UNIVERSIDADE TECNOLÓGICA FEDERAL DO PARANÁ

FELIPE OLIVEIRA BASSO

SIMULAÇÕES DE GRANDES ESCALAS E SIMULAÇÃO NUMÉRICA DIRETA SUB-RESOLVIDA DE ESCOAMENTO TURBULENTO DE FLUIDOS HERSCHEL-BULKLEY

Tese

CURITIBA
2022

FELIPE OLIVEIRA BASSO

SIMULAÇÕES DE GRANDES ESCALAS E SIMULAÇÃO NUMÉRICA DIRETA SUB-RESOLVIDA DE ESCOAMENTO TURBULENTO DE FLUIDOS HERSCHEL-BULKLEY

Large-Eddy Simulation and Under-Resolved Direct Numerical Simulation of Turbulent Flow of Herschel-Bulkley Fluids

Thesis presented to the Postgraduate Programme in Mechanical and Materials Engineering (PPGEM) from the Federal University of Technology - Parana, as partial fulfilment of the requirements for the degree of Doctor of Sciences.

Advisor: Prof. Dr. Admilson Teixeira Franco

CURITIBA
2022

4.0 Internacional

This license allows reusers to distribute, remix, adapt, and build upon the material in any medium or format for noncommercial purposes only, and only so long as attribution is given to the creator. If you remix, adapt, or build upon the material, you must license the modified material under identical terms.

Ministério da Educação
Universidade Tecnológica Federal do Paraná
Campus Curitiba

FELIPE OLIVEIRA BASSO

SIMULAÇÕES DE GRANDES ESCALAS E SIMULAÇÃO NUMÉRICA DIRETA SUB-RESOLVIDA DE ESCOAMENTO TURBULENTO DE FLUIDOS HERSCHEL-BULKLEY.

Trabalho de pesquisa de doutorado apresentado como requisito para obtenção do título de Doutor Em Engenharia Mecânica da Universidade Tecnológica Federal do Paraná (UTFPR). Área de concentração: Engenharia Térmica.

Data de aprovação: 01 de Julho de 2022

Dr. Admilson Teixeira Franco, Doutorado - Universidade Tecnológica Federal do Paraná

Dr. Cezar Otaviano Ribeiro Negrao, Doutorado - Universidade Tecnológica Federal do Paraná

Dr. Gilmar Mompean Munhoz Da Cruz, Doutorado - Université Lille 1, Sciences Et Technologie

Dr. Roney Leon Thompson, Doutorado - Universidade Federal do Rio de Janeiro (Ufrj)

Dr. Silvio Luiz De Mello Junqueira, Doutorado - Universidade Tecnológica Federal do Paraná

Documento gerado pelo Sistema Acadêmico da UTFPR a partir dos dados da Ata de Defesa em 04/07/2022.

ACKNOWLEDGEMENTS

I would like to thank my supervisor, Admilson T. Franco, for the constant encouragement, dedication, and guidance of the work.

I would like to thank all my colleagues at the Center for Research in Rheology and Non-Newtonian Fluids (CERNN) for their advice, valuable academic discussions, and shared moments over the years.

I am very thankful to my family for their support, patience, love, and especially for understanding my absence.

I appreciate the support from the National Council for Scientific and Technological Development of Brazil (CNPq) and Petrobras for partially funding this research.

Finally, this study was financed in part by the Coordenação de Aperfeiçoamento de Pessoal de Nível Superior - Brasil (CAPES) - Finance Code 001.

RESUMO

BASSO, FELIPE OLIVEIRA. **Simulações de Grandes Escalas e Simulação Numérica Direta Sub-Resolvida de Escoamento Turbulento de Fluidos Herschel-Bulkley**. Tese. Programa de Pós-Graduação em Engenharia Mecânica e de Materiais, Universidade Tecnológica Federal do Paraná, Curitiba, Brasil, 137 páginas, 2022.

Escoamentos turbulentos de fluidos não newtonianos com o modelo Herschel-Bulkley são encontrados em várias aplicações de engenharia, por exemplo, fluidos de perfuração, lamas de mineração e soluções de polímeros. No entanto, estudos sobre simulações de grandes escalas (LES) envolvendo esse tipo de fluido são escassos. O presente trabalho visa contribuir para este debate. A primeira parte da tese se concentra na avaliação da abordagem LES na previsão das características de escoamento de fluidos Herschel-Bulkley. A metodologia numérica é comparada com dados de referência da literatura. Dois modelos de sub-malha (SGS) são considerados: Dynamic Smagorinsky e Wall Adapting Local Eddy-viscosity (WALE). Além disso, simulações numéricas direta sub-resolvidas (UDNS) também são realizadas. Em seguida, o método de solução é utilizado para analisar o escoamento turbulento de fluidos Herschel-Bulkley através de uma seção anular concêntrica com rotação interna do cilindro em $Re_G \approx 9,000$. A influência do índice de comportamento do escoamento ($n = 0.65$, 0.70 e 0.75), número de Bingham ($B_n = 0.10$, 0.25 e 0.40), e a taxa de rotação ($N = 0.15$ e 0.30) nas características de escoamento são exploradas. As quantidades de escoamento instantâneo, incluindo contornos da velocidade axial e viscosidade, estruturas de vórtices, estatísticas de turbulência de primeira e segunda ordem e características do escoamento médio, como perfis viscosidade, energia cinética turbulenta, gradiente de pressão e fator de atrito são investigados. Os resultados mostram que estruturas turbulentas mais fracas são geradas à medida que o valor de n é reduzido e o número de Bingham elevado. Aumentar a taxa de rotação aumenta as magnitudes das estatísticas turbulentas e torna os níveis de flutuações de velocidade mais assimétricos. Demonstra-se também que as previsões obtidas com os modelos SGS e UDNS não apresentam diferenças significativas.

Palavras-chave: Simulação das Grandes Escalas, Simulação Numérica Direta Sub-Resolvida, Turbulência, Fluido Herschel–Bulkley.

ABSTRACT

BASSO, FELIPE OLIVEIRA. **Large-Eddy Simulation and Under-Resolved Direct Numerical Simulatoin of Turbulent Flow of Herschel-Bulkley Fluids**. Thesis. Postgraduate Program in Mechanical and Materials Engineering, Federal University of Technology - Parana, Curitiba, Brazil, 137 pages, 2022.

The Herschel-Bulkley model's turbulent flows of non-Newtonian fluids are encountered in several engineering applications, e.g. drilling fluids, mining slurries, and polymer solutions. However, studies regarding Large Eddy Simulations (LES) involving this type of fluid are scarce. The present work aims to contribute to this issue. The first part of the thesis focuses on evaluating the LES approach in predicting the flow features of Herschel-Bulkley fluids. The numerical methodology is compared against literature reference data. Two subgrid-scale (SGS) models are considered: Dynamic Smagorinsky and Wall Adapting Local Eddy-viscosity (WALE) models. Additionally, under-resolved direct numerical simulations (UDNS) are also performed. Following that, the solution method is used to analyze the turbulent flow of Herschel-Bulkley fluids through a concentric annular section with inner cylinder rotation at $Re_G \approx 9,000$. The influence of the flow behavior index ($n = 0.65$, 0.70 and 0.75), the Bingham number ($B_n = 0.10$, 0.25 and 0.40), and the rotation rate ($N = 0.15$ and 0.30) on the flow characteristics are explored. The instantaneous flow quantities, including contours of the axial velocity and viscosity, vortex structures, the first- and second-order turbulence statistics, and mean flow features, such as mean viscosity profiles, mean turbulence kinetic energy, pressure gradient, and friction factor are investigated. The results show that weaker turbulent structures are generated as the n value is reduced and the Bingham number increases. Raising the rotation rate enhances the magnitudes of turbulent statistics and makes the levels of velocity fluctuations more asymmetrical. It is also demonstrated that predictions obtained with the SGS models and the UDNS do not present significant differences.

Keywords: Large-Eddy Simulation, Under-resolved Direct Numerical Simulation, Turbulence, Herschel-Bulkley fluids.

LIST OF FIGURES

LIST OF TABLES

LIST OF ABBREVIATIONS AND ACRONYMS

CDS	Convection Differencing Scheme
CFD	Computational Fluid Dynamics
CFL	Courant Friedrichs Lewy
CMC	Sodium Carboxymethyl Cellulose
CPU	Central Processing Units
DILU	Diagonal Incomplete Lower Upper
DNS	Direct Numerical Simulation
FVM	Finite Volume Method
GNF	Generalized Newtonian Fluid
GNU	General Public License
ILES	Implicit Large-Eddy Simulation
LDA	Laser Doppler Anemometry
LDV	Laser Doppler Velocimetry
LES	Large-Eddy Simulation
NNSGS	Non-Newtoanian Subgrid-Scale stress tensor
OpenFOAM	Open source Field Operation And Manipulation
PBICG	Preconditioned Bi-Conjugate Gradient
PISO	Pressure Implicit Split Operator
PIV	Particle Image Velocimetry
RANS	Reynolds-Averaged Navier-Stokes
RPM	Revolutions Per Minute
SGS	Subgrid-Scale
UDNS	Under-Resolved Direct Numerical Simulation
WALE	Wall Adapting Local Eddy-viscosity

NOMENCLATURE

Roman letters and symbols

$\mathbf{A}_\phi$	Discretization matrix	$[-]$
A	Mean flow advection	$[m^2\ s^{-3}]$
C_S	Model constant	$[-]$
$\mathbf{d}$	Vector between P and N	$[m]$
D	Diameter / Integration domain	$[m/-]$
D_t	Mean viscous transport	$[m^2\ s^{-3}]$
E	Energy density	$[m^2\ s^{-2}]$
f	Friction coefficient / Any flow quantity	$[-]$
F	Mass flux through the face	$[m^3/s]$
g_b	Fixed gradient at boundary b	$[-]$
G	Filter function	$[-]$
k	Turbulent kinetic energy per unit mass	$[m^2\ s^{-2}]$
k	Wave number	$[m^-1]$
K	Fluid consistency index	$[Pa\ s^n]$
K_o	Kolmogorov constant	$[-]$
l	Large eddies' length scale	$[m]$
L	Characteristic length	$[m]$
L_z	Axial domain length	$[m]$
L_θ	Azimuthal domain length	$[rad]$
L_{ij}^{SGS}	Leonard stress tensor	$[Pa]$
M	Ratio of the resolved turbulent kinetic energy to the modeled one	$[-]$
∇	Nabla operator	$[-]$
n	Flow behavior index	$[-]$
N	Point in the center of the neighbouring control volume	$[-]$
N_{x_i}	Number of cells in i^{th} direction	$[-]$
p	Pressure	$[Pa]$
P	Modified pressure / Point in the center of the control volume	$[Pa/-]$
P_t	Turbulent kinetic energy production	$[m^2\ s^{-3}]$
r	Radial coordinate	$[m]$
R	Radius of the cylinder	$[m]$
R_r^*	Radius raio	$[-]$
$\mathbf{R}$	R.h.s vector for discretization system	$[-]$
R_{zz}	Two-point correlation function	$[m^2\ s^{-2}]$

s', s''	Ratio of the SGS viscosity to the molecular viscosity	$[-]$
S_ϕ	Source term	$[-]$
$\mathbf{S}$, S_{ij}	Rate-of-strain tensor	$[s^{-1}]$
$\mathbf{S}$	Outward-pointing face area vector	$[-]$
t	Time	$[s]$
T_t	Turbulent velocity transport	$[m^2\ s^{-3}]$
T_{ij}^{SGS}	Subgrid-scale test stress tensor	$[Pa]$
u	Large eddies' velocity scale	$[m\ s^{-1}]$
u_i	Velocity component in the i^{th} direction	$[m\ s^{-1}]$
u_τ	Friction velocity	$[m\ s^{-1}]$
$\mathbf{u}$	Velocity vector	$[m\ s^{-1}]$
U_b	Bulk velocity	$[m\ s^{-1}]$
V	Volume	$[m^3]$
V_p	Computational cell volume	$[m^3]$
z	Axial coordinate	$[-]$
x_i	i^{th} direction in a Cartesian coordinate system	$[-]$
$\mathbf{x}$	Position vector	$[m]$

Greek letters

$\dot{\gamma}$	Shear rate	$[s^{-1}]$
Γ	Diffusivity coefficient	$[-]$
δ	One-half of the annular gap	$[m]$
δ_{ij}	Kronecker delta	$[-]$
Δ	Filter size	$[m]$
Δt	Time interval	$[s]$
Δx_i	spatial mesh size	$[m]$
$\boldsymbol{\Delta}$	Orthogonal contribution of the face area vector	$[m]$
ε	Rate of energy dissipation	$[m^2\ s^{-3}]$
ε'	Ratio of the SGS dissipation to the molecular dissipation	$[-]$
ϵ	Mean viscous dissipation	$[m^2\ s^{-3}]$
η_k	Smallest eddies' length scale	$[m]$
η	apparent viscosity	$[Pa\ s]$
θ	Azimuthal coordinate	$[rad]$
ζ	Pressure-related transport	$[m^2\ s^{-3}]$
ϑ	Smallest eddies' velocity scale	$[m\ s^{-1}]$
κ	Von Kármán constant	$[-]$
μ	Dynamic viscosity	$[Pa\ s]$

ν	Kinematic viscosity	$[m^2\ s^{-1}]$
ν_{SGS}	Kinematic eddy viscosity	$[m^2\ s^{-1}]$
Π	Rate of transfer of kinetic energy per unit mass	$[m^2\ s^{-3}\ kg^{-1}]$
$\boldsymbol{\varpi}$	Non-orthogonal contribution of the face area vector	$[m]$
ρ	Density	$[kg\ m^{-3}]$
$\boldsymbol{\sigma}$	Viscous stress tensor	$[Pa]$
ς	Mean shear turbulent viscous transport	$[m^2\ s^{-3}]$
τ_w	Wall shear stress magnitude	$[Pa]$
τ_y	Yield stress	$[Pa]$
$\boldsymbol{\tau}^{SGS}$, τ_{ij}^{SGS}	Subgrid-scale stress tensor	$[Pa]$
$\boldsymbol{\tau}^{\boldsymbol{NNSGS}}$	Non-Newtonian subgrid-scale stress tensor	$[Pa]$
Υ	Turn-over time	$[s]$
ϕ	Generic scalar quantity	$[-]$
χ_{nn}	Mean shear turbulent viscous dissipation	$[m^2\ s^{-3}]$
Ψ	Pressure gradient	$[Pa\ m^{-1}]$
ω	Angular frequency	$[rad\ s^{-1}]$
Ω	Angular velocity	$[rad\ s^{-1}]$

Non-dimensional parameters

Bn	Bingham number $\tau_y L^n / K U_b^n$	$[-]$
He	Hedstrom number $\rho L^2 \tau_y^{(2/n-1)} / K^{2/n}$	$[-]$
r^*	Non-dimensional radial coordinate $(r - R_i)/(R_o - R_i)$	$[-]$
Re	Reynolds number $\rho \mathrm{U_b} L/\mu$	$[-]$
Re_τ	Friction Reynolds number $u_\tau L/\nu$	$[-]$
Re_G	Generalized Reynolds number $\rho \mathrm{U_b} L/\eta$	$[-]$
Re_{η_k}	Smallest eddies Reynolds number $\vartheta \eta_k/\nu$	$[-]$
N	Rotation rate $\Omega R_{rc}/U_b$	$[-]$
Δx_i^+	Non-dimensional cell size $\Delta x_i u_\tau/\nu$	$[-]$
y^+	Non-dimensional wall distance $y u_\tau/\nu$	$[-]$

Superscripts

$(\ )'$	Fluctuation field
$\overline{(\ )}$	Time-averaged quantity
$\widetilde{(\ )}$	Filtered quantity
$\widehat{(\ )}$	Test filter
$(\ )^0$	Previous time-step
$(\ )^+$	Wall coordinates

$(\,)^{\mathrm{T}}$	Transposed

Subscripts

$(\,)_b$	Boundary face
$(\,)_f$	Cell face
$(\,)_P$	Cell of interest
$(\,)_i$	Inner cylinder
$(\,)_N$	Neighbouring cell
$(\,)_{nn}$	Non-Newtonian fluids
$(\,)_o$	Outer cylinder
$(\,)_{rc}$	Rotating cylinder
$(\,)_{res}$	Resolved scales
$(\,)_{SGS}$	Subgrid-scales
$(\,)_w$	Wall

CONTENTS

1 INTRODUCTION

1.1 Motivation

Transitional and turbulent flows of non-Newtonian fluids with viscoplastic characteristics are encountered in various applications and biological systems. These applications include drilling fluid flows, mining slurries, paint industries, polymer solutions, and blood flow in arteries.

The blood is a complex fluid in the medical field that presents some non-Newtonian rheological characteristics, including deformation rate dependency, viscoelasticity, and thixotropic behavior (ZAMAN et al., 2015). The laminar-turbulent transition of blood flow can be found in the arteries of patients who have vascular stenosis disease. Stenosis is an abnormal narrowing in a blood vessel caused by accumulations of low-density lipoproteins, e.g., cholesterol (MOLLA; PAUL, 2012; KHAN et al., 2018). As a consequence, turbulent flows can damage blood-cell components in the form of mechanical hemolysis anemia - damage to the red blood cells due to the high wall shear stress associated with turbulence – and thrombus formation – the post-stenotic flow has a recirculation zone that facilitates the accumulation of platelets, providing an optimal environment for coagulation (KELLY et al., 2020).

In the wellbore drilling process, non-Newtonian fluids with viscoplastic behavior are used as a drilling fluid (MITCHELL; MISKA, 2011). According to Mitchell and Miska (2011) and Caenn and Chillingar (1996), the primary functions of the drilling fluids are: to transport the cuttings from the hole to the surface through the annular region; hold cutting in suspension when fluid circulation is interrupted; support the wellbore wall and maintain the wellbore stability; cool and lubricate the rotating drill string and drill bit; control the subsurface pressure.

A drilling method widely used is the rotary drilling process (HOSSAIN; AL-MAJED, 2015). Figure 1.1 illustrates a schematic view of this type of operation. The drilling fluid is pumped into the drill string, passes through the bit nozzles, and returns to the surface, carrying the cuttings through the annular region formed between the hole walls and drill string.

The drilling fluid flow in the annular region preferably occurs under a laminar regime. However, in situations where it is necessary to increase the flow rate to prevent excessive cutting sedimentation (cutting bed) in the annular region, the flow may become turbulent. Moreover, the flow in the annulus can be laminar, transitional, or turbulent depending on the parameters such as drill string rotation, drill string eccentricity concerning the wellbore center, diameter ratio between the drill string and wellbore diameter, and fluid rheological properties (ERGE et al., 2015a).

Hossain and Al-Majed (2015) and CAENN et al. (2017) argue that most of the problems encountered during the drilling process, such as slow drilling rate and loss of circulation, are directly or indirectly related to the drilling fluids. Therefore, knowing the behavior of these fluids in different flow regimes is essential to control processes during a drilling operation.

Figure 1.1 – Schematic representation of drilling operation and wellbore cleaning.

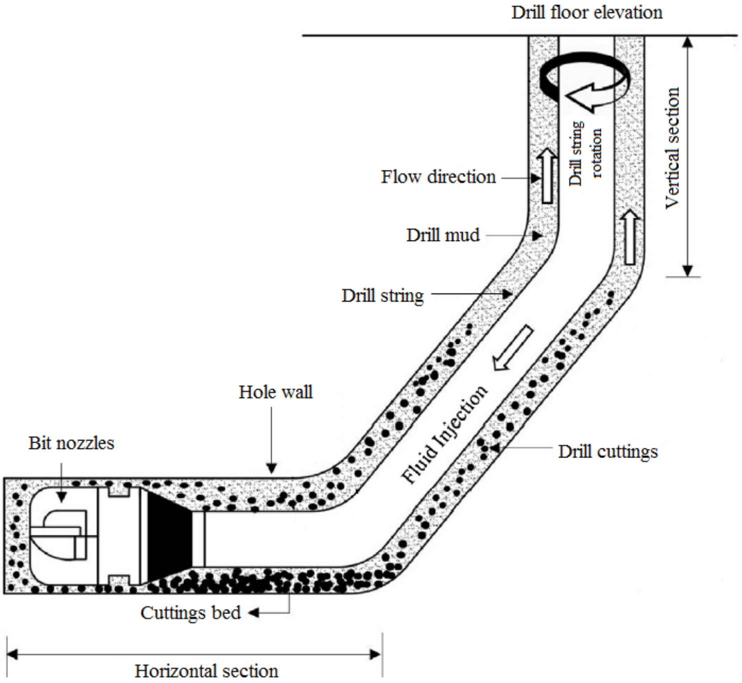

Source: Adapted from Epelle and Gerogiorgis (2018).

Based on the above considerations, the particular motivation for the present work comes from the research regarding turbulent flows of non-Newtonian fluids and the oil industry. While the turbulence theory and numerical methods are well-developed for the Newtonian fluids, there are gaps in the literature regarding theoretical understanding, physical phenomena, and mathematical modeling for turbulent flows of non-Newtonian fluids.

1.2 Numerical Simulation of Turbulent Flows

Turbulence is an omnipresent phenomenon in fluid flow dynamics. For several decades engineers and scientists have been trying to comprehend turbulence mechanisms and develop methods to model turbulent flows.

From a numerical solution, the turbulent flow can be computed with different levels of approximation. The most straightforward approach to solve the turbulent flows is a direct numerical simulation (DNS), which directly resolves all the spatial and temporal scales of the flow without any turbulence modeling approximation. Supposing the mesh is fine enough to resolve even the smallest scales of motion, the dissipative scales, and the numerical scheme employed is designed to minimize the numerical dispersion and dissipation errors, one can obtain an accurate solution to the balance equations free of modeling assumptions (PIOMELLI, 1999). DNS provides a detailed understanding of turbulence mechanisms, which is helpful for the improvement of theories and the development of turbulence models. However, DNS is computationally expensive, and it is currently unfeasible for most calculations of industrial flows.

Statistical methods were developed to reduce the number of scales solved in a turbulent flow. The Reynolds-averaged Navier-Stokes (RANS) simulations are based on the statistical description of the flow. Reynolds (1896) proposed that any instantaneous variable of a turbulent flow, such as velocity field $\mathbf{u}(\mathbf{x}, t)$, could be decomposed into a mean value $\bar{\mathbf{u}}(\mathbf{x})$ and a fluctuation part $\mathbf{u}'(\mathbf{x}, t)$ through an averaging procedure, yielding $\mathbf{u}(\mathbf{x}, t) = \bar{\mathbf{u}}(\mathbf{x}) + \mathbf{u}'(\mathbf{x}, t)$.

One obtains the well-known RANS equations by inserting the Reynolds decomposition into the Navier-Stokes equations. These equations describe the evolution of the mean quantities, while the effect of turbulent fluctuations introduces a new term, the so-called Reynolds stress tensor, which must be modeled to close the system. The Reynolds stress tensor can be determined by a turbulence model via the eddy viscosity hypothesis or computed directly from the Reynolds stress transport equation (POPE, 2000).

The cost of RANS simulations is significantly lower compared to DNS. Consequently, the solution of RANS equations is commonly used in industrial applications to predict the turbulent flow. Unfortunately, since the resolved field is limited to the mean flow, no information is provided about coherent turbulence structures and two-point correlations, for example.

Large-eddy simulation (LES) is a technique intermediate between the DNS of turbulent flows and the solution of the RANS equations, and it is motivated by the limitations of each of these approaches. In LES, the large-scale turbulent motions are solved explicitly, while the small ones are modeled. The LES approach avoids the problem of the RANS method, which also models the motion of large scales, which contain most of the kinetic energy in a turbulent flow. At the same time, keep away from the DNS issue of having to solve the dissipative scales. According to Pope (2000), nearly all of the computational effort in DNS is spent on the smallest scales of turbulence.

Since the small scales are more homogeneous, dissipative, and contain little energy than the large eddies, it is appropriate to model them (RODI et al., 2013). The effect of the small (unresolved) scales can be modeled explicitly (explicit LES) or implicitly (Implicit LES).

In explicit LES, an additional forcing term (Subgrid-scale (SGS) stress tensor) is added to the Navier–Stokes equations (SAGAUT, 2006). Conversely, in Implicit LES (ILES), no additional term is introduced to the Navier–Stokes equations, and the effects of unresolved scales are incorporated implicitly via a numerical scheme (SAGAUT, 2006; GRINSTEIN et al., 2007). The computational effort is significantly reduced by modeling the small-scale fluctuations compared to a DNS solution, and LES can produce quantitatively satisfactory predictions. Details about the filtering procedure are discussed in Section 2.5.

In an alternative approach, the Navier–Stokes equations are solved directly on a (coarse) LES mesh executed without an SGS model and constraints imposed on the numerical dissipation (CASTIGLIONI; DOMARADZKI, 2015; KOMEN et al., 2017). In the current thesis, this approach is referred to as under-resolved direct numerical simulation (UDNS) or no-model LES, following the works of Castiglioni and Domaradzki (2015) and Komen et al. (2017).

1.3 Literature Review

This section reviews previous works regarding the turbulent flow of generalized Newtonian fluids (GNF), focusing on fluids characterized by the Herschel-Bulkley model. A definition of GNF is given in Chapter 2 (Section 2.2). The literature review is divided into three topics. Section 1.3.1 reports the experimental studies in pipes. In Section 1.3.2, experimental works in the annular section are discussed. In Section 1.3.3, DNS and LES of turbulent flows of GNFs are debated.

1.3.1 Experimental Studies in Pipes

Experimental works regarding turbulent flows of GNFs initially focused on correlations for the friction factor. Authors such as Metzner and Reed (1955), Dodge and Metzner (1959), Torrance (1963), Hanks (1978), Wilson and Thomas (1985), and Slatter (1995) proposed several methods to measure the coefficient of friction factor.

Early experimental studies concerning the flow visualization and measurements of turbulent statistics of GNFs in pipes were published by Park et al. (1989), Pinho and Whitelaw (1990), and Pereira and Pinho (1994). All works above used laser Doppler velocimeter (LDV) as a measurement technique to investigate the flow features. The studies showed similar behaviors for the non-Newtonian fluids, such as an increase in the mean velocity profiles and axial turbulence intensities, suppression of radial and azimuthal turbulence intensities, and delay in the transition from laminar to turbulent flow.

Escudier and Presti (1996) performed Laser Doppler Anemometry (LDA) measurements to investigate the Laponite solution in laminar, transitional, and fully turbulent flows. The Herschel-Bulkley model fitted the viscosity apparent in the testing fluid. Escudier and Presti (1996) were the first researchers to report the asymmetric behavior in mean velocity profiles when the flow is in a transitional regime. It was speculated that the asymmetry is either associated with instabilities in the flow during the transitional or with small geometric imperfections in the flow loop.

Peixinho et al. (2005) carried out an experimental study to analyze laminar, transitional, and turbulent flow with three different fluids: 0.2% Carbopol solution as viscoplastic fluid,an aqueous solution of 2% sodium carboxymethyl cellulose (CMC) as a shear-thinning fluid, and glucose syrup as a Newtonian fluid. The Herschel-Bulkley model fitted the Carbopol solution, whereas the Cross model characterized the CMC solution. For the Carbopol solution, the asymmetry in the mean velocity profile appears in the transitional regime, while in laminar and turbulent regimes, no evident asymmetry was noticed. The drag reduction effect for both non-Newtonian fluids was observed in turbulent flow via friction factor measurements and velocity profiles. The authors also argue that the transition for the yield stress fluid takes place in two stages. The experimental velocity profile departs slightly from the laminar theoretical solution in the first stage. The fluctuations are suppressed in the central zone (plug zone) and increase slightly outside this zone. Then, in the later stage, with increasing the Reynolds number, turbulent spots fill up the whole section, and the plug zone is disrupted due to large velocity fluctuations. Between two successive spots, the presence of the plug zone is still possible.

Subsequently, Escudier et al. (2005) performed LDA measurements in unrelated research programs in the UK, France, and Australia. They used a wide range of non-Newtonian fluids with rheological curves fitted by Herschel-Bulkley and Carreau-Yasuda models. In all cases, the mean velocity profiles were axisymmetric for laminar and turbulent flow conditions, while asymmetries for the transitional flow were observed. Thus, the authors concluded that asymmetry must result from a fluid-dynamic mechanism rather than imperfections in the flow facilities. Typical mean axial velocity profiles obtainedby the authors are shown in Figure1.2.

Figure 1.2 – Mean axial velocity profiles at different Reynolds numbers for 0.2% Carbopol solution. The Herschel-Bulkley parameters: τ_y = 9.80 [Pa], K = 2.31 $[\mathrm{Pa\,s}^n]$, $n = 0.51$.

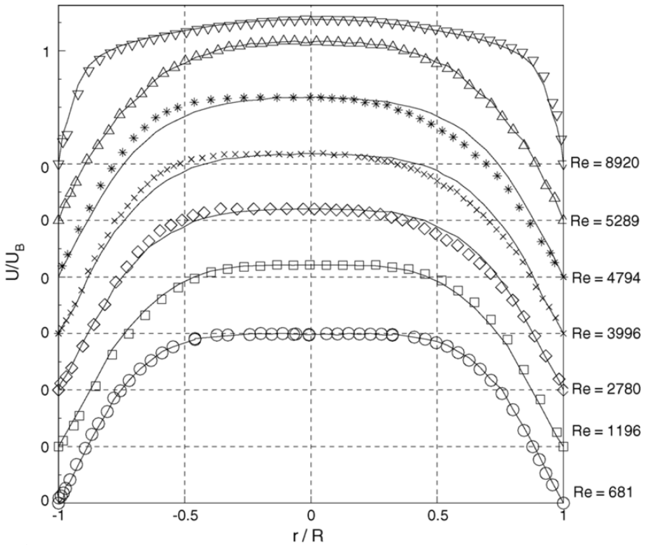

Source: Escudier et al. (2005).

A description of asymmetry in the transitional regime was also provided by Esmael and Nouar (2008). According to the authors, a feasible explanation for these asymmetries is attributed to a nonlinear coherent structure characterized by two weakly modulated counter-rotating longitudinal vortices.

Guzel et al. (2009) investigate the transition to turbulence of a yield stress shear-thinning fluid experimentally. From the results, the researchers mention that the plug breaks – vanish – before starting the transition regime. Moreover, they observed that once in the transition or turbulent regime, the behavior of the yield stress fluid is similar to a shear-thinning fluid.

Bahrani and Nouar (2014) measured the mean velocity profiles experimentally using LDV for an 0.2% Carbopol solution at different Reynolds numbers. According to the authors, two stages are identified during the transition to turbulence. In the first stage, called pre-transition, a central zone (plug zone) remains in the laminar regime with occasionalvelocity fluctuations. At this stage, the mean velocity profile exhibits a slight asymmetry, and the experimental measurements of the friction factor are very close to the theoretical laminar solution. The second stage corresponds to the appearance of turbulent puffs with a significant asymmetry in the axial velocity profile. These observations are in agreement with Peixinho et al. (2005).

1.3.2 Experimental Works in Annular Sections

As mentioned in the previous section, the return of drilling fluid to the surface during the drilling process occurs in an annular region formed between the hole walls and drill string. In addition, the flow in annular passages is also crucial in several areas of engineering, such as heat exchangers, and gas-cooled nuclear reactors (CHUNG; SUNG, 2005). This section reviews the experimental works of GNFs flow in laminar-turbulent transition regimes in the annular sections.

Amongst the available literature, the work of Nouri et al. (1993) stands out as one of the first experimental studies of turbulent flows in annular sections with non-Newtonian fluids. Nouri et al. (1993) analyzed turbulent flows in concentric and eccentric annular passages with a Newtonian fluid and a non-Newtonian solution (0.2% CMC solution) for several Reynolds numbers. The Power-Law model fitted the apparent viscosity of 0.2% CMC solution. The LDV technique obtained the mean velocity profiles and Reynolds shear stress. They observed that the profiles of mean velocity and axial turbulent intensity are similar to those obtained for the Newtonian fluid at an equal Reynolds number, while the radial and azimuthal turbulence intensities are suppressed.

Subsequently, Nouri and Whitelaw (1994) extended their previous work (NOURI et al., 1993), including the rotation effect of the inner cylinder (300 rpm) on turbulent flows in a concentric annular passage. They observed that the mean axial velocity profiles become flattered with increasing cylinder rotation, and there is an enhancement in turbulence intensities due to the rotation effect. Later, Nouri and Whitelaw (1997) performed an experimental investigation through an eccentric annular section, including the effects of inner cylinder rotation.

Escudier et al. (1995) conducted measurements using LDA for laminar, transitional, and turbulent flows in a concentric annular section for three non-Newtonian fluids: a Xanthan gum, 0.2% CMC solution, and a laponite–CMC blend. The rheological curves for the non-Newtonian fluids were fitted by Carreau, Cross, and Herschel-Bulkley models. Measurements were also conducted for a Newtonian fluid. Distributions of mean axial velocity, axial and azimuthal turbulence intensities, and friction factors are presented. For the turbulent flow, it was observed that all non-Newtonian fluids showed a significant drag reduction compared to Newtonian fluid. The axial turbulence intensities for the non-Newtonian solutions exhibited similar magnitudes distributions to those observed for the Newtonian cases, while the azimuthal velocity fluctuations are lowered in intensity. These results agree with the study conducted by Nouri et al. (1993).

Japper-Jaafar et al. (2010) conducted LDA measurements for laminar-turbulent transition flow through a concentric annular region for Newtonian and non- Newtonian fluids. The Carreau–Yasuda model was used to fit the data of Xanthan gum and the Herschel-Bulkley model to fit the Carbopol solutions. Particular attention is placed on the transitional flow region. The transitional flow regime is studied by monitoring the axial turbulence intensity level. They found that the Reynolds number range for transitional flow is greater for the more shear-thinning fluids.

Erge et al. (2015b) analyzed the laminar-turbulent transition of non-Newtonian fluids in concentric and eccentric annular regions. Blends of Laponite solutions, Xanthan gum, and polyanionic cellulose (PAC R) additives were used as testing fluids, and the Herschel-Bulkley model fitted their rheological curves. Both theoretical and experimental approaches are used to better understand the onset of transitional flow.

The authors concluded that the transition from laminar to turbulent significantly depends on eccentricity, diameter ratio, and fluid properties, especially the shear-thinning ability of the fluid.

Experimental works provide valuable information about the behavior of GNFs in turbulent flows. However, those aqueous solutions of CMC, Xanthan gum, and laponite, often used as testing fluid, can exhibit some degree of viscoelasticity and thixotropy (ESCUDIER et al., 1995; PEIXINHO et al., 2005). According to (RUDMAN; BLACKBURN, 2006), although the level of viscoelasticity can be irrelevant in low shear, e.g. laminar flow, becomes essential in the high shear, typical of turbulent flow.

1.3.3 DNS and LES of Turbulent Flows of GNFs

Early studies regarding DNS of turbulent flows of GNFs were presented by Rudman et al. (2004) and Rudman and Blackburn (2006). Turbulent pipe flow of Power-law, Herschel-Bulkley, and Carreau–Yasuda fluids were simulated numerically with a high-order spectral element-Fourier DNS code – *Semtex*. These studies investigated the effect of rheological properties on the turbulent flow structure at moderate Reynolds numbers. The results with non-Newtonian fluids showed a reduction in the friction factor when compared to a Newtonian fluid. Analysis of the flow field revealed coarser turbulent structures than for Newtonian fluids with the homologous Reynolds numbers. Moreover, the yield stress fluids weaken the turbulent structures further, driving the flow toward the transitional regime.

Another study regarding DNS with Power-law fluids was developed by Gavrilov and Rudyak (2016) at relatively higher Reynolds numbers Re_G ($10,000 \sim 20,000$). Five different flow behavior indexes *n* from 0.4 to 1 were considered. The authors published the first study about the anisotropy of Power-law fluids through anisotropy-invariant maps. They noted that the Power-law fluids exhibit stronger turbulent anisotropy than a Newtonian fluid, and the anisotropy becomes more significant with the decreasing flow behavior index. The authors also observed that turbulence intensity increases in the axial direction but decreases in the radial and the azimuthal directions with the reducing flow behavior index. They argue that this phenomenon is associated with the suppression of the energy transfer from the axial fluctuations to the transverse ones.

Singh et al. (2017a) used the same numerical formulation as Rudman et al. (2004) to perform an investigation regarding the influence of flow index behavior of Power-law fluids in turbulent pipe flow for friction Reynolds number $Re_\tau = 323$. The results were analyzed to understand the shear-thinning effects for first- and second-order flow statistics, including turbulent kinetic energy production, transport, and dissipation. In addition, the simulations showed that the turbulent kinetic energy budget is affected by shear-thinning, mainly in the near-wall region ($y^+ \leq 60$). After that, Singh et al. (2018) performed simulations with Power-law fluid for friction Reynolds numbers $Re_\tau = 323 \sim 750$ ($Re_G = 10,000 \sim 28,000$). The reported results are similar to the work carried out by Gavrilov and Rudyak (2016). The results provided strong evidence that the shear-thinning effect does not disappear by increasing the Reynolds number.

Subsequently, Singh et al. (2017b) investigated the effects of yield stress on turbulent pipe flow of Herschel-Bulkley and Bingham fluids at a generalized Reynolds number of $Re_G \approx 11,000$. Simulations were carried out with the yield stress varying from 0% to 20% of the mean wall shear stress. The results demonstrated increased axial turbulence intensity when the yield stress was enhanced. In contrast, the radial and azimuthal turbulence intensities were lower for higher yield stresses. The influence of yield stress is similar to shear-thinning, acting as a turbulence dampening instrument. However, the effect of yield stress is larger outside the viscous sublayer ($y^+ < 5$), while shear-thinning acts more inside the viscous layer. Analysis of the turbulent kinetic energy budget terms showed that the effect of yield stress is more significant for $y^+ \leq 60$.

Zheng et al. (2019) performed DNS of turbulent pipe flow of Herschel-Bulkley fluids and compared the performance of two numerical methods. The accuracy and efficiency of OpenFOAM – a second-order finite volume code – were evaluated against the high-order spectral element-Fourier DNS code *Semtex*. The simulations were run for nominal generalized Reynolds numbers of $Re_G = 5,000$ and $Re_G = 7,500$. The results showed that OpenFOAM predicts a more transitional Herschel-Bulkley fluid flow than *Semtex's* predictions, with lower second-order turbulence statistics in the radial and azimuthal directions and a higher peak in the axial direction. Profiles of the second-order turbulence statistics presented disagreement between the codes, with a maximum difference of 16% in the peak value of second-order turbulence statistics in the azimuthal direction at $Re_G = 5,000$. The discrepancy between the codes decreased as the Reynolds number increased, with a maximum difference of 7,7% for $Re_G = 7,500$.

Arosemena et al. (2021) performed DNS of turbulent channel flow of Carreau fluids. The different statistics studied reveal that the fluid rheology effect appears mainly to affect the flow within the inner layer region $y^+ \leq 110$, suppressing near-wall structures such as quasi-streamwise vortices and low-speed streaks, inhibiting turbulence generating events and leading to different drag reduction features.

There have been few studies regarding the LES of GNF. In this approach, extra terms arise when the spatial filter is applied to the balance equations due to the non-Newtonian viscosity (OHTA; MIYASHITA, 2014; AMANI et al., 2021). Additionally, the existence of several constitutive models (Power-law, Casson, Cross, Herschel-Bulkley, Bingham) makes it challenging to develop a generalist SGS model to account for the effects of GNF.

Molla and Paul (2012) performed LES with the Dynamic Smagorinsky model ignoring the additional term imposed by the non-Newtonian stress tensor to investigate the transition to turbulent non-Newtonian fluid flow through arterial stenosis using various GNF models (Power-law, Carreau, Quemada, Cross, and the viscoplastic modified-Casson model) to simulate the blood viscosity. The distributions of shear rate, post-stenotic recirculation zone, mean shear stress, mean pressure, and turbulent kinetic energy were discussed.

Ohta and Miyashita (2014) carried out DNS and LES of turbulent channel flow of GNF. The authors evaluated the capability of an extended Smagorinsky SGS model with correction function (damping function) in the filter width for a locally varying viscosity employing the Power-law and the viscoplastic Casson model. Ohta and Miyashita (2014) analyzed the profiles of the additional term and compared them with the SGS stress. As a result, the authors ignore the influence of the additional term as it is much smaller than the SGS stress. Mean axial velocity profiles and Reynolds shear stress were assessed with the Power-law fluid, while only the mean axial velocity profiles were analyzed with the Casson model. The extended Smagorinsky model's results agreed better with the DNS data than the standard Smagorinsky model in coarse grids. From the analyses, it can be seen that the well-resolved LES with the standard Smagorinsky's model reproduced the flow features correctly. In dense grids, both SGS models showed similar results, suggesting that the scale features of the viscosity fluctuations are small.

Gnambode et al. (2015) follow the arguments of Ohta and Miyashita (2014) and also neglected the additional term. The authors performed LES of turbulent pipe flow of Power-law fluids for various power-law indices ($0.5 \leq n \leq 1.4$) at different Reynolds numbers ($4,000 \leq Re_G \leq 12,000$). The LES results indicated that it is possible to reproduce with good accuracy most of the non-Newtonian fluid flow features using the Dynamic Smagorinsky model with a fine grid resolution.

Recently, Amani et al. (2021) proposed a closure model for the additional term, namely the Non-Newtonian SGS (NNSGS) stress tensor. Two canonical case studies were evaluated by including the Power-law viscosity model in Burgers turbulence. Inagaki (2021) assessed the effectiveness of a mixed SGS model, combining an isotropic eddy viscosity model and a scale-similarity model for Power-law fluids. The author follows the discussion of Ohta and Miyashita (2014) and also ignores the additional term imposed by the non-Newtonian stress tensor. The performance of the proposed model was tested in the plane channel flows and pipe flows for the power-law index of $0.5 \leq n \leq 1.15$.

1.4 Open Issues and Objectives of the Work

From the above literature review, it is clear that few studies have been conducted with LES focusing on the turbulent flows of viscoplastic fluids, Molla and Paul (2012) and Ohta and Miyashita (2014) addressed the subject briefly.

The main question that arises is whether SGS models based on the eddy viscosity hypothesis can provide satisfactory results for simulations with viscoplastic fluids at a low Bingham number (ratio of yield stress forces to viscous forces (ALEXANDROU et al., 2003)).

Therefore, this thesis aims to assess the performance of different SGS models for the turbulent flow of Herschel-Bulkley fluids. Two SGS models available in the literature are considered for this task: Dynamic Smagorinsky and Wall-Adapting Local Eddy-viscosity (WALE). The models will be evaluated based on predictions of first- and second-order turbulence statistics and flow features such as mean wall shear stress, mean wall viscosity, friction factor, mean shear rate, and mean viscosity profiles. Additionally, UDNS simulations will also be performed. Numerical results from each model will be compared with DNS performed using OpenFOAM and the spectral element-Fourier code *Semtex*.

Subsequently, the current methodology will be used to study the effects of rheological properties of Herschel-Bulkley fluids in a concentric annular section. The effects of the flow behavior index, Bingham number and the influence of the inner cylinder rotation on the flow characteristics will be evaluated.

1.5 Document Outline

This thesis is divided into six chapters: Chapter 2 presents a brief review of the concepts regarding non-Newtonian fluids and turbulent flows. The LES formulation, the approaches to modeling unresolved scales, and methods to quantify LES resolution are also exposed. Chapter 3 presents the numerical method employed in this thesis. The finite-volume discretization technique performed by the OpenFOAM code is described. In Chapter 4, the verification of the numerical method is discussed. First, simulations of the turbulent pipe flows of Newtonian and Herschel-Bulkley fluids are performed. Numerical simulations of turbulent flows of a Newtonian fluid in a concentric annular section with different inner cylinder rotations are also analyzed. Chapter 5 presents the results and discussions concerning the turbulent flows of Herschel-Bulkley fluids in a concentric annular region with inner cylinder rotation. Finally, the conclusions and recommendations of this thesis are exposed in Chapter 6.

2 THEORETICAL FORMULATION

This chapter presents the theoretical concepts used throughout this thesis. Section 2.1 describes the balance equations for an incompressible and isothermal flow. The basics concepts regarding Newtonian and non-Newtonian fluids are present in Section 2.2 and some non-dimensional parameters used in the current work are described in Section 2.3. Section 2.4 introduces a brief overview of turbulent flows features. The LES filtering process and sub-grid scale modeling are discussed in Section 2.5. Finally, in Section 2.6, some methods to assess the LES resolution are presented.

2.1 Balance Equations

In the Eulerian description, the governing principles in fluid mechanics can be derived using a control volume approach. For an incompressible and isothermal flow, the motion of a fluid is governed basically by the mass and momentum conservation equations (SAGAUT, 2006).

The mass conservation is described as

$$\nabla \cdot \mathbf{u} = 0 \tag{2.1}$$

where $\mathbf{u} = (u_i, u_j, u_k)^{\mathrm{T}}$ is the velocity vector.

$$\rho \left[\frac{\partial \mathbf{u}}{\partial t} + \mathbf{u} \cdot \nabla \mathbf{u} \right] = -\nabla p + \nabla \cdot \boldsymbol{\sigma} \tag{2.2}$$

where t indicates the time, ρ is the density, p is the pressure, and $\boldsymbol{\sigma}$ is the viscous stress tensor. Equations of motion in cylindrical coordinates are presented in Appendix A.

In order to complete the model's system of equations, it is necessary to introduce a constitutive equation, which describes the shear stress-shear rate relationship of a fluid.

2.2 Fluid Behavior

Newtonian fluids are those whose behavior can be described by Newton's law of viscosity, which establishes a linear relationship between the shear stress and shear rate for a given temperature and pressure. The viscous stress tensor $\boldsymbol{\sigma}$ for an incompressible Newtonian flow can be defined as (ASTARITA; MARRUCCI, 1974; SAGAUT et al., 2006)

$$\boldsymbol{\sigma} = 2\mu \mathbf{S} \tag{2.3}$$

where μ is the dynamic viscosity of the fluid and $\mathbf{S}$ is the rate-of-strain tensor, defined as

$$\mathbf{S} = \frac{1}{2}(\nabla \mathbf{u} + (\nabla \mathbf{u})^{\mathrm{T}}) \tag{2.4}$$

A fluid that does not obey Newton's law of viscosity is described as a Non-Newtonian fluid. The non-Newtonian fluids can be divided into three groups: Generalized Newtonian fluid (GNF), time-dependent fluids, and viscoelastic fluids (CHHABRA; RICHARDSON, 2008; DESHPANDE et al., 2010).

- Generalized Newtonian fluids are a subclass of non-Newtonian fluids in which the instantaneous shear stress of the material is determined purely by the local shear rate (BALMFORTH et al., 2014). The GNF also implies a time-independent viscosity and inelastic behavior.
- Fluids whose apparent viscosity also depends on the shear duration and their kinematic history are called time-dependent.
- Viscoelastic materials exhibit elastic as well as viscous behavior. In addition, after deformation shows partial elastic recovery.

It is worth mentioning that this classification is somewhat arbitrary in real fluids. Some fluids can exhibit a combination of properties from two or even all three groups (DESHPANDE et al., 2010).

In this thesis, the discussion will focus only on fluids characterized as GNF. For more details about the time-dependent fluids and viscoelastic fluids, the reader is referred to Bird et al. (1987), Macosko (1994), Chhabra and Richardson (2008), and Deshpande et al. (2010).

GNFs are divided into shear-thinning (pseudoplastic), shear-thickening (dilatant), and viscoplastic fluids. Shear-thinning fluids are characterized by an apparent viscosity that gradually decreases with an increasing shear rate. On the other hand, shear-thickening fluids enhance the apparent viscosity as the shear rate increases. Finally, the viscoplastic behavior is characterized by the existence of yield stress, τ_y, i. e. a viscoplastic fluid does not flow until the shear stress surpasses the yield stress value.

The Power-law model can represent both shear-thinning and shear-thickening fluids, whereas the Herschel-Bulkley model aims to represent viscoplastic fluids. Figure 2.1 shows the flow curves and shear stress in the shear rate function, for the Newtonian, Power-law, and Herschel-Bulkley models.

For a GNF, the apparent viscosity is a function of the shear rate magnitude. The viscous stress tensor is written as (ASTARITA; MARRUCCI, 1974)

$$\boldsymbol{\sigma} = 2\eta(|\dot{\gamma}|)\mathbf{S} \tag{2.5}$$

where η is the apparent viscosity, $|\dot{\gamma}|$ denotes the magnitude of the shear rate. The magnitude of the shear rate is defined as the second invariant of the rate-of-strain tensor, yielding

$$|\dot{\gamma}| = (2\mathbf{S} : \mathbf{S})^{1/2} \tag{2.6}$$

Figure 2.1 – Qualitative flow curves for Newtonian and non-Newtonian fluids.

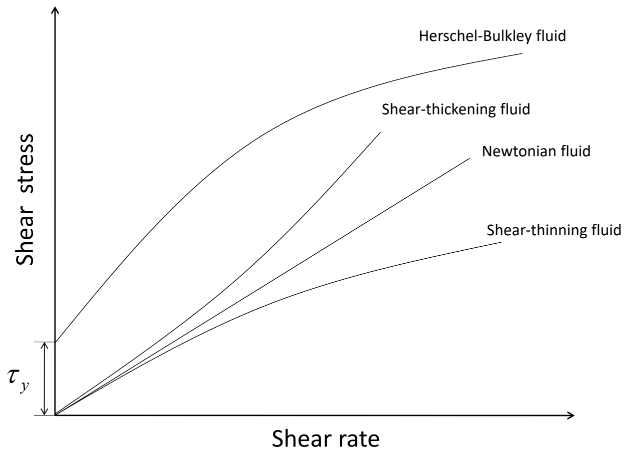

Source: Adapted from Bird et al. (1987).

The Herschel-Bulkley model is widely used to characterize the rheological behavior of drilling fluids (PEIXINHO et al., 2005). The apparent viscosity of the Herschel-Bulkley model is defined as (OSSWALD; RUDOLPH, 2015):

$$\begin{cases} \eta = \frac{\tau_y}{|\dot{\gamma}|} + K|\dot{\gamma}|^{n-1} & |\boldsymbol{\sigma}| > \tau_y \\ \eta \to \infty & |\boldsymbol{\sigma}| \leq \tau_y \end{cases} \tag{2.7}$$

where τ_y is the yield stress, K is the fluid consistency index, and n is the flow behavior index. For $n < 1$, the Herschel–Bulkley model presents the shear-thinning behavior (BIRD et al., 1987). When $\tau_y = 0$, Eq. 2.7 reduces to a Power-Law rheology model representing purely shear-thinning behavior.

2.3 Non-Dimensional Parameters

When the viscous stress tensor either for a Newtonian fluid or GNF (Eqs. 2.3 and 2.5) is introduced into Eq.(2.2) yields the Navier-Stokes equation,

$$\frac{\partial \mathbf{u}}{\partial t} + \mathbf{u} \cdot \nabla \mathbf{u} = -\frac{1}{\rho}\nabla p + \nabla \cdot \left[\nu(\nabla \mathbf{u} + (\nabla \mathbf{u})^{\mathrm{T}})\right] \tag{2.8}$$

where ν is the kinematic viscosity, and it is defined as $\nu = \mu/\rho$ for a Newtonian fluid or $\nu = \eta/\rho$ for a GNF.

The Navier-Stokes equation expresses the equilibrium condition between inertial forces (left-hand side) and surface forces, represented by the pressure field and viscous stress tensor (right-hand side) acting on the fluid particle (SCHILICHTING, 1979; DAVIDSON, 2004).

A significant dimensionless quantity that arises naturally when governing equations (Eqs. 2.1 and 2.8) are transformed into dimensionless form is the Reynolds number (Re), which describes the ratio of inertial forces to viscous forces. The Reynolds number is defined as

$$Re = \frac{\rho U_b L}{\mu} \tag{2.9}$$

where U_b is the fluid bulk velocity and L is the characteristic length.

The Reynolds number is used to differentiate between the laminar and turbulent fluid flow. Considering the example of a pipe flow, it is assumed that $Re \leq 2,100$ denotes a laminar flow, whereas $Re \geq 2,300$ indicates that the flow is turbulent.

Commonly, the Reynolds number used for GNFs is based on the mean wall viscosity η_w (RUDMAN; BLACKBURN, 2006; SINGH et al., 2017b). Then, the dynamic viscosity of Eq 2.9 is replaced by η_w. For a Herschel-Bulkley fluid, the mean wall viscosity is defined as (SINGH et al., 2017b)

$$\eta_w = \frac{K^{1/n}\, \tau_w}{(\tau_w - \tau_y)^{1/n}} \tag{2.10}$$

where τ_w is the mean wall shear stress. For instance, for a given mean pressure gradient $\partial P / \partial z$, the τ_w can be calculated as

$$\tau_w = -\frac{D}{4}\frac{\partial P}{\partial z} \tag{2.11}$$

where D is the pipe diameter.

Using the mean wall viscosity scale, the generalized Reynolds number Re_G is written as (RUDMAN; BLACKBURN, 2006; SINGH et al., 2017b)

$$Re_G = \frac{\rho U_b L}{\eta_w} \tag{2.12}$$

Two dimensionless parameters arise for Herschel-Bulkley fluid flows. The Hedstrom number, He, determines the flow behavior of yield stress fluids (MALIN, 1998).

$$He = \frac{\rho L^2\, \tau_y^{(2/n-1)}}{K^{2/n}} \tag{2.13}$$

Additionally, the Bingham number, Bn, relates the ratio of the yield stress forces to viscous forces (ALEXANDROU et al., 2003)

$$Bn = \frac{\tau_y L^n}{K U_b^n} \tag{2.14}$$

2.4 Turbulence

2.4.1 A Brief Discussion of Turbulence

Turbulent flows usually arise from instabilities when inertial forces surpass the influence of viscous effects. These instabilities produce fluctuations in the velocity field and grow chaotically, leading to a fully turbulent flow. Nevertheless, the turbulent flows are highly dissipative and need a continuous energy supply. If energy is not supplied, turbulence decay rapidly, and the flow becomes laminar again due to the viscous effects. A typical energy source for velocity fluctuations is shear in the mean flow (TENNEKES; LUMLEY, 1978) (TENNEKES and LUMLEY, 1978).

As mentioned in Section 1.2, any turbulent flow quantity, such as the velocity field, can be characterized by the Reynolds decomposition. Thus, the instantaneous velocity $\mathbf{u}(\mathbf{x}, t)$ is expressed as the sum of a mean velocity $\bar{\mathbf{u}}(\mathbf{x})$, obtained from a statistical average and a fluctuating contribution $\mathbf{u}'(\mathbf{x}, t)$ (WILCOX, 1993).

$$\mathbf{u}(\mathbf{x}, t) = \bar{\mathbf{u}}(\mathbf{x}) + \mathbf{u}'(\mathbf{x}, t). \tag{2.15}$$

$$\bar{\mathbf{u}}(\mathbf{x}) = \lim_{T \to \infty} = \frac{1}{T} \int_{t}^{t+T} \mathbf{u}(\mathbf{x}, t) dt \tag{2.16}$$

The time average of the fluctuation part of the velocity field is zero (WILCOX, 1993).

$$\bar{\mathbf{u}}'(\mathbf{x}, t) = \lim_{T \to \infty} = \frac{1}{T} \int_{t}^{t+T} [\mathbf{u}(\mathbf{x}, t) - \bar{\mathbf{u}}(\mathbf{x})] dt = 0 \tag{2.17}$$

The turbulent kinetic energy (TKE) per unit mass defined by the mean value of the turbulent velocity fluctuations is given by (WILCOX, 1993)

$$k = \frac{1}{2}\overline{u_i' u_i'} = \frac{1}{2}(\overline{u_i'^2} + \overline{u_j'^2} + \overline{u_k'^2}) \tag{2.18}$$

Two features of turbulent flows stand out: the capability to mix or transport properties and the existence of a wide range of eddies. First, the ability to mix fluid directly impacts the rates of momentum, heat, and mass transfer; these quantities rapidly disperse across the flow. On the other hand, in a laminar flow, these substances would be transported along streamlines of the flow and slowly diffuse by molecular transport (TENNEKES; LUMLEY, 1978; DURBIN; PETTERSSON-REIF, 2015).

The second issue is that the turbulent flows are characterized by a wide range of eddies with different length and time scales, and energy and momentum transfer are essentially affected by inertial processes (BAYLY et al., 1988). The large eddies are the most energetic, interact with the mean flow, and they are dependent on geometry and boundaries conditions; while the small scales contain little energy, they are considered isotropic and can be described by a Gaussian probability density function (LESIEUR et al., 2005; RODI et al., 2013).

The large scales extract energy from the mean motion and transfer their energy toward smaller eddies until the size of the smallest scales of turbulence is so tiny that their structure can no longer subsist to the molecular viscosity action. This mechanism is known as the *energy cascade* and it was introduced by Richardson (1922). The *energy cascade* process is illustrated in Figure 2.2. The viscous stress effects in large eddies are negligible. The cascade ends when the eddy size becomes so small that Re, based on the size of the smallest eddies, is of order unity. The viscous forces become significant, and dissipation becomes important (DAVIDSON, 2004).

Figure 2.2 – Schematic representation of the energy cascade. Terms u and l represent the typical velocity and length scales associated with the largest eddies. Terms ϑ and η_k correspond to the velocity scales and characteristic length of the smallest structures, respectively.

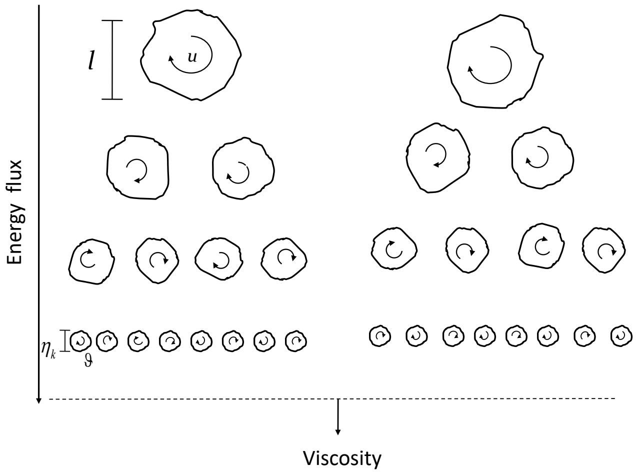

Source: Adapted from Davidson (2004).

The distribution of TKE from the different length scales is usually expressed by the energy spectrum in wave number domain $\mathrm{E(k)}$ (SAGAUT et al., 2006). The TKE is related to the energy spectrum in the wave number space $\mathrm{E(k)}$ as

$$k = \frac{1}{2}\overline{u_i' u_i'} = \int_0^\infty \mathrm{E(k)} d\mathrm{k} \tag{2.19}$$

where k is the wave number, given by

$$\mathrm{k} = \frac{\omega_{eddie}}{u} = \frac{2\pi}{l} \tag{2.20}$$

Here ω_{eddie} is the angular frequency associated with the rotation of a turbulent scale, which can be expressed as $\omega_{eddie} = 2\pi/\Upsilon$, where the lifespan of eddies is given by the turn-over time $\Upsilon = l/u$ (DAVIDSON, 2004). The TKE spectrum is depicted in Figure 2.3.

The first region of Figure 2.3, the *energy-containing range*, consists of the largest eddies where the mean flow generates the turbulence energy. The largest scales of turbulence are subject to inertial instabilities and quickly break up into small vortices. The rate at which energy (per unit mass) is passed down to the smaller scales is defined as

Figure 2.3 – Typical representation of the energy spectrum of a turbulent flow.

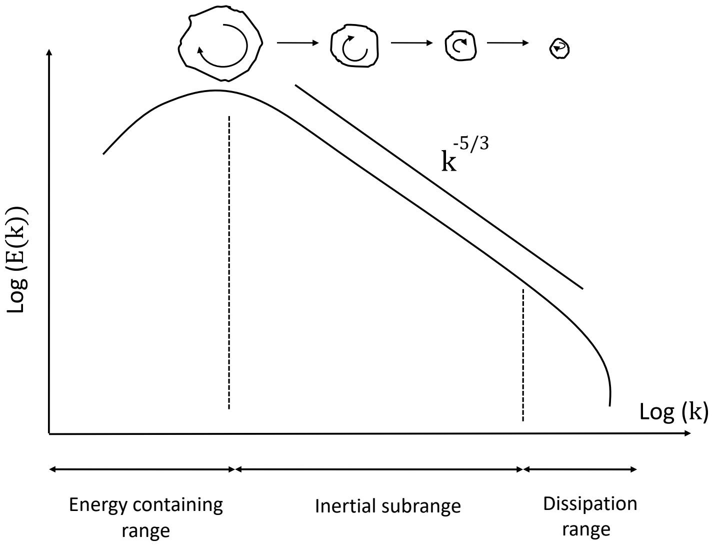

Source: Adapted from Sagaut et al. (2006).

$$\Pi \sim \frac{u^2}{l/u} = \frac{u^3}{l} \tag{2.21}$$

In the *inertial subrange*, whose extent of this spectrum is conditioned to the Reynolds number, the size of turbulent scales is small compared to l but large compared to η_k. In this range, the energy is neither fed from the mean motion nor dissipated by viscous forces but only transferred from the larger to the smaller eddies. Based on the Kolmogorov hypothesis, the energy spectrum $\mathrm{E(k)}$ in the inertial subrange decreases following the $\mathrm{k}^{-5/3}$ relation, and it is defined as:

$$\mathrm{E(k)} = K_o \varepsilon^{2/3} \mathrm{k}^{-5/3} \tag{2.22}$$

where K_0 is the Kolmogorov constant, ranging between 1.4 – 1.7 (SAGAUT et al., 2006).

In statistically steady turbulence, the rate of energy dissipation in the smallest scales, ε, must be equivalent to the Π (DAVIDSON, 2004)

$$\varepsilon \approx \Pi \sim \frac{u^3}{l} \tag{2.23}$$

At the smallest scales of turbulence, the viscous effect becomes significant, and the rate of energy dissipation is given by

$$\varepsilon = 2\nu S_{ij} S_{ij} \sim \nu \frac{\vartheta^2}{\eta_k^2} \tag{2.24}$$

where the rate-of-strain tensor associated with the smallest eddies can be evaluated by

$$S_{ij} \sim \frac{\vartheta}{\eta_k} \tag{2.25}$$

Since the energy is transferred without loss, combining Eq. 2.6 and 2.7 gives:

$$\frac{u^3}{l} \approx \nu \frac{\vartheta^2}{\eta_k^2} \tag{2.26}$$

In addition, the local Reynolds number in the smallest scales is expressed by

$$Re_{\eta_k} = \frac{\vartheta \eta_k}{\nu} \sim 1 \tag{2.27}$$

From Eqs. (2.26) and (2.27), it is possible to derive expressions to estimate the Kolmogorov's micro scales (DAVIDSON, 2004).

$$\eta_k = l Re^{-3/4} \sim \frac{\nu^3}{\varepsilon} \tag{2.28}$$

$$\vartheta = u Re^{-1/4} \sim (\nu\varepsilon)^{1/4} \tag{2.29}$$

2.4.2 Turbulent Kinetic Energy Budget

The TKE budget, which can describe the physical processes that govern the turbulent flow is directly related to the mechanisms that generate, transport and dissipate turbulence (NASEEM et al., 2019).

Compared with a Newtonian fluid, the non-uniform viscosity and viscosity fluctuations modify the TKE budget equation for a non-Newtonian fluid. According to Singh et al. (2017b), an equation for the ensemble-average TKE for GNF is written as:

$$\begin{aligned}\overbrace{\frac{\partial k}{\partial t}}^{k_t} + \overbrace{U_j \frac{\partial k}{\partial x_j}}^{A} = \overbrace{-\overline{u'_i u'_j} S_{ij}}^{P_t} + \left\{ \overbrace{-\frac{1}{2}\frac{\partial \overline{u'_i u'_i u'_j}}{\partial x_j}}^{T_t} - \overbrace{\frac{\partial \overline{p' u'_j}}{\partial x_j}}^{\zeta} + \overbrace{\frac{\partial (2\overline{\nu}\,\overline{s'_{ij} u'_i})}{\partial x_j}}^{D_t} \right\} - \overbrace{2\overline{\nu}\,\overline{s'_{ij} s'_{ij}}}^{\epsilon} \\ + \left\{ \overbrace{\frac{\partial (2\overline{\nu' u'_i} S_{ij})}{\partial x_j}}^{\varsigma_{nn}} + \overbrace{\frac{\partial (\overline{2\nu' s'_{ij} u'_i})}{\partial x_j}}^{D_{nn}} \right\} \overbrace{-2\overline{\nu' s'_{ij}} S_{ij}}^{\chi_{nn}} - \overbrace{-2\overline{\nu' s'_{ij} s'_{ij}}}^{\epsilon_{nn}}\end{aligned} \tag{2.30}$$

In order to simplify the notation, the suffix notation was used here. The terms in the first row appear for both Newtonian and non-Newtonian fluids, and the following is the standard terminology:

k_t: rate of change of turbulence kinetic energy;

A: mean flow advection;

P_t: turbulent kinetic energy production;

T_t: turbulent velocity transport;

ζ: pressure-related transport;

D_t: mean viscous transport;

ϵ: mean viscous dissipation.

The terms in the second row are zero for a Newtonian fluid and appear only for non-Newtonian fluids. SINGH et al. (2017) defined the following terminology for these terms:

ς_{nn}: mean shear turbulent viscous transport;

D_{nn}: turbulent viscous transport;

χ_{nn}: mean shear turbulent viscous dissipation;

ϵ_{nn}: turbulent viscous dissipation.

When the terms of similar nature are summed together, the TKE budget equation can be written as (SINGH et al., 2017b)

$$\frac{Dk}{Dt} = P + T^k + \epsilon^k \tag{2.31}$$

where $T^k = T_t + \zeta + D_t + \varsigma_{nn} + D_{nn}$ is the total transport and $\epsilon^k = \epsilon + \chi_{nn} + \epsilon_{nn}$ is the total dissipation.

2.5 Large-Eddy Simulations

2.5.1 The Filtering Procedure

As briefly mentioned in the introduction, the large scales of fluid motion are solved explicitly in LES, while the small ones are modeled. In order to separate these scales, a filtering operation is performed. Ideally, this separation happens in a spectral region where only energy transfer occurs, no action by production and dissipation (SAGAUT et al., 2006; RODI et al., 2013). In Figure 2.4, an energy spectrum is illustrated for DNS and LES. The cut-off wave-number $\mathrm{k}_{cut-off}$ represents the separation between resolved and unresolved scales.

Mathematically, the filtering operation corresponds to the convolution of any flow quantity $f(\mathbf{x},t)$ by the filter function $G(\mathbf{x},\mathbf{x}',\Delta)$ in the form (LESIEUR et al., 2005)

$$\tilde{f}(\mathbf{x},t) = \int_D f(\mathbf{x}',t)\; G(\mathbf{x},\mathbf{x}',\Delta) dV' \tag{2.32}$$

where $\tilde{f}(\mathbf{x},t)$ is the resolved (filtered) part of $f(\mathbf{x},t)$, $\mathbf{x}$ is the location where $\tilde{f}$ is determined, $\mathbf{x}'$ is the position where f is considered in the spatial integration, D is the domain where the integration is performed, and Δ is the filter width (PIOMELLI, 1999; RODI et al., 2013). The specified function G satisfies the normalization condition (POPE, 2000; SAGAUT, 2006).

$$\int_D G(\mathbf{x},\mathbf{x}',\Delta) dV' = 1 \tag{2.33}$$

The unresolved field of $f(\mathbf{x},t)$, denoted by $f'(\mathbf{x},t)$ is a representation of the small scales of the flow, often known as subgrid scales, which are smaller than Δ and it is defined as (LESIEUR et al., 2005; SAGAUT, 2006)

Figure 2.4 – Concept of LES regarding the energy spectrum.

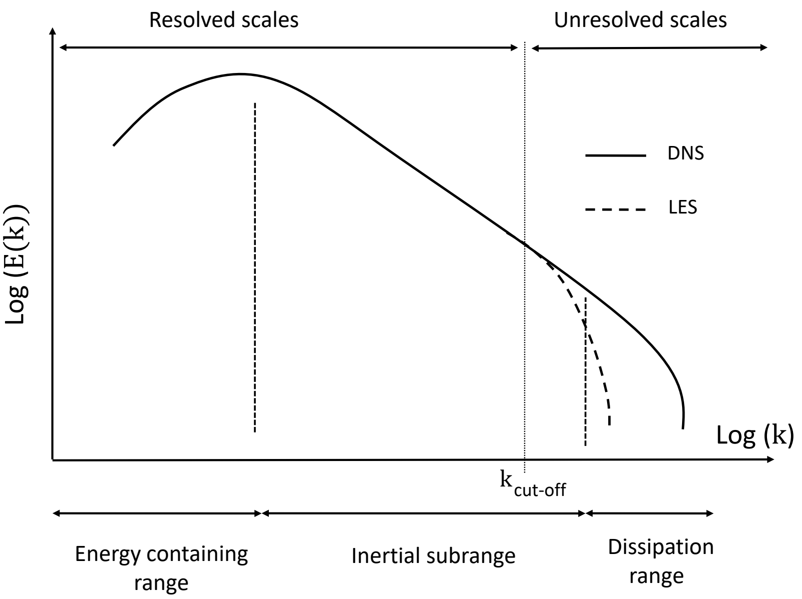

Source: Adapted from Rodi et al. (2013).

$$f'(\mathbf{x},t) = f(\mathbf{x},t) - \tilde{f}(\mathbf{x},t) \tag{2.34}$$

It is worth mentioning that the filter G is not a Reynolds type operator since the following properties of this type of operator are not satisfied in general (DAVIDSON, 2004; SAGAUT, 2006):

$$\tilde{\tilde{f}}(\mathbf{x},t) \neq \tilde{f}(\mathbf{x},t) \tag{2.35}$$

$$\tilde{f'}(\mathbf{x},t) \neq 0 \tag{2.36}$$

where $\tilde{\tilde{f}}(\mathbf{x},t)$ and $\tilde{f'}(\mathbf{x},t)$ are referred to as double-filtered variable and filtered residual variable, respectively.

The filters commonly employed to separate scales are the Top-Hat (box) filter, Gaussian filter, and the Sharp or Spectral cut-off filter (PIOMELLI, 1999; POPE, 2000; SAGAUT, 2006). The convolution filters $G(\mathbf{x})$ in the physical space and their corresponding transfer function $\hat{G}(\mathrm{k})$ in the Fourier space (frequency domain) are described in Table 2.1.

The graphical representation of the three filters in physical and Fourier space is shown in Figure 2.5. The top-hat filter is local in the physical space and non-local in the Fourier space, inversely to the sharp cut-off filter, which is local in the spectral space and non-local in the physical space. As for the Gaussian filter is non-local both in the physical and Fourier spaces (SAGAUT, 2006) because the Fourier transform of a Gaussian function is also a Gaussian.

Table 2.1 – Filter functions and transfer functions (POPE, 2000).

Name	**Filter Function**	**Transfer Function**
-	$G(\mathbf{x})$	$\widehat{G}(\mathrm{k}) \equiv \int_{-\infty}^{\infty} \mathrm{e}^{\mathrm{ikr}}\, G(\mathbf{x})dx$
Top-Hat (box) filter	$G(\mathbf{x})= \begin{cases} 1/\Delta \text{ if } \lvert x\rvert \quad \leq \Delta/2 \\ 0 \quad \text{otherwise} \end{cases}$	$\widehat{G}(\mathrm{k}) = \frac{\sin(\mathrm{k}\ \Delta/2)}{\mathrm{k}\ \Delta/2}$
Gaussian Filter	$G(\mathbf{x})= \sqrt{\frac{6}{\pi\Delta^2}}\exp\left(-\frac{6x^2}{\Delta^2}\right)$	$\widehat{G}(\mathrm{k}) = \exp\left(-\frac{\mathrm{k}\ \Delta^2}{24}\right)$
Sharp or Spectral cut-off filter	$G(\mathbf{x}) = \frac{\sin(\mathrm{k_c}(x))}{\mathrm{k_c}(x)}$, with $\mathrm{k_c} = \frac{\pi}{\Delta}$	$\widehat{G}(\mathrm{k}) = \begin{cases} 1/\Delta \text{ if k} \quad \leq \pi \\ 0 \quad \text{otherwise} \end{cases}$

Source: Adapted from Pope (2000).

The top-hat filter for being local in physical space, a simple average over a rectangular region (DE VILLIERS, 2006), is used implicitly in the finite volume method. In this approach, the filter cut-off width Δ is defined by the computational mesh size and determines the scales of the fluid motion that are filtered out.

The sharp cut-off filter is typically used in conjunction with spectral methods. In Fourier space, the filtering operation affects only scales above a defined cut-off wave number (PIOMELLI, 1999).

The difference between the exact solution and the energy spectrum modification of a test function performed by the filtering operators is depicted in Figure 2.6. The top-hat and Gaussian filters give similar results. Both filters smooth the resolved and unresolved scales, while the sharp cut-off filter clearly separates the scale fluctuations (PIOMELLI, 1999; SAGAUT, 2006).

Applying the filtering operation to the governing equations (Eqs. (2.1) and (2.8)), one obtains the filtered equations (SAGAUT, 2006; RODI et al., 2013)

$$\nabla \cdot \tilde{\mathbf{u}} = 0 \tag{2.37}$$

$$\frac{\partial \tilde{\mathbf{u}}}{\partial t} + \nabla \cdot (\widetilde{\mathbf{u} \otimes \mathbf{u}}) = -\frac{1}{\rho}\nabla \tilde{p} + \nabla \cdot \tilde{\boldsymbol{\sigma}} \tag{2.38}$$

where quantities with an $\widetilde{(\ )}$ are filtered (resolved) components.

The non-linear term $\mathbf{u} \otimes \mathbf{u}$ in the Navier-Stokes equation (Eq. 2.38) produces the filtered product $\widetilde{\mathbf{u} \otimes \mathbf{u}}$ in the convective term (POPE, 2000). Since $\widetilde{\mathbf{u} \otimes \mathbf{u}} \neq \tilde{\mathbf{u}} \otimes \tilde{\mathbf{u}}$, the SGS stress tensor $\boldsymbol{\tau}^{SGS}$ arises from the difference between the two sides of this inequality. $\boldsymbol{\tau}^{SGS}$ is defined as (POPE, 2000; SAGAUT et al., 2006)

$$\boldsymbol{\tau}^{SGS} = \widetilde{\mathbf{u} \otimes \mathbf{u}} - \tilde{\mathbf{u}} \otimes \tilde{\mathbf{u}} \tag{2.39}$$

Figure 2.5 – Typical filter functions. Boxfilter: representation in physical space (a) and Fourier space (b). Gaussian filter: representation in physical space (c) and Fourier space (d). Sharp cut-off filter: representation in physical space (e) and Fourier space (f).

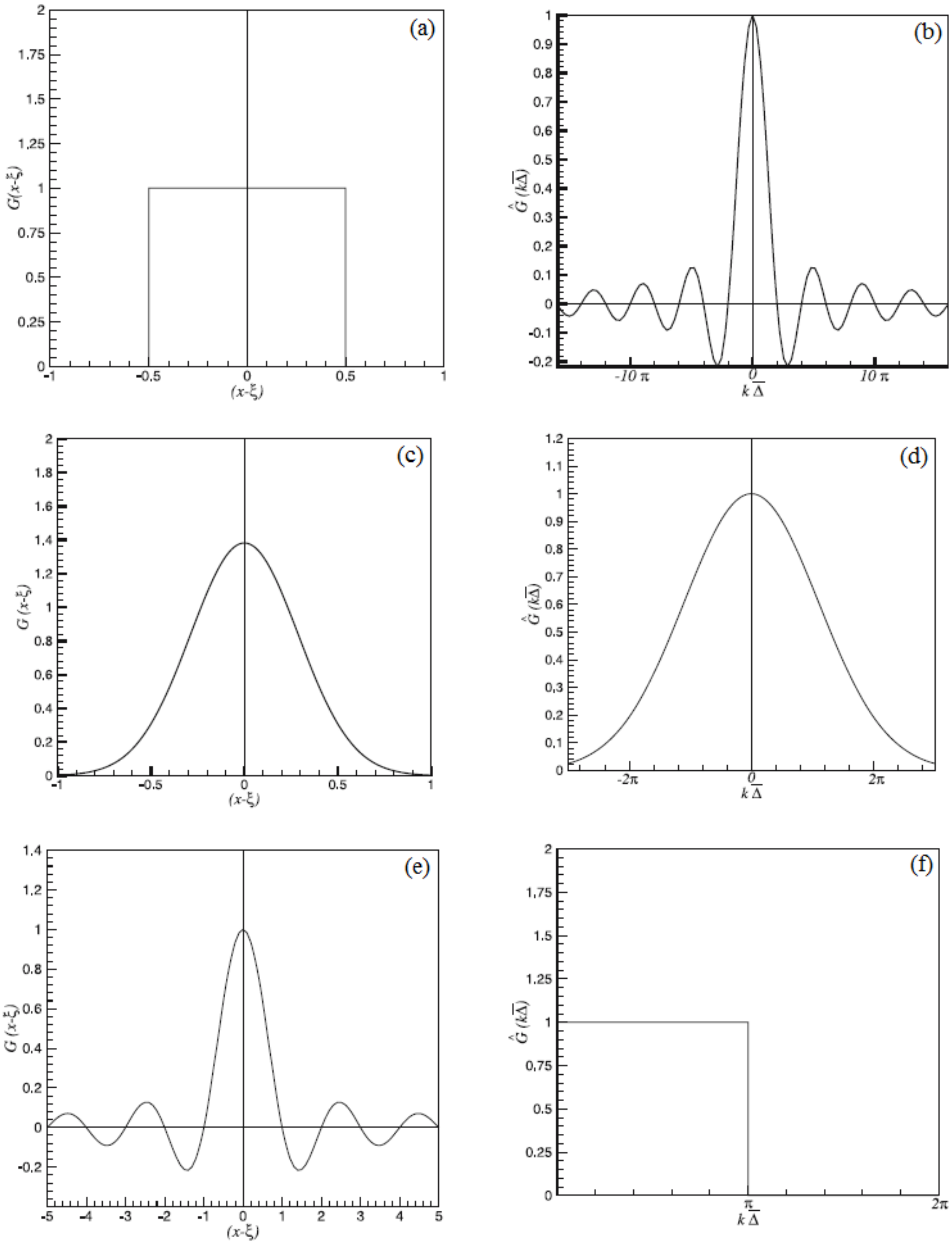

Source: Adapted from Sagaut (2006).

The SGS stress tensor represents all the interaction between the subgrid (unresolved) and the filtered scales (LESIEUR et al., 2005; SAGAUT, 2006). Currently, two different methods of accounting for SGS stresses are found in the literature (SAGAUT, 2006):

Figure 2.6 – Energy spectrum of the unfiltered and filtered solutions for the same cut-off wave number $\mathrm{k}_{cut-off} = 60$.

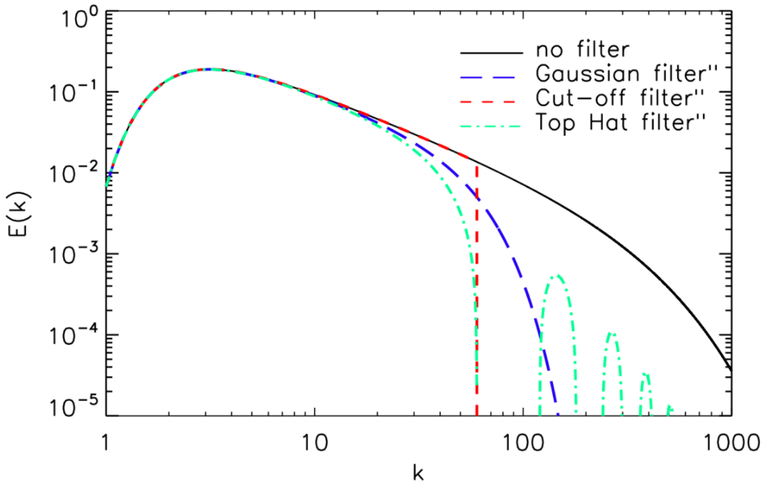

Source: Adapted from Laval (2020).

- Explicit modeling: This approach derives a model that correctly drains the energy from the resolved to unresolved scales, mimicking the process associated with the energy cascade.
- Implicit inclusion: The effects of unresolved scales are incorporated implicitly via a numerical scheme by arranging it, so the truncation error induces the desired effects.

In the present thesis, the $\boldsymbol{\tau}^{SGS}$ effect will be treated explicitly. Therefore, Eq. (2.38) can be rewritten as (OHTA; MIYASHITA, 2014; AMANI et al., 2021)

$$\frac{\partial \tilde{\mathbf{u}}}{\partial t} + \nabla \cdot (\tilde{\mathbf{u}} \otimes \tilde{\mathbf{u}}) = -\frac{1}{\rho}\nabla \tilde{p} + \nabla \cdot \tilde{\boldsymbol{\sigma}} - \nabla \cdot \boldsymbol{\tau}^{SGS} + \nabla \cdot \boldsymbol{\tau}^{NNSGS} \tag{2.40}$$

Note that when the spatial filtering process is applied to the governing equations for a GNF an additional term, $\boldsymbol{\tau}^{\boldsymbol{NNSGS}} = \widetilde{\boldsymbol{\sigma}(\mathbf{S})} - \boldsymbol{\sigma}(\widetilde{\mathbf{S}})$, is derived because the viscous stress tensor is a non-linear function of the rate-of-strain tensor (OHTA; MIYASHITA, 2014; AMANI et al., 2021).

As mentioned in the literature review, Ohta and Miyashita (2014) showed that $\boldsymbol{\tau}^{\boldsymbol{NNSGS}}$ is much smaller than the SGS stress, and its amplitude is negligible compared with the error associated with the SGS model. Therefore, following the arguments of Ohta and Miyashita (2014) this additional term is also disregarded in the present study, and only the SGS stress tensor is modeled.

For the simulations involving the UDNS, the terms $\boldsymbol{\tau}^{SGS}$ and $\boldsymbol{\tau}^{NNSGS}$ of Eq. (2.40) vanish and the balance equations are solved directly.

2.5.2 Subgrid-Scale Modeling

The most popular models for computing SGS stresses employ the eddy viscosity hypothesis (DAVIDSON, 2004; SAGAUT, 2006; RODI et al., 2013). Using the eddy viscosity assumption, $\boldsymbol{\tau}^{SGS}$ is decomposed into anisotropic and an isotropic component (RODI et al., 2013). For simplification, assuming the suffix notation the $\boldsymbol{\tau}^{SGS}$ is defined as

$$\boldsymbol{\tau}^{SGS} = \tau_{ij}^{SGS} = \tau_{ij}^{SGS,a} + \frac{1}{3}\tau_{kk}^{SGS}\delta_{ij} \tag{2.41}$$

where $\tau_{ij}^{SGS,a}$ is the anisotropic SGS stress tensor, τ_{kk}^{SGS} is the component ofthe SGS normal stresses and δ_{ij} denotes the Kronecker delta. The isotropic part contains the sum of the SGS normal stresses, whose value is equal to two times the SGS kinetic energy and acts like a pressure term (POPE, 2000; RODI et al., 2013).

The isotropic part of τ_{ij}^{SGS} is added to the filtered pressure term, which leads to a new pressure variable (POPE, 2000; RODI et al., 2013)

$$\tilde{P} = \tilde{p} + \frac{1}{3}\tau_{kk}^{SGS} \tag{2.42}$$

The anisotropic SGS stress tensor is defined as

$$\tau_{ij}^{SGS,a} = -2\nu_{SGS}\tilde{S}_{ij} \tag{2.43}$$

where ν_{SGS} is the eddy viscosity of the SGS motions and $\tilde{S}_{ij}$ is the filtered rate-of-strain tensor (POPE, 2000; RODI et al., 2013)

$$\tilde{S}_{ij} = \frac{1}{2}\left(\frac{\partial \tilde{u}_i}{\partial x_j} + \frac{\partial \tilde{u}_j}{\partial x_i}\right) \tag{2.44}$$

The eddy viscosity is not a fluid property and can be estimated through dimensional analysis, similar to Prandtl's mixing length model (SAGAUT, 2006; RODI et al., 2013).

In the present thesis, two SGS models are used to model the SGS stress tensor: Dynamic Smagorinsky and WALE. Both models are based on the eddy viscosity assumption.

Dynamic Smagorinsky model

The Dynamic Smagorinsky model was proposed by Germano et al. (1991). The eddy viscosity is defined according to the model developed by Smagorinsky (1963),

$$\nu_{SGS} = (C_s\Delta)^2|\tilde{S}| \tag{2.45}$$

where C_s is the model constant, Δ is the filter width, and $|\tilde{S}| = \sqrt{2\tilde{S}_{ij}\tilde{S}_{ij}}$ is the magnitude of the filtered rate-of-strain tensor.

To dynamically calculate C_s, Germano et al. (1991) suggested introducing a second filter $\widehat{\Delta}$ (the test filter) wider than the grid filter Δ. The test filter is commonly defined as $\widehat{\Delta} = 2\Delta$. The SGS-test-filter stress tensor T_{ij}^{SGS} is defined as (GERMANO et al., 1991)

$$T_{ij}^{SGS} = \widehat{\widetilde{u_i u_j}} - \widehat{\tilde{u}}_i\widehat{\tilde{u}}_j \tag{2.46}$$

where quantities with $\widehat{\cdot}$ are test-filtered.

An exact relation can relate subgrid tensors corresponding to two different filtering levels (SAGAUT, 2006), this approach in the literature refers to Germano identity

$$L_{ij} = T_{ij}^{SGS} - \widehat{\tau}_{ij}^{SGS} = \widehat{\tilde{u}_i \tilde{u}_j} - \widehat{\tilde{u}}_i \widehat{\tilde{u}}_j \tag{2.47}$$

Assuming the same functional form to calculate the resolved turbulent stresses L_{ij}, the ν^{SGS} expressed in Eq. (2.45) can be used to parametrize both T_{ij}^{SGS} and τ_{ij}^{SGS}

$$\begin{aligned} \tau_{ij}^{SGS} - \frac{1}{3}\tau_{kk}^{SGS}\delta_{ij} &= -2\ (C_s\,\Delta)^2\,|\tilde{S}|\tilde{S}_{ij} \\ T_{ij}^{SGS} - \frac{1}{3}T_{kk}^{SGS}\delta_{ij} &= -2\ \left(C_s\,\widehat{\Delta}\right)^2\,|\widehat{\tilde{S}}|\widehat{\tilde{S}}_{ij} \end{aligned} \tag{2.48}$$

By inserting Eq. 2.48 into Eq.2.47, an equation for C_s is obtained:

$$L_{ij} - \frac{1}{3}L_{kk}\delta_{ij} = -2\,C_s^2\,M_{ij} \tag{2.49}$$

where

$$M_{ij} = \widehat{\Delta}^2 \left|\widehat{\tilde{S}}\right| \widehat{\tilde{S}}_{ij} - \Delta^2 \widehat{\left|\tilde{S}\right| \tilde{S}_{ij}} \tag{2.50}$$

Lilly (1992) presented the least-squares method to determine the value of C_s (Eq. 2.49), yielding

$$C_s^2 = -\frac{1}{2}\,\frac{\langle L_{ij}M_{ij}\rangle}{\langle M_{ij}M_{ij}\rangle} \tag{2.51}$$

WALE

The WALE model was proposed by Nicoud and Ducros (1999), and it calculates the eddy viscosity based on the square of the velocity gradient tensor. It is defined by (NICOUD; DUCROS, 1999)

$$\nu_{SGS} = (C_w\Delta)^2\,\frac{(S_{ij}^d S_{ij}^d)^{3/2}}{(\bar{S}_{ij}\bar{S}_{ij})^{5/2} + (S_{ij}^d S_{ij}^d)^{5/4}} \tag{2.52}$$

where S_{ij}^d is the traceless, symmetric tensor of the square of the velocity gradient tensor

$$S_{ij}^d = \frac{1}{2}\left(\frac{\partial \bar{u}_k}{\partial x_i}\frac{\partial \bar{u}_j}{\partial x_k} + \frac{\partial \bar{u}_k}{\partial x_j}\frac{\partial \bar{u}_i}{\partial x_k}\right) - \frac{1}{3}\delta_{ij}\frac{\partial \bar{u}_k}{\partial x_k}\frac{\partial \bar{u}_k}{\partial x_k} \tag{2.53}$$

A way to determine this constant is to assume that the WALE model gives the same ensemble-average subgrid kinetic energy dissipation as the classical Smagorinsky model (NICOUD; DUCROS, 1999). The filter width Δ is computed as the cubic root of the computational cell volume. The WALE model was designed to provide predictions similar to the Dynamic Smagorinsky model. The latter also provides the correct near-wall asymptotic behavior ($\nu_{SGS} = y^3$) through its dependence on L_{ij}, while the WALE formulation does not require explicit filtering or damping functions (DURBIN; PETTERSSON-REIF, 2015).

2.6 LES Resolution

There are different ways to estimate the resolution of LES data. However, there is no consensus on which method would be the ideal in the literature. In LES, there is no concept of grid independence because a grid-independent LES is essentially a DNS (CELIK et al., 2005; DURBIN; PETTERSSON-REIF, 2015).

A common approach to quantify the LES accuracy is *a-posteriori* validation. DNS and/or experimental data concerning turbulence statistics for several canonical problems, such as homogeneous isotropic turbulence, periodic channel flow, and periodic pipe flow are available in the literature for comparison and validation.

The spatial grid resolution is essential in the LES because it provides a perception of accuracy. As the computational grid is refined, smaller and smaller turbulent structures are resolved, and the simulation moves towards a DNS.

Regarding non-dimensional wall units for LES, the near-wall flow can either be modeled as in a RANS approach or resolved as in the DNS. For a wall-resolved LES in a turbulent boundary layer, Jiang and Lai (2009) and Zang (1991) mention that the grid size must satisfy $\Delta y^+_{wall} < 1$ for the first volume near the wall and contain 3 to 5 grid elements between the wall and the region of the wall coordinate $y^+ = 10$.

Jiang and Lai (2009) summarize that there are three levels of grid resolution for LES in the streamwise Δx^+ and spanwise Δz^+ directions for a turbulent boundary layer: poor resolution with $\Delta x^+ \geq 100$ and $\Delta z^+ \geq 30$; medium resolution with $50 \leq \Delta x^+ < 100$ and $12 \leq \Delta z^+ < 30$; high resolution with $\Delta x^+ < 50$ and $\Delta z^+ < 12$.

According to Montreuil (2000), typical LES high-resolution requirements for a simple periodic channel flow is $\Delta x^+ \approx 35$ and $\Delta z^+ \approx 10$, Menter (2012) suggests $\Delta x^+ \approx 40$ and $\Delta z^+ \approx 20$. For instance, Kim et al. (1987) argue that the required resolution for a DNS in a periodic channel flow is $\Delta x^+ = 8$ and $\Delta z^+ = 4$. In the wall-normal direction, leastways three grid points below $\Delta y^+_{wall} = 1$ and at least 10 grid elements up to $y^+_{wall} = 10$. Zheng et al. (2019) performed DNS of turbulent pipe flow of non-Newtonian fluids using a mesh resolution with $\Delta y^+_{wall} = 0.5$, $\Delta z^+ = 9.4$ (streamwise in cylindrical coordinate) and $R\Delta\theta^+ = 5.7$ (spanwise in cylindrical coordinate).

The non-dimensional cell sizes in Cartesian coordinates are defined as

$$\Delta y^+ = \frac{u_\tau \Delta y}{\nu} \tag{2.54}$$

$$\Delta x^+ = \frac{u_\tau \Delta x}{\nu} \tag{2.55}$$

$$\Delta z^+ = \frac{u_\tau \Delta z}{\nu} \tag{2.56}$$

where Δy, Δx and Δz represent the spatial mesh size in y, x and z directions, respectively, and u_τ is the friction velocity defined as $u_\tau = \sqrt{\tau_w/\rho}$.

Pope (2000) introduced a parameter M to estimate the amount of resolved turbulent kinetic energy by a simulation. This variable is the ratio of the resolved turbulent kinetic energy to the modeled one, defined as

$$M = \frac{k_{res}}{k_{res} + k_{SGS}} \tag{2.57}$$

where k_{res} and k_{SGS} are the resolved and modeled turbulent kinetic energy, respectively.

The value of M ranges from 0 to 1. If $M = 1$, the simulation corresponds to DNS and indicates that the flow is very well resolved, while for M approaching zero tends to a RANS simulation. Pope (2000) suggests $M \geq 0.8$ as the minimum resolution to achieve a good result with LES.

Another parameter to compute the LES resolution is the ratio of the SGS viscosity to the molecular viscosity, given by (DURBIN; PETTERSSON-REIF, 2015)

$$s' = \frac{\nu_{SGS}}{\nu_{SGS} + \nu} \tag{2.58}$$

Several authors (DAVIDSON, 2009; BEN-NARS et al., 2017) prefer to express the ratio of the SGS viscosity to the molecular viscosity as follows

$$s'' = \frac{\nu_{SGS}}{\nu} \tag{2.59}$$

Both parameters s' and s'' range between 0 and 1 and represents the degree of modeling in an LES simulation. According to (DURBIN; PETTERSSON-REIF, 2015), when the ratio of the SGS viscosity to molecular viscosity is not more than the order of 0.1, LES is found to be very accurate. When it reaches 1, the simulation is considered inaccurate.

An alternative measure of the resolution can be defined via the rate of energy dissipation (DURBIN; PETTERSSON-REIF, 2015; BEN-NARS et al., 2017), given by

$$\varepsilon' = \frac{\varepsilon_{SGS}}{\varepsilon_{SGS} + \varepsilon} \tag{2.60}$$

where ε_{SGS} is the SGS dissipation.

Davidson (2009) and Davidson (2011) presented and discussed some further methods to assess the LES resolution, including energy spectra, two-point correlations, and the ratio of SGS shear stress to resolved Reynolds shear stress $N_s = \tau_{SGS,12}/(u'v')$. The author argues that two-point correlations are the best measures for estimating LES resolution. From this property, it is possible to know the number of grids used to solve the largest scales of the flow.

Finally, Meyers et al. (2003) and Celik et al. (2005) formulated some indices to measure the resolution of an LES, including the contributions from both the SGS modeling and numerical discretization.

Chapter summary

This chapter provided some fundamental conceptualization about the subjects that will be covered in the development of this work. The basic concepts about non-Newtonian fluids behavior and a brief discussion regarding generalized Newtonian fluids were introduced. The characteristics of turbulent flows and the difference in the TKE budget between Newtonian and GNFs were also shown. Subsequently, the LES filtering process of the balance equations was presented, and the most used filters and their respective characteristics. Two SGS models derived from the eddy viscosity hypothesis (Dynamic Smagorinsky and WALE) to compute the effects of unresolved scales were also discussed. The chapter is concluded with a brief discussion regarding several methods available in the literature to assess the resolution of LES data.

3 NUMERICAL IMPLEMENTATION

This chapter presents the numerical methodology used, exposing the characteristics of the Open source Field Operation And Manipulation (OpenFOAM) code, which is based on the Finite Volume Method (FVM). Only the discretization and interpolation methods and the solution techniques for systems of linear algebraic equations employed in this work will be discussed. For the other approaches available in the OpenFOAM package, the reader is advised to consult the work of Jasak (1996), which is the primary source regarding OpenFOAM's FVM implementation.

The selection of OpenFOAM as the tool to perform the numerical simulations is based on some reasons. First, the OpenFOAM is an open-source Computational Fluid Dynamics (CFD) package under the GNU General Public License. The code also provides a collection of libraries for pre-processing, solving, and post-processing and a structure that can be used to develop specific applications, such as custom solvers and boundary conditions.

3.1 Introduction

The FVM is a numerical technique that transforms the set of partial differential equations representing conservation laws of fluid dynamics into a system of linear algebraic equations. The integral formulation of conservation laws is directly discretized in the physical space (HIRSC, 2007).

The discretization procedure used in the FVM demands two steps.The first step is to divide the computational domain into a finite number of discrete regions, called elements or cells, whose one element can represent a control volume. This approach is known as cell-centered, where control volumes coincide with elements. Another method to define a control volume is cell vertex, where the control volume is formed by a set of adjacent cells that share the same vertex (VERSTEEG; MALALASEKERA, 2007; MOUKALLED et al., 2016).

The cell-centered variable arrangement is currently the most popular variable arrangement used with the FVM (MOUKALLED et al., 2016). In this approach, the variables and their related quantities are stored at the centroids of the elements.

After the domain discretization, the partial differential equations are integrated over the control volumes. Then, to obtain an algebraic equation for each control volume, the surface and volume integrals are approximated using quadrature formulae (FERZIGER; PERIC, 2002; MOUKALLED et al., 2016).

3.2 Domain Discretization

The geometric domain is subdivided into a finite number of elements resulting in a mesh in which the balance equations are solved. The mesh is composed of discrete elements defined by a set of vertices and bounded by faces. These control volumes do not overlap and fill the computational domain completely.

A typical pair of the control volume is depicted in Figure 3.1. It is conventional to indicate the centroid of the control volume of interest as P, the face of the control volume as f, and the centroid of a neighboring control volume with a common face to P as N. The vector **d** is the distance between cell centroids, $\mathbf{d} = \mathbf{x}_P - \mathbf{x}_N$, and $\mathbf{S}_f$ is the face normal area vector. The $\mathbf{S}_f$ point outwards from the control volume and has a magnitude equal to the area of the face.

In the control volume, the definitions of centroid P and the centroid of the face f are given by

$$\int_{V_P} (\mathbf{x} - \mathbf{x}_p) dV = 0 \tag{3.1}$$

$$\int_f (\mathbf{x} - \mathbf{x}_f) d\mathbf{S} = 0 \tag{3.2}$$

where $\mathbf{x}_P$ is the position of the cell centroid, $\mathbf{x}_f$ is the face center, x is the position of a generic point within the domain, and $d\mathbf{S}$ ($d\mathbf{S} = \mathbf{n}dS$) represents an infinitesimal surface element with associated normal **n** pointing outward of the surface ∂V.

All the dependent variables (e.g. velocity, pressure, temperature) are stored at the cell centroid in the OpenFOAM code. The adoption of this arrangement is favorable for solving flows in complex geometries (MOUKALLED et al., 2016).

Figure 3.1 – A pair of control volumes.

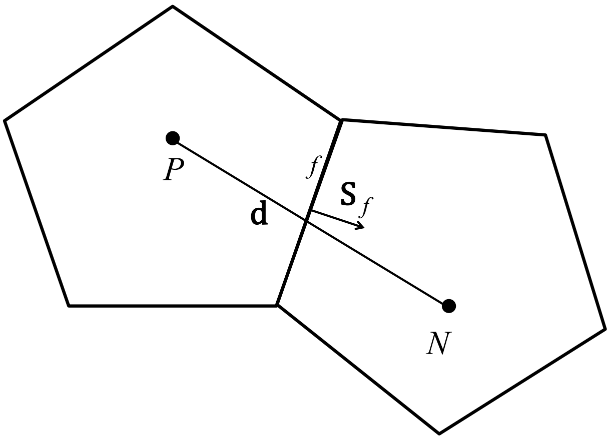

Source: Own Elaboration.

3.3 Discretization of the Transport Equations

The transport equation for a generic scalar property ϕ is defined as (VERSTEEG; MALALASEKERA, 2007; MOUKALLED et al., 2016)

$$\underbrace{\frac{\partial \phi}{\partial t}}_{\text{Transient term}} + \underbrace{\nabla \cdot (\mathbf{u}\phi)}_{\text{Advective term}} = \underbrace{\nabla \cdot (\Gamma \nabla \phi)}_{\text{Diffusion term}} + \underbrace{S_\phi(\phi)}_{\text{Source term}} \tag{3.3}$$

where Γ is the diffusivity coefficient and S_ϕ represents a source term. The discretization of each Eq. (3.3) terms will be discussed separately in the sequence.

The FVM requires the integration of Eq. (3.3) over a control volume (VERSTEEG; MALALASEKERA, 2007; MOUKALLED et al., 2016), yielding

$$\begin{aligned} \int_t^{t+\Delta t} \left[\frac{\partial}{\partial t} \int_{V_P} \phi dV + \int_{V_P} \nabla \cdot (\mathbf{u}\phi) dV - \int_{V_P} \nabla \cdot (\Gamma_\phi \nabla \phi) dV \right] dt \\ = \int_t^{t+\Delta t} \left[\int_{V_P} S_\phi(\phi) dV \right] dt \end{aligned} \tag{3.4}$$

where V_P is the control volume around the point P.

In order to obtain second-order accuracy, a linear variation of ϕ around the point P is assumed in both space and time as (JASAK, 1996; MOUKALLED et al., 2016)

$$\phi(\mathbf{x}) = \phi_p + (\mathbf{x} - \mathbf{x}_P) \cdot (\nabla_\phi)_P \tag{3.5}$$

$$\phi(t + \Delta t) = \phi^t + \Delta t \left(\frac{\partial \phi}{\partial t} \right)^t \tag{3.6}$$

where $\phi_P = \phi(\mathbf{x}_P)$ and $\phi^t = \phi(t)$.

According to the linear variation of $\phi(\mathbf{x})$, Eq. 3.5, the integral over the volume V_P becomes:

$$\begin{aligned} \int_{V_P} \phi(\mathbf{x}) dV = \int_{V_P} [\phi_p + (\mathbf{x} - \mathbf{x}_P) \cdot (\nabla_\phi)_P] dV \\ = \phi_P \int_{V_P} dV + \underbrace{\left[\int_{V_P} (\mathbf{x} - \mathbf{x}_P) dV \right]}_{=0\ (Eq. 3.1)} \cdot (\nabla_\phi)_P = \phi_P V_P \end{aligned} \tag{3.7}$$

Terms under the divergence operator are evaluated using the Gauss divergence theorem, according to

$$\begin{aligned} \int_{V_p} \nabla \cdot \mathbf{a} dV = \oint_{\partial V} d\mathbf{S} \cdot \mathbf{a} \\ = \sum_f \left(\int_f d\mathbf{S} \cdot \mathbf{a} \right) \end{aligned} \tag{3.8}$$

where **a** is a generic vector.

By assuming a linear variation of $\phi(\mathbf{x})$, the expression for the surface integral is defined as

$$\begin{aligned}\int_f d\mathbf{S}\cdot\mathbf{a} &= \left(\int_f d\mathbf{S}\right)\cdot\mathbf{a}_f + \underbrace{\left[\int_f (\mathbf{x}-\mathbf{x}_f)d\mathbf{S}\right]}_{=0(Eq.3.2)} : (\nabla\mathbf{a})_f \\ &= \mathbf{S}_f\cdot\mathbf{a}_f\end{aligned} \tag{3.9}$$

Combining Eqs. (3.8) and (3.9), one obtains

$$\int_{V_p} \nabla\cdot\mathbf{a}\,dV = \sum_f\left(\int_f d\mathbf{S}\cdot\mathbf{a}\right) = \sum_f \mathbf{S}_f\cdot\mathbf{a}_f \tag{3.10}$$

3.3.1 Advective Term

The discretization of the advective term is obtained using Eq. (3.10)

$$\int_{V_P} \nabla\cdot(\mathbf{u}\phi)dV = \sum_f \mathbf{S}_f\cdot(\mathbf{u}\phi)_f = \sum_f \mathbf{S}_f\cdot(\mathbf{u})_f\phi_f = \sum_f F_f\phi_f \tag{3.11}$$

where $F_f = \mathbf{S}_f\cdot\mathbf{u}_f$ is the mass flux through the face f and ϕ_f is the face value of the transported quantity ϕ.

The value of ϕ_f is not given directly, so it must be interpolated to the cell faces employing the so-called Convection Differencing Scheme – CDS (FERZIGER; PERIC, 2002).

The central differencing scheme performs a straightforward approximation for the value on the face between the two nearest nodes. This method interpolates linearly the face value of ϕ between the point P and a neighboring point N. The schematic representation is illustrated in Figure 3.2, and the equation for ϕ_f is expressed as (FERZIGER; PERIC, 2002)

$$\phi_f = f_x\phi_P + (1-f_x)\phi_N \tag{3.12}$$

where f_x is the interpolation factor, and it is defined as the ratio of the distances fN and PN as

$$f_x = \frac{fN}{PN} \tag{3.13}$$

It is worth mentioning that the central differencing scheme can produce non-physical oscillations in the solution for advection-dominated problems (FERZIGER; PERIC, 2002; HIRSC, 2007). Nonetheless, this issue can be remedied with mesh refinement (DE VILLIERS, 2006; VERSTEEG; MALALASEKERA, 2007; XU; YANG, 2021).

Several authors used the central differencing scheme in conjunction with the FVM (LAMPITELLA, 2014; KOMEN et al., 2014; KOMEN et al., 2017; ZHENG et al., 2019) to reproduce turbulent flows with LES and DNS. Adedoyin et al. (2015) investigated the combination of several CDS and SGS models. The author mentions that the central differencing scheme presents better results than the other methods.

Figure 3.2 – Face interpolation to calculate the face fluxes between the two nearest nodes.

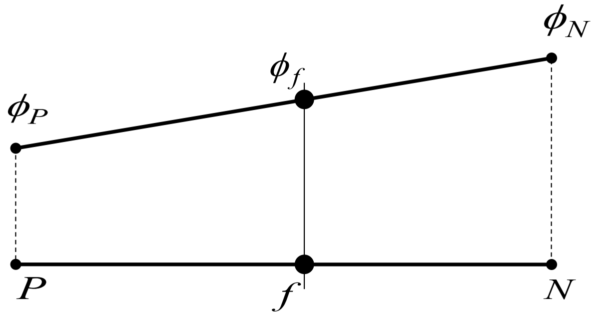

Source: Adapted from OpenFOAM.

3.3.2 Diffusive Term

A similar approach employed in discretizing the advective term is used here. The linear variation of the quantity ϕ is also assumed to compute the diffusion term of the Eq. (3.4)

$$\int_{V_P} \nabla \cdot (\Gamma_\phi \nabla_\phi) dV = \sum_f \mathbf{S}_f \cdot (\Gamma_\phi \nabla_\phi)_f = \sum_f (\Gamma_\phi)_f \, \mathbf{S}_f \cdot (\nabla \phi)_f \tag{3.14}$$

In the case of an orthogonal mesh, the vectors $\mathbf{d}$ and $\mathbf{S}_f$ depicted in Figure 3.3 are parallel. Then, the following expression is used to estimate the face gradient of ϕ:

$$\mathbf{S}_f \cdot (\nabla_\phi)_f = |\mathbf{S}_f| \frac{\phi_N - \phi_P}{|\mathbf{d}|} \tag{3.15}$$

Figure 3.3 – Schematic representation of vector decomposition for an orthogonal mesh.

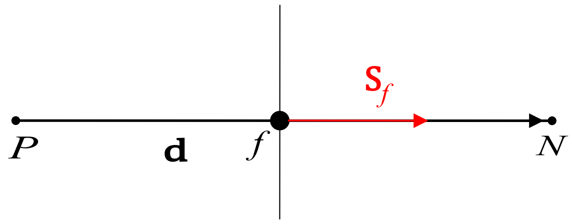

Source: Adapted from OpenFOAM.

For non-orthogonal cells, the product $\mathbf{S}_f \cdot (\nabla_\phi)_f$ is divided into two parts, according to Figure 3.4.

$$\mathbf{S}_f \cdot (\nabla \phi)_f = \underbrace{\Delta \cdot (\nabla \phi)_f}_{orthogonal\ contribution} + \underbrace{\varpi \cdot (\nabla \phi)_f}_{non-orthogonal\ contribution} \tag{3.16}$$

The first term on the right side of Eq. (3.16) is an orthogonal contribution since the Δ vector has the same direction of $\mathbf{d}$, while the second term is a non-orthogonal correction since the Δ and ϖ vectors add up to the vector $\mathbf{S}_f$.

Figure 3.4 – Schematic representation of vector decomposition for a non-orthogonal mesh.

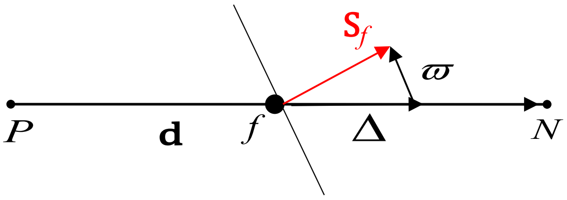

Source: Adapted from OpenFOAM.

$$\mathbf{S}_f = \Delta + \boldsymbol{\varpi} \tag{3.17}$$

Eq. (3.16) can be rewritten using Eq. (3.15) for the orthogonal contribution and a correction equation for the non-orthogonal term as

$$\mathbf{S}_f \cdot (\nabla_\phi)_f = |\Delta| \frac{\phi_N - \phi_P}{|\mathbf{d}|} + \boldsymbol{\varpi} \cdot [f_x (\nabla \phi)_P + (1 - f_x)(\nabla \phi)_N] \tag{3.18}$$

where

$$(\nabla \phi)_P = \frac{1}{V_p} \sum_f \mathbf{S}_f \phi_f \tag{3.19}$$

3.3.3 Source Term

The source term usually represents a general function of ϕ that cannot be considered either in the advective and diffusive terms or in the temporal contribution of the transport equation (JASAK, 1996). This term is linearized as follows

$$S_\phi(\phi) = S_C + S_P \phi \tag{3.20}$$

where S_c and S_P can also depend on ϕ. Following Eq. (3.7), the volume integral is calculated as

$$\int_{V_P} S_\phi(\phi) dV = S_C V_P + S_P V_P \phi_P \tag{3.21}$$

Finally, the integral form of the transport equation introduced in Eq. (3.4) is here again reported.

$$\begin{aligned} \int_t^{t+\Delta t} \left[\frac{\partial}{\partial t} \int_{V_P} \phi dV + \int_{V_P} \nabla \cdot (\mathbf{u}\phi) dV - \int_{V_P} \nabla \cdot (\Gamma_\phi \nabla \phi) dV \right] dt \\ = \int_t^{t+\Delta t} \left[\int_{V_P} S_\phi(\phi) dV \right] dt \end{aligned} \tag{3.22}$$

Substituting the discretized terms, Eq.(3.11), (3.14), and (3.21), into Eq. (3.22), one obtains the semi-discretized form of the transport equation (HIRSC, 2007; MOUKALLED et al., 2016)

$$\begin{aligned}\int_t^{t+\Delta t}\left[\left(\frac{\partial\phi}{\partial t}\right)_P V_P + \sum_f F_f\phi_f - \sum_f(\Gamma_\phi)_f\,\mathbf{S}_f\cdot(\nabla\phi)_f\right]dt \\ = \int_t^{t+\Delta t}\left[S_C V_P + S_P V_P\phi_P\right]dt\end{aligned} \tag{3.23}$$

3.3.4 Temporal Discretization

The temporal term is discretized using a second-order implicit backward differencing scheme. This method requires the expansion of ϕ^n values at ϕ^{n-1} and ϕ^{n-2}. In order to calculate the temporal derivative, the time level $n-2$ is expressed as a Taylor expansion around n:

$$\phi^{n-2} = \phi^n - 2\left(\frac{\partial\phi}{\partial t}\right)^n\Delta t + 2\left(\frac{\partial^2\phi}{\partial t^2}\right)^n\Delta t^2 + O(\Delta t^3) \tag{3.24}$$

Likewise, for the term $\phi n-1$ around n

$$\phi^{n-1} = \phi^n - \left(\frac{\partial\phi}{\partial t}\right)^n\Delta t + \frac{1}{2}\left(\frac{\partial^2\phi}{\partial t^2}\right)^n\Delta t^2 + O(\Delta t^3) \tag{3.25}$$

Combining Eqs. (3.24) and (3.25), the second-order approximation of the temporal derivative is (JASAK, 1996):

$$\left(\frac{\partial\phi}{\partial t}\right)^n = \frac{\frac{3}{2}\phi^n - 2\phi^{n-1} + \frac{1}{2}\phi^{n-2}}{\Delta t} \tag{3.26}$$

By assuming that the density, the advective and the diffusive fluxes do not change in time within each time step, the final form of the discretized transport equation becomes (JASAK, 1996; KOMEN et al., 2014):

$$\begin{aligned}\frac{\frac{3}{2}\phi^n - 2\phi^{n-1} + \frac{1}{2}\phi^{n-2}}{\Delta t}V_P + \sum_f F_f\phi_f^n - \sum_f(\Gamma_\phi)_f\,\mathbf{S}_f\cdot(\nabla\phi)_f^n \\ = \left[S_C V_P + S_P V_P\phi_P^n\right]\end{aligned} \tag{3.27}$$

The convergence and stability of numerical schemes are reached by Courant–Friedrichs–Lewy *(CFL)* condition (MOUKALLED et al., 2016) as follows

$$CFL = \frac{u_i\Delta t}{\Delta_x} + \frac{u_j\Delta t}{\Delta_y} + \frac{u_k\Delta t}{\Delta_z} \tag{3.28}$$

The *CFL* must be smaller than 1 to ensure numerical stability (HIRSC, 2007; MOUKALLED et al., 2016). Consequently, the small time step helps to correctly capture the fluctuations or transient characteristics of turbulent flows.

3.4 Boundary Conditions

Boundary conditions play an important role in numerical simulations of fluid flow. For instance, the flow fields within a domain are quite different for distinct boundary conditions, although the governing equations representing a particular phenomenon are the same. The class of boundary conditions used in this work is given by Dirichlet, Neumann, and periodic boundary conditions.

3.4.1 Dirichlet Boundary Condition

This approach prescribes a fixed value of ϕ at the boundary face b, yielding $\phi = \phi_b$ A schematic view is illustrated in Figure 3.5. This boundary condition is used to prescribe the velocity field at the inlet domain and define the no-slip condition at the walls. The equations for the Dirichlet boundary condition when applied to the advective and diffusive terms are defined below.

- **Advective term**: From Eq. (3.11), the advective term is discretized as

$$\int_{V_P} \nabla \cdot (\mathbf{u}\phi) dV = \sum_f F_f \phi_f \tag{3.29}$$

The boundary flux is evaluated directly by employing the fixed value of ϕ_b. Therefore

$$(F_f \phi_f)_{f \to b} = F_b \phi_b \tag{3.30}$$

- **Diffusive term:** The diffusive term is discretized according to Eq.(3.14)

$$\int_{V_P} \nabla \cdot (\Gamma_\phi \nabla_\phi) dV = \sum_f (\Gamma_\phi)_f \, \mathbf{S}_f \cdot (\nabla\phi)_f \tag{3.31}$$

The face gradient at face b is calculated from the known face value ϕ_b and thecell center value ϕ_P, similar to Eq. (3.15):

$$\mathbf{S}_f \cdot (\nabla_\phi)_b = |\mathbf{S}_b| \frac{\phi_b - \phi_P}{|\mathbf{d}_b|} \tag{3.32}$$

3.4.2 Neumann Boundary Conditions

This type of boundary condition specifies the normal gradient $\mathbf{g}_b$ at the boundary face, it is computed as follows

$$\frac{\partial \phi}{\partial \mathrm{n}_b} = \frac{\mathbf{S}_b}{|\mathbf{S}_b|} = \mathbf{g}_b \tag{3.33}$$

The Neumann boundary condition is depicted in Figure 3.6, and for the current work, it is applied to the wall region for the pressure field.

Figure 3.5 – Schematic representation of the Dirichlet boundary condition.

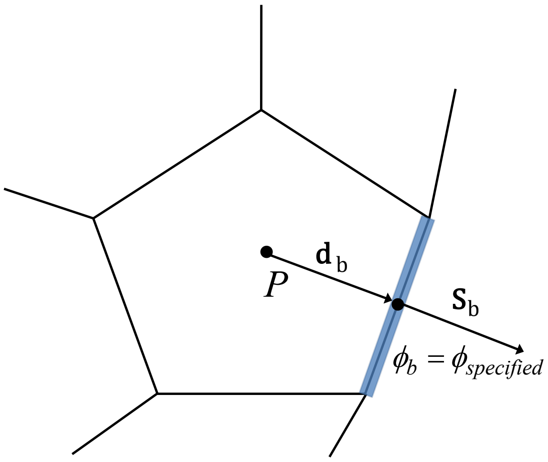

Source: Adapted from Moukalled et al. (2016).

- **Advective term**: Since the value of ϕ_b is not provided, the face value ϕ_b is calculated from the value in the cell center ϕ_P Moreover, the prescribed gradient at the boundary

$$\begin{aligned}\phi_b &= \phi_P + \mathbf{d}_b \cdot (\nabla\phi)_b \\ &= \phi_P + |\mathbf{d}_b| \cdot \mathbf{g}_b\end{aligned} \tag{3.34}$$

- **Diffusive term**: In this case, the fixing of the boundary condition is direct, since

$$(\nabla\phi)_b \cdot \mathbf{S}_b = \mathbf{g}_b \tag{3.35}$$

Figure 3.6 – Schematic representation of the Neumann boundary condition.

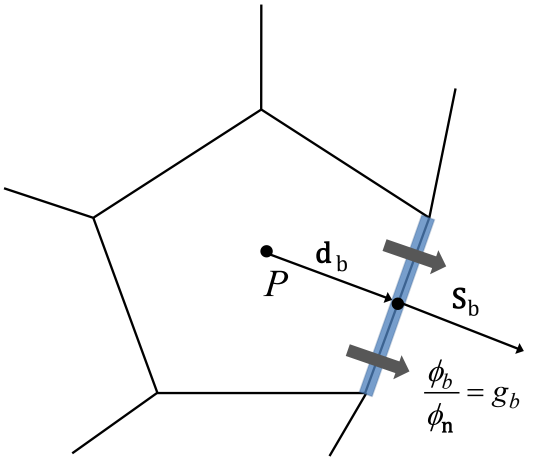

Source: Adapted from Moukalled et al. (2016).

3.4.3 Periodic Boundary Conditions

Periodic boundary conditions help approximate a large (infinite) domain, e.g., channel and pipe flow, when the flow is statistically homogeneous in a particular direction, or the geometry is periodic in one or two directions (RODI et al., 2013). For any flow variable, such as velocity field, the periodic boundary condition implies

$$\mathbf{u}(\mathbf{x},t) = \mathbf{u}(\mathbf{x}+\mathbf{L}',t) \tag{3.36}$$

where $\mathbf{L}'$ is the length of the periodic region.

3.5 Discretization ofthe Navier-Stokes Equation

The discretization methods presented above for a generic scalar property ϕ provide the basis for the discretization of the Navier-Stokes equations. By integrating the Eqs. (2.37) and (2.40) over a control volume to yield the integral form of the governing equations, one obtains

$$\int_{V_P} \nabla \cdot \tilde{\mathbf{u}} dV = \int_{\partial V} dS \cdot \tilde{\mathbf{u}} = 0 \tag{3.37}$$

$$\begin{split}\int_t^{t+\Delta t} \left[\frac{d}{dt}\int_{V_P} \widetilde{\mathbf{u}} dV + \int_{V_P} \nabla \cdot (\widetilde{\mathbf{u}} \otimes \widetilde{\mathbf{u}}) dV - \int_{V_P} \nabla \cdot [\nu_{eff}(\nabla \widetilde{\mathbf{u}} + (\nabla \widetilde{\mathbf{u}})^T)] dV \right] dt = \\ -\int_t^{t+\Delta t} \left[\frac{1}{\rho} \int_{V_P} \nabla \widetilde{P} dV \right] dt\end{split} \tag{3.38}$$

where ν_{eff} is the sum of the kinematic viscosity ν and SGS viscosity ν_{SGS}.

Two issues require special attention: the non-linearity of the momentum equation and the pressure-velocity coupling. First, the advective term $\nabla \cdot (\widetilde{\mathbf{u}} \otimes \widetilde{\mathbf{u}})$ appearing in Eq. (3.38) results in a quadratic function and must be linearized to prevent the resulting system of algebraic equations from being nonlinear. This procedure is achieved by replacing one of the values from the current iteration of velocity with a value from the previous time-step ($\widetilde{\mathbf{u}}^0 \approx \widetilde{\mathbf{u}}$). The advective term is linearized as follows (JASAK, 1996; DAMIÁN, 2013):

$$\begin{aligned}\int_{V_P} \nabla \cdot (\widetilde{\mathbf{u}} \otimes \widetilde{\mathbf{u}}) dV &= \sum_f \mathbf{S}_f \cdot \widetilde{\mathbf{u}}_f \cdot \widetilde{\mathbf{u}}_f \\ &\approx \sum_f (\mathbf{S}_f \cdot \widetilde{\mathbf{u}}_f^0) \cdot \widetilde{\mathbf{u}}_f = \sum_f F_f^0 \cdot \widetilde{\mathbf{u}}_f \\ &= a_P \widetilde{\mathbf{u}}_P + \sum_f a_N \widetilde{\mathbf{u}}_N\end{aligned} \tag{3.39}$$

where F_f^0 is the mass flux through the face f at the previous time-step, $\widetilde{\mathbf{u}}_f^0$ is the velocity at the previous time-step, a_P are the diagonal coefficients of the discretization matrix, and a_N the off-diagonal ones.

The coefficients a_P and a_N are functions of $\widetilde{\mathbf{u}}^0$. The flux conservation at each time-step is taken from the iteration of the pressure-velocity loop, which assures the application of the continuity equation (DE VILLIERS, 2006; DAMIÁN, 2013). In addiction, since the time-step is small (CFL<1), the variation between consecutive solutions will also be small, and it is possible to delay the non-linearity without any significant effect (JASAK, 1996).

Regarding the pressure-velocity coupling, the question that arises when using segregated schemes, as in the OpenFOAM code, with incompressible fluids is how to solve the pressure field from the conservation equation, where the pressure does not show up, but only the velocity. Therefore, it is necessary to derive a pressure equation for the incompressible Navier-Stokes system.

3.5.1 Solution of the Pressure Equation

Starting from the semi-discretized form of the momentum equation is possible to derive an equation for the pressure field. The semi-discretized form of the momentum equation is defined as (JASAK, 1996)

$$a_P \widetilde{\mathbf{u}}_P = \mathbf{H}(\widetilde{\mathbf{u}}) - \nabla P \tag{3.40}$$

where $\mathbf{H}(\widetilde{\mathbf{u}})$ accounts for the advective and diffusive terms as well as all the source terms (JASAK, 1996; DAMIÁN, 2013)

$$\mathbf{H}(\widetilde{\mathbf{u}}) = -\sum_f a_N \widetilde{\mathbf{u}}_N + \frac{\widetilde{\mathbf{u}}^0}{\Delta t} \tag{3.41}$$

The discretized form of the continuity equation (Eq. 2.37) can be written as

$$\nabla \cdot \tilde{\mathbf{u}} = \sum_f \mathbf{S}_f \cdot \widetilde{\mathbf{u}}_f = 0 \tag{3.42}$$

The Eq.(3.40) is used to express the velocity at the cell center $\widetilde{\mathbf{u}}_P$

$$\widetilde{\mathbf{u}}_P = \frac{\mathbf{H}(\widetilde{\mathbf{u}})}{a_P} - \frac{1}{a_P}\nabla \widetilde{P} \tag{3.43}$$

Interpolating the Eq. (3.43) to express the velocities at cell faces $\widetilde{\mathbf{u}}_f$

$$\widetilde{\mathbf{u}}_f = \left(\frac{\mathbf{H}(\widetilde{\mathbf{u}})}{a_P}\right)_f - \left(\frac{1}{a_P}\right)_f \left(\nabla \widetilde{P}\right)_f \tag{3.44}$$

This equation will serve as a basis for the calculation of face fluxes. Introducing the above equation into Eq. (3.42), an equation for the pressure can be obtained:

$$\nabla \cdot \left(\frac{1}{a_P}\nabla \widetilde{P}\right) = \nabla \cdot \left(\frac{\mathbf{H}(\widetilde{\mathbf{u}})}{a_P}\right) \tag{3.45}$$

Then, the set of discrete equations for the Navier-Stokes system is defined as

$$a_P \widetilde{\mathbf{u}}_P = \mathbf{H}(\widetilde{\mathbf{u}}) - \sum_f S(\widetilde{P})_f \tag{3.46}$$

$$\sum_f S_f \cdot \left[\left(\frac{1}{a_P} \right)_f (\nabla \widetilde{P})_f \right] = \sum_f \mathbf{S}_f \cdot \left(\frac{\mathbf{H}(\widetilde{\mathbf{u}})}{a_P} \right)_f \tag{3.47}$$

where $S(\widetilde{P})$ is a source term given by the pressure gradient. Finally, the face flux F is estimated using Eq. (3.44)

$$F = \widetilde{\mathbf{u}}_f \cdot \mathbf{S}_f = \left[\left(\frac{\mathbf{H}(\widetilde{\mathbf{u}})}{a_P} \right)_f - \left(\frac{1}{a_P} \right)_f \left(\nabla \widetilde{P} \right)_f \right] \cdot \mathbf{S}_f \tag{3.48}$$

3.5.2 The PISO Algorithm for Pressure-Velocity Coupling

By considering the final form of the Navier-Stokes system, Eqs. (3.46) and (3.47), a solution for the pressure-velocity coupling can be developed. The Pressure-Implicit-Split-Operator (PISO) algorithm has been initially proposed by Issa (1986). In this approach, the method performs a series of corrections to velocity and pressure fields until the convergence of the solution is reached. The PISO algorithm can be described as follows:

1. An approximation for the velocity field is estimated by solving the momentum equation (Eq. 3.46) using the pressure field of the previous time-step. This step is called *momentum predictor.*

$$a_P \widetilde{\mathbf{u}}_P = \mathbf{H}(\widetilde{\mathbf{u}}) - \sum_f S(\widetilde{P}^0)_f \tag{3.49}$$

2. Using velocity field obtained, the $\mathbf{H}(\widetilde{\mathbf{u}})$ operator can be assembled, and the pressure equation (Eq. 3.47) is solved. The solution of the pressure equation gives the first estimate of the new pressure field. This step is called the *pressure solution.*

$$\sum_f S_f \cdot \left[\left(\frac{1}{a_P} \right)_f (\nabla \widetilde{P})_f \right] = \sum_f \mathbf{S}_f \cdot \left(\frac{\mathbf{H}(\widetilde{\mathbf{u}})}{a_P} \right)_f \tag{3.50}$$

3. Eq. (3.48) gives a set of conservative fluxes consistent with the new pressure field.

$$F = \widetilde{\mathbf{u}}_f \cdot \mathbf{S}_f = \left[\left(\frac{\mathbf{H}(\widetilde{\mathbf{u}})}{a_P} \right)_f - \left(\frac{1}{a_P} \right)_f \left(\nabla \widetilde{P} \right)_f \right] \cdot \mathbf{S}_f \tag{3.51}$$

4. The correction of the velocity field at the cell center is carried out due to the new pressure distribution. The velocity correction is done in an explicit manner using Eq. (3.43). This passage is called the *explicit velocity correction.*

$$\widetilde{\mathbf{u}}_P = \frac{\mathbf{H}(\widetilde{\mathbf{u}})}{a_P} - \frac{1}{a_P} \nabla \widetilde{P} \tag{3.52}$$

5. If the convergence of pressure and velocity fields is reached, the solution advances. Otherwise, steps 2 to 4 are repeated until convergence is achieved.

Figure 3.7 summarises the solution flowchart of the numerical code.

Figure 3.7 – Solution flowchart.

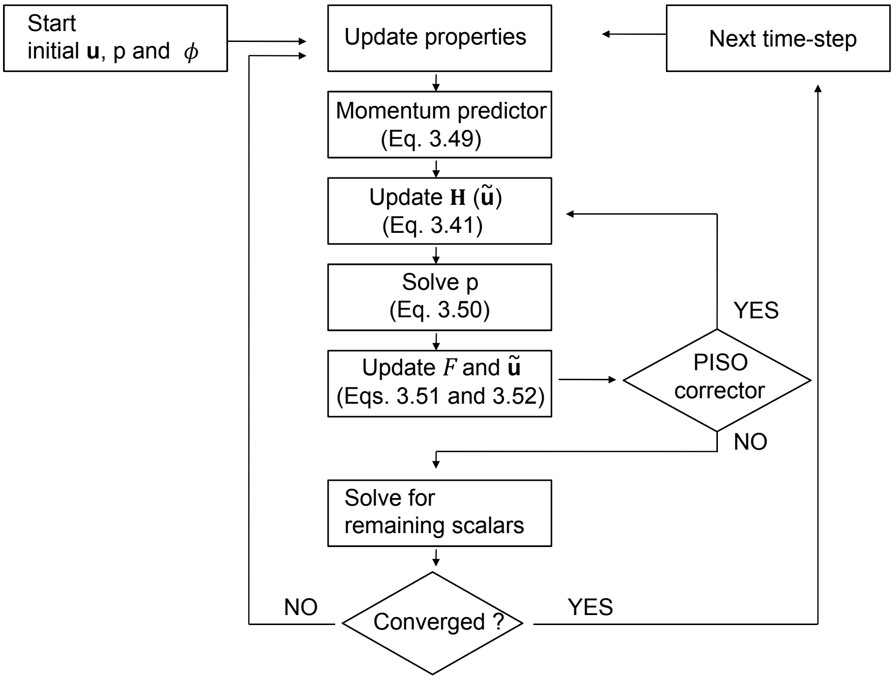

Source: Own elaboration.

3.6 Solving the System of Algebric Equations

The final form of the discretization process is a system of linear equations for each control volume that can be written as follows (FERZIGER; PERIC, 2002; MOUKALLED et al., 2016)

$$\mathbf{A}_\phi \boldsymbol{\phi} = \mathbf{R} \tag{3.53}$$

where $\mathbf{A}_\phi$ is the matrix of a_P and a_N coefficients, $\boldsymbol{\phi}$ is a vector of unknowns located at the centroids of the elements, and $\mathbf{R}$ is the vector that contains all sources, constants, boundary conditions, and non-linearizable components (MOUKALLED et al., 2016). The solution of this system is usually obtained by the use of iterative linear equations solvers.

The discretization of the balance equation generally produces asymmetrical linear systems due to the advective term. Conversely, the matrix of coefficients resulting from the discretization of the incompressible pressure equation or pressure correction equation yields symmetrical systems (MOUKALLED et al., 2016).

In the present thesis, the system of linear equations is resolved by employing different solvers. The preconditioned Bi-Conjugate Gradient solver (PBiCG) with Diagonal Incomplete LU (DILU) as a preconditioner is used for asymmetric matrices. According to (BENZI, 2002), the preconditioners attempt to improve the properties of the coefficient matrix and thus optimize the solver's performance. The Geometric-Algebraic Multi-Grid (GAMG) solved the pressure equation with Gauss-Seidel as smoother for symmetric matrices. Finally, regarding the convergence of the solvers, the iterative calculation is performed until the residual value computed by the L1 norm reaches orders of magnitude set by the user.

Chapter Summary

This chapter introduced the finite volume discretization technique adopted in the OpenFOAM code. The second-order discretization schemes applied in this work are described in Section 3.3. The boundary conditions, the discretization procedure for the Navier-Stokes equations, and the approach adopted for the pressure-velocity coupling based on the PISO algorithm were discussed in Sections 3.4 and 3.5. Finally, the methods to solve the linear systems are reported in Section 3.6. In the next chapter, the verification studies will be presented.

4 NUMERICAL VERIFICATION

In this chapter, the numerical methodology is tested. First, LES of turbulent pipe flows of Newtonian and Herschel-Bulkley fluids are investigated. Next, simulations of the turbulent flows of Newtonian fluids in a concentric annular section with inner cylinder rotation are performed. For the results obtained with the Newtonian fluids, only the first and second-order turbulence statistics are discussed, while those computed with the Herschel-Bulkley fluids, besides the turbulence statistics, flow quantities, including mean wall shear stress, mean wall viscosity, friction factor, mean shear rate and mean viscosity profiles are also compared to the reference data.

4.1 Turbulent Pipe Flow

Numerical simulations of turbulent pipe flows were carried out at two different generalized Reynolds numbers of $5,000$ and $7,500$. The pipe length in the axial direction is defined as $L_z = 4\pi D$. The pipe length follows the arguments of Singh et al. (2017a), which is based on a domain independence study via two-point correlation, and it has the same length used by Rudman et al. (2004), Singh et al. (2017b), and Zheng et al. (2019) for similar Reynolds numbers.

4.1.1 Initial and Boundary Conditions

The simulations with Herschel-Bulkley fluids were initialized with a fully developed Newtonian flow field. DE VILLIERS (2006) developed the approach to create an initial field for the Newtonian case. The method is based on the interaction between streaks and streamwise vortices that play a central role in near-wall turbulence production (CASSINELLI et al., 2017).

According to DE VILLIERS (2006), the profile is derived from the fully developed laminar flow. Near-wall parallel streaks are produced by modifying the base parabolic flow, U_{z0}^+, in the following way (DE VILLIERS, 2006)

$$\begin{aligned} U_z^+ = U_{z0}^+ + (\Delta u_{z0}^+/2)\ cos(b^+\theta^+ r^+)(y^+/30)\exp(-C_\sigma y^{+2} + 0.5), \\ U_r^+ = U_\theta^+ = 0 \end{aligned} \tag{4.1}$$

where U_z^+, are the mean velocity profiles in the axial, radial and azimuthal directions, respectively, Δu_{z0}^+ is the wall-normal circulation, b^+ stands for spanwise wavenumber and C_σ is the transverse decay, $C_\sigma = 0.00055$.

Then, these streaks need to be slightly perturbed to develop a wavy character which, in turn, will produce streamwise vortices. This is achieved by a second relation (Eq. 4.2), which introduces a spanwise perturbation (DE VILLIERS, 2006)

$$\begin{aligned} u_\theta = c_\epsilon \sin(a^+ z^+) y^+ \exp(-C_\theta y^{+2}), \\ u_z = u_r = 0 \end{aligned} \tag{4.2}$$

where c_ϵ is the linear perturbation amplitude, $c_\epsilon = u_b/200$, and a^+ is the axial wave numbers. The constants, b^+ and a^+ are chosen to produce a sparse streak spacing ($\theta^+ \approx 200$), equivalent to the buffer layer in the wall-normal extent ($y^+ = 30$) and with a maximum intensity of about 10% of the bulk fluid velocity (DE VILLIERS, 2006).

The standard no-slip boundary condition was applied at the pipe wall, and the flow is assumed periodic in the axial direction for any flow quantity $\phi(z, r, \theta) = \phi(z + L_z, r, \theta)$. In addition, the flow is driven by a constant mass flow rate.

It is worth mentioning that the apparent viscosity of the Herschel-Bulkley model diverges to infinity as the shear rate approaches zero (Eq. 2.7) and, therefore, a 'cut-off' value is used to remedy this issue. In the present work, the 'cut-off' value chosen is 0,01 [s^{-1}], and the values below are assumed to be constant for computing the viscosity.

4.1.2 Averaging Procedure

Before collecting averages over time, typically, 10 flow-through time ($FTT = L/U_b$) are required for the flow to reach a statistically steady state. After that, statistics were collected for 40 FTT. As the final step, the spatial averaging was carried out over the homogeneous directions during the post-processing.

4.1.3 Mesh Convergence Study

The mesh analysis is performed at two different Reynolds numbers. First, LES of turbulent pipe flow of a Newtonian fluid was considered to evaluate the mesh resolution for the simulations at $Re_G = 5,000$. The second case of LES of turbulent pipe flow of a Herschel-Bulkley fluid was used to check the grid for the simulations at $Re_G = 7,500$. The range of values mentioned in Section 2.6 provides a perception of the mesh requirements for LES analysis with a high-resolution grid. Four different grid resolutions were considered for both Reynolds numbers, as shown in Tables 4.1 and 4.2.

Table 4.1 – Summary of the computational grids for the turbulent pipe flow simulations with Newtonian fluid at $Re_G = 5,000$.

Mesh resolution	I	II	III	IV
N_z x N_r x N_θ	54x36x112	108x18x112	108x36x112	162x36x112
Number of cells	260,064	302,400	521,000	732,032
Δz^+	76	40	40	26.4
$(R\Delta\theta)^+$	9.5	9.4	9.2	9.2
Δr^+_{wall} (first volume near the wall)	0.41	0.84	0.4	0.4
Number of cells in the viscous sublayer	9	5	9	9
Number of cells for $y^+ \leq 10$	14	8	14	14

Source: Own elaboration.

Figure 4.1 depicts the profiles of the mean velocity and root-mean-square (RMS) velocity fluctuations calculated from the different SGS models for the simulations with the Newtonian fluid at $Re_G = 5,000$. The profiles are normalized using the friction velocity $u_\tau = \sqrt{\tau_w/\rho}$. Figure 4.2 illustrates the configuration of the meshes employed in the pipe cross-section.

Table 4.2 – Summary of the computational grids for the turbulent pipe flow simulations with Herschel-Bulkley fluid at $Re_G = 7,500$.

Mesh resolution	V	VI	VII	VIII
N_z x N_r x N_θ	54x42x136	108x21x136	108x42x136	162x42x136
Number of cells	370,872	433,296	741,744	1,126,616
Δz^+	98	52	52	34.2
$(R\Delta\theta)^+$	12.4	12.1	12.1	10.2
Δr^+_{wall} (first volume near the wall)	0.51	0.53	0.51	0.48
Number of cells in the viscous sublayer	7	4	7	7
Number of cells for $y^+ \leq 10$	12	7	12	12

Source: Own elaboration.

Results for the mean axial velocity and radial and azimuthal turbulence intensities obtained with the Dynamic Smagorinsky and WALE models on meshes II, III, and IV align with the reference DNS data. The major difference ($\approx 4\%$) between the meshes III and IV occurs in the range $50 < y^+ < 100$ for the RMS velocity fluctuations in the axial direction.

Figure 4.1 indicates that the difference in the outcomes between meshes III and IV are minimal and, thus, mesh III is considered adequate for the sequence of simulations at $Re_G = 5,000$ in the current work. Moreover, mesh III complies with the high-resolution grid requirements ($\Delta z^+ < 50$ and $R\Delta\theta^+ < 12$).

The profiles of mean velocity and RMS velocity fluctuations for the Herschel-Bulkley fluid at $Re_G = 7,500$ with different grid resolutions are illustrated in Figure 4.3. The non-Newtonian law of the wall for the mean axial velocity for Power-law and Herschel-Bulkley fluids proposed by Anbarlooei et al. (2015) are also plotted for comparison. The model parameters for the Herschel-Bulkley fluid are provided in Table 4.3. The bulk velocity is 1.0 [$\mathrm{m\ s^{-1}}$] and the pipe diameter is 0.1 [m].

Table 4.3 – Herschel-Bulkley fluid model parameters for the turbulent pipe flow simulations at $Re_G = 7,500$.

τ_y (Pa)	K (Pa s^n)	ρ (kg m^{-3})	n
4.28e-02	9.09e-02	1,000	0.65

Source: Zheng et al. (2019).

Results from meshes VI, VII and VIII computed by the Dynamic Smagorinsky and WALE models match with DNS data of Zheng et al. (2019) for radial and azimuthal turbulence intensities. In terms of the mean velocity and RMS turbulent intensity in the axial direction, just on mesh VIII the SGS models perform similarly with DNS data.

Overall, similar trends were observed between meshes VI, VII and VIII with the Dynamic Smagorinsky and WALE models. However, only the mesh VIII follows the guidelines of a high-resolution grid ($\Delta z^+ < 50$ and $R\Delta\theta^+ < 12$). Thus, the mesh IV will be considered for simulations at $Re_G = 7,500$.

Figure 4.1 – Profiles of mean velocity and turbulence intensities for the different SGS models. Turbulent pipe flow of a Newtonian fluid at $Re_G = 5,000$, (a) Dynamic Smagorinsky (b) WALE.

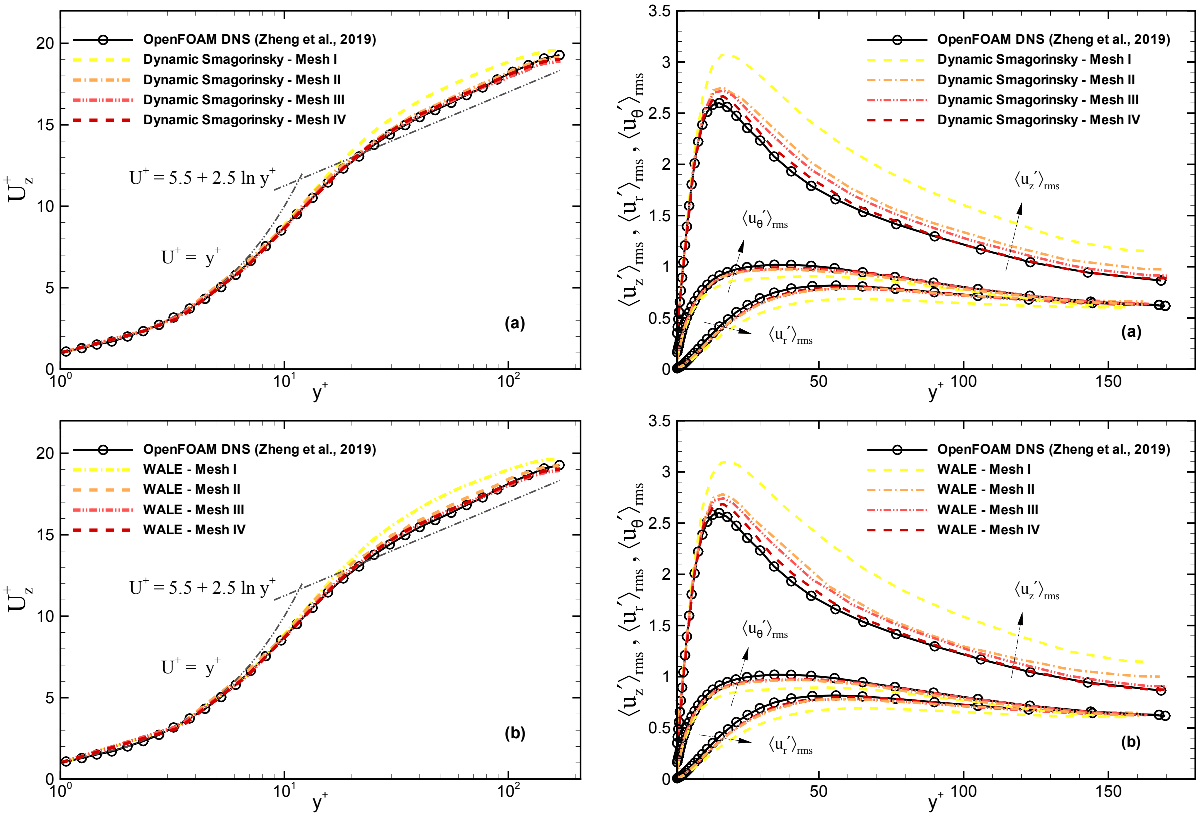

Source: Own elaboration.

Figure 4.2 – Pipe cross-section configuration on meshes I, III, and IV.

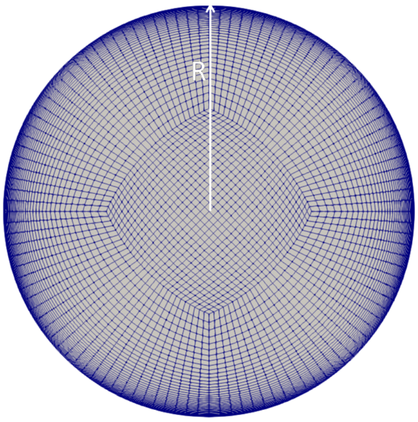

Source: Own elaboration.

4.1.4 Newtonian Fluid

In order to assess the predictive capability of the numerical method, the LES and UDNS computations are compared with the DNS results from Zheng et al. (2019) and experimental data from Den Toonder and Niewstadt (1997) for turbulent pipe flow of a Newtonian fluid at $Re_G = 5,000$.

Figure 4.3 – Profiles of mean velocity and turbulence intensities for the different SGS models. Turbulent pipe flow of a Herschel-Bulkley fluid at $Re_G = 7,500$, (a) Dynamic Smagorinsky (b) WALE.

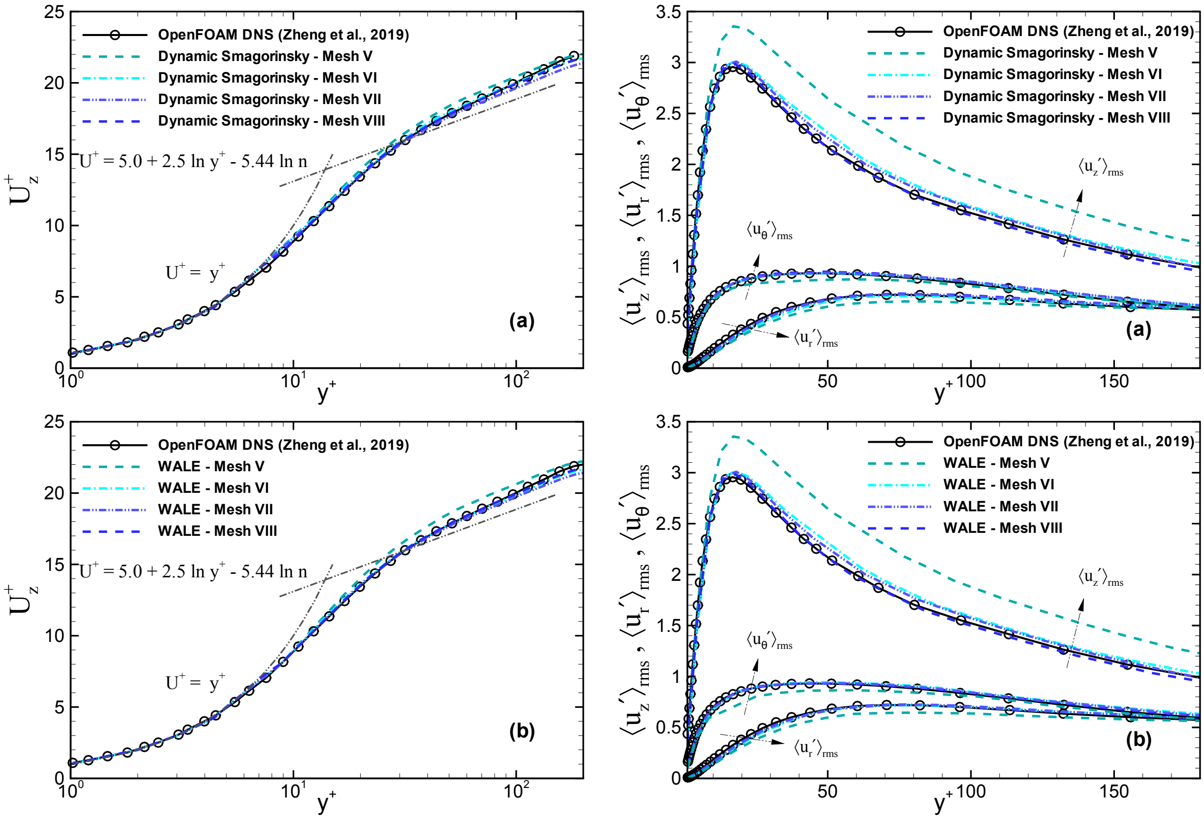

Source: Own elaboration.

Figure 4.4 shows the mean axial velocity profiles predicted by SGS models, UDNS, the corresponding DNS results (ZHENG et al., 2019), and the experimental data (Den Toonder; NIEWSTADT, 1997). The profiles are normalized using the friction velocity u_τ. The distributions of the mean axial velocity of both SGS models and UDNS are qualitatively consistent with the DNS results and experimental data.

Figure 4.4 – Mean axial velocity profiles of Newtonian fluid plotted in wall units for $Re_G = 5,000$.

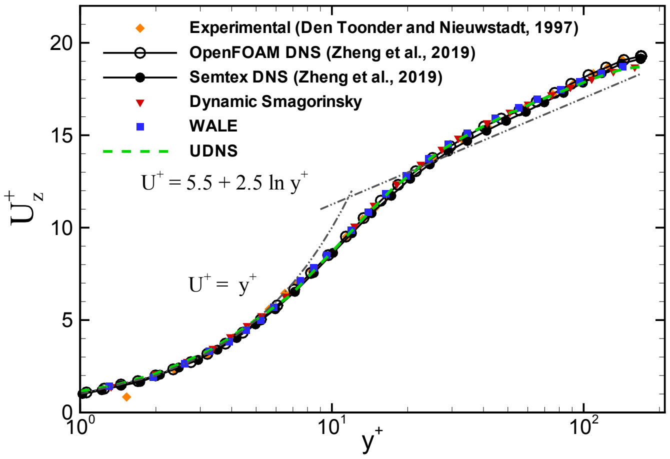

Source: Own elaboration.

The second-order statistics of the velocity field are plotted in Figure 4.5. A good agreement can be observed for the profiles of the RMS velocity fluctuations of the Dynamic Smagorinsky and WALE models, and the UDNS compared with the DNS data of Zheng et al. (2019). Profiles of Reynolds shear stress for both SGS models and UDNS match the DNS results and the experimental data.

Figure 4.5 – Profiles of RMS velocity fluctuations in (a) axial, (b) radial, (c) azimuthal direction, and (d) Reynolds shear stress of Newtonian fluid plotted in wall units at $Re_G = 5,000$.

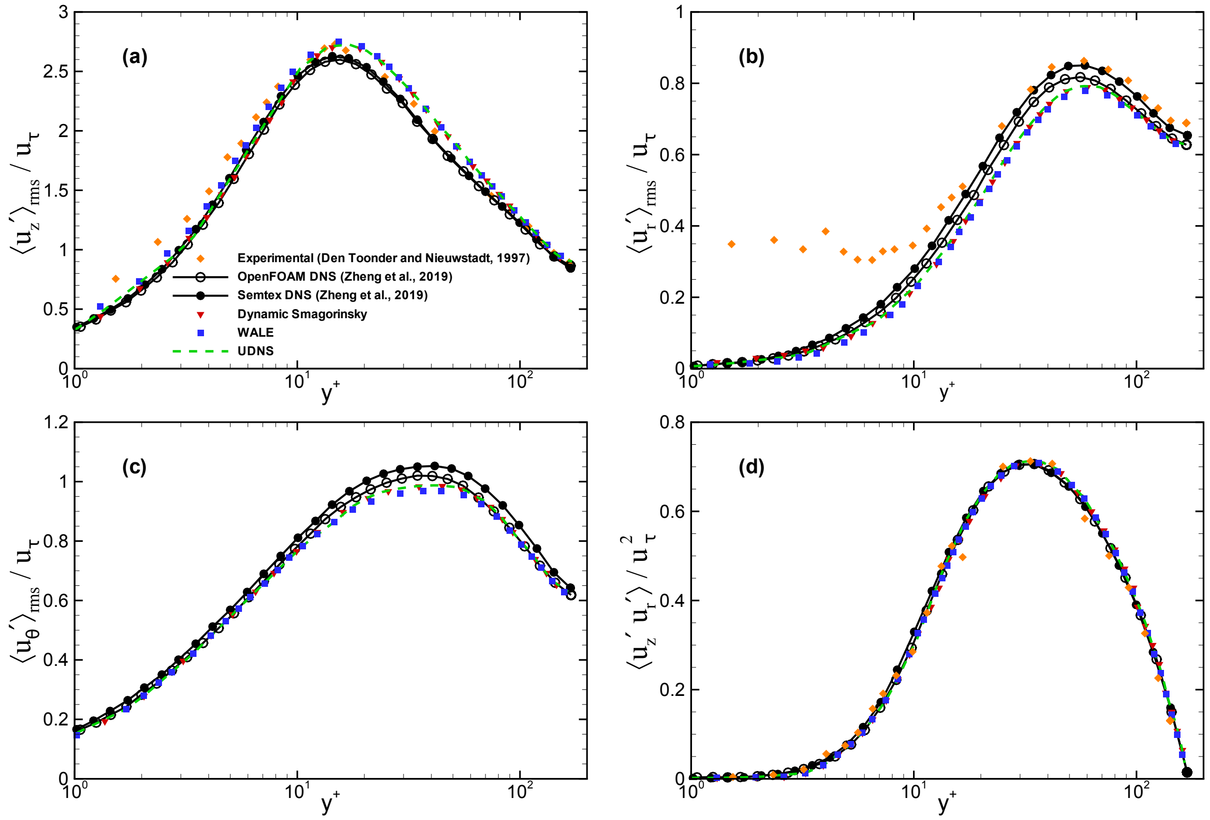

Source: Own elaboration.

Small differences (less than 2%) were observed between the SGS models predictions and the corresponding UDNS computations, suggesting that the numerical dissipation is dominant over the SGS dissipation rate. Similar results were observed by Castiglioni and Domaradzki (2015), Cadieux et al. (2017), and Komen et al. (2017). Kravchenko and Moin (1997) also pointed out that the contribution of the SGS models is small when applied in low-order methods.

4.1.5 Herschel-Bulkley Fluid

Simulations of turbulent pipe flow of Herschel–Bulkley fluids are carried out at two different generalized Reynolds numbers of $5,000$ and $7,500$. Following the work developed by Zheng et al. (2019), the model parameters are given in Table 4.4. The pipe diameter is 0.1 [m], the fluid density is 1,000 [$\mathrm{kg\ m^{-3}}$], and the bulk velocity is 1.0 [$\mathrm{m\ s^{-1}}$]. An additional simulation of turbulent pipe flow of Herschel–Bulkley fluids at $Re_G = 10,600$ is also presented in Appendix B.

Table 4.4 – Model parameters for the turbulent pipe flow simulations with Herschel-Bulkley fluids.

Simulation	τ_y (Pa)	K (Pa s^n)	n	Re_G	He	Bn
Case A	6.62e-02	1.22e-01	0.65	5,000	23	0.1215
Case B	4.28e-02	9.09e-02	0.65	7,500	23	0.1054

Source: Zheng et al. (2019).

4.1.5.1 Mean Velocity Profile

The mean axial velocity profiles for the simulations at $Re_G = 5,000$ and $Re_G = 7,500$ are illustrated in Figure 4.6. The profiles are normalized using the friction velocity u_τ. The Dynamic Smagorinsky and WALE models and the UDNS match the OpenFOAM DNS data of Zheng et al. (2019) up to the buffer layer ($y^+ \leq 30$). After that, the UDNS yields a lower velocity in the logarithmic region with a maximum deviation of 3.2%. For the simulations at $Re_G = 7,500$, the LES results follow the trend of OpenFOAM DNS data of Zheng et al. (2019).

As shown in Figure 4.6, the DNS axial velocity profiles predicted by OpenFOAM are slightly above the profiles obtained with *Semtex*, suggesting OpenFOAM predicts the flow to be more transitional for the shear-thinning fluids (ZHENG et al., 2019).

Figure 4.6 – Mean axial velocity profiles of Herschel-Bulkley fluids plotted in wall units at different generalized Reynolds numbers, (a) $Re_G = 5,000$ and (b) $Re_G = 7,500$.

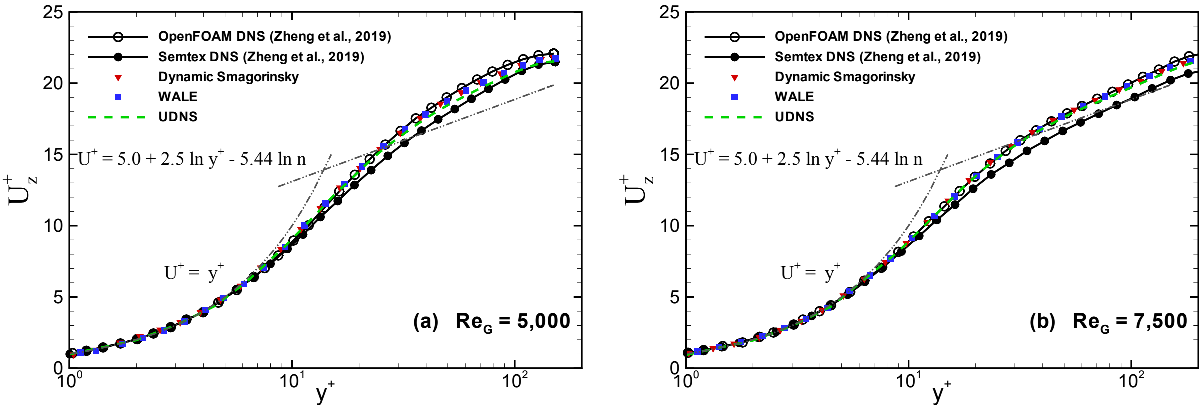

Source: Own elaboration.

4.1.5.2 RMS Velocity Fluctuations and Reynolds Shear Stress

The profiles of the RMS velocity fluctuations in the axial direction for the LES predictions at $Re_G = 5,000$ and $Re_G = 7,500$ are shown in Figure 4.7. The results obtained with the Dynamic Smagorinsky and WALE models and the corresponding UDNS computations present satisfactory agreement with OpenFOAM DNS data of Zheng et al. (2019) for both generalized Reynolds numbers. The current simulations predict the peak location. However, the LES simulations, as well as OpenFOAM DNS results (2019), overpredict the values by around 10% and 6% compared to *Semtex* DNS data of Zheng et al. (2019) for $Re_G = 5,000$ and $Re_G = 7,500$, respectively.

Figure 4.7 – Profiles of the RMS velocity fluctuations in the axial direction of Herschel-Bulkley fluids plotted in wall units , at different generalized Reynolds numbers, (a) $Re_G = 5,000$ and (b) $Re_G = 7,500$.

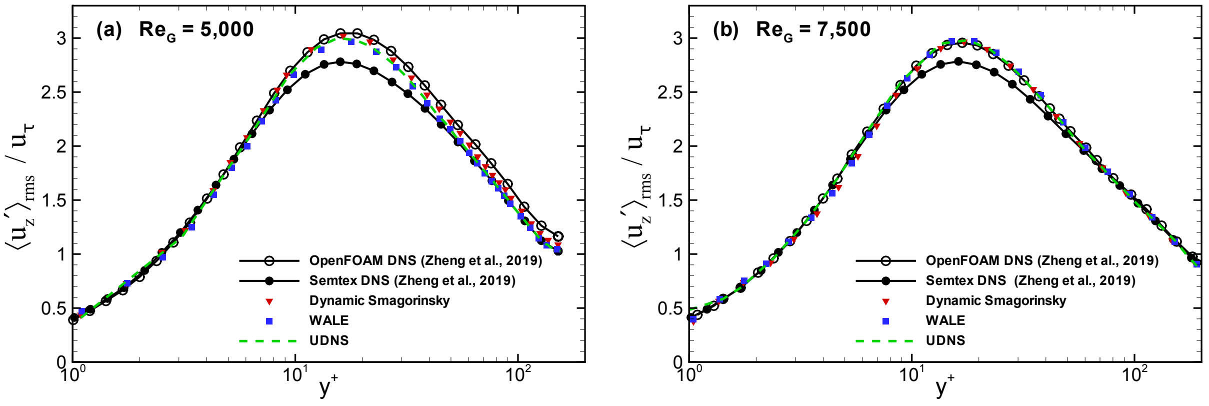

Source: Own elaboration.

Figure 4.8 depicts the profiles of RMS velocity fluctuations in the radial direction. The UDNS and the SGS models follow the trend of OpenFOAM DNS data of Zheng et al. (2019) at $Re_G = 5,000$. In the buffer layer ($5 < y^+ < 30$), the UDNS is in slightly better agreement with the OpenFOAM DNS data than the SGS models. However, the UDNS overpredicts the peak value by around 2.1%, whereas the SGS models overpredict this location by approximately 1.5% compared to OpenFOAM DNS data of Zheng et al. (2019). For the simulations at $Re_G = 7,500$, all the LES computations performed similarly with the OpenFOAM DNS data from Zheng et al. (2019).

Figure 4.8 – Profiles of the RMS velocity fluctuations in the radial direction of Herschel-Bulkley fluids plotted in wall units at different generalized Reynolds numbers, (a) $Re_G = 5,000$ and (b) $Re_G = 7,500$.

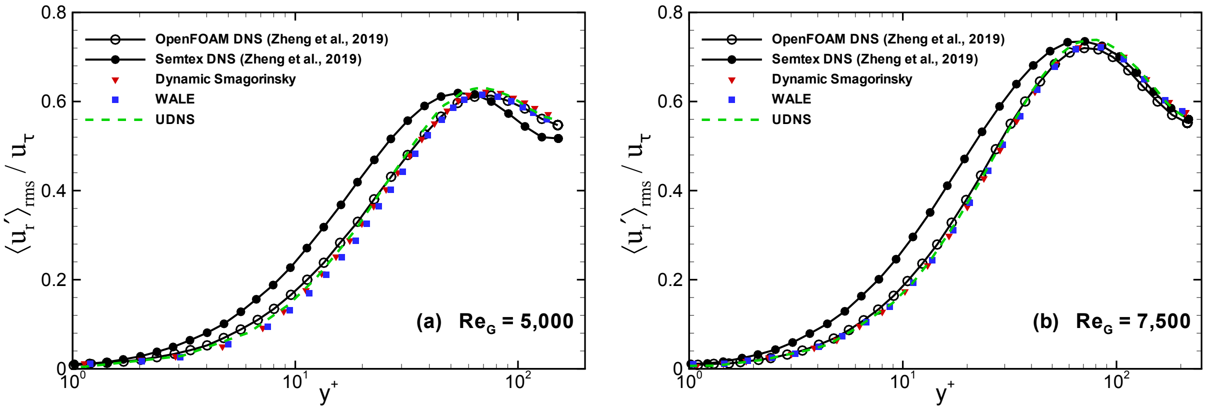

Source: Own elaboration.

Results for the profiles of the RMS velocity fluctuations in the azimuthal direction are reported in Figure 4.9. For the simulations at $Re_G = 5,000$, the SGS models and the corresponding UDNS predictions agree with the OpenFOAM DNS data from Zheng et al. (2019). The Dynamic Smagorinsky and WALE models overpredict the peak value by approximately 4.5% and 2%, respectively, while the difference for the UDNS at the peak is 5.87% compared to OpenFOAM DNS result (ZHENG et al., 2019). For $Re_G = 7,500$, in contrast, the profiles obtained with LES computations follow the trend of the OpenFOAM DNS data of Zheng et al. (2019).

Figure 4.9 – Profiles of the RMS velocity fluctuations in the azimuthal direction of Herschel-Bulkley fluids plotted in wall units at different generalized Reynolds numbers, (a) $Re_G = 5,000$ and (b) $Re_G = 7,500$.

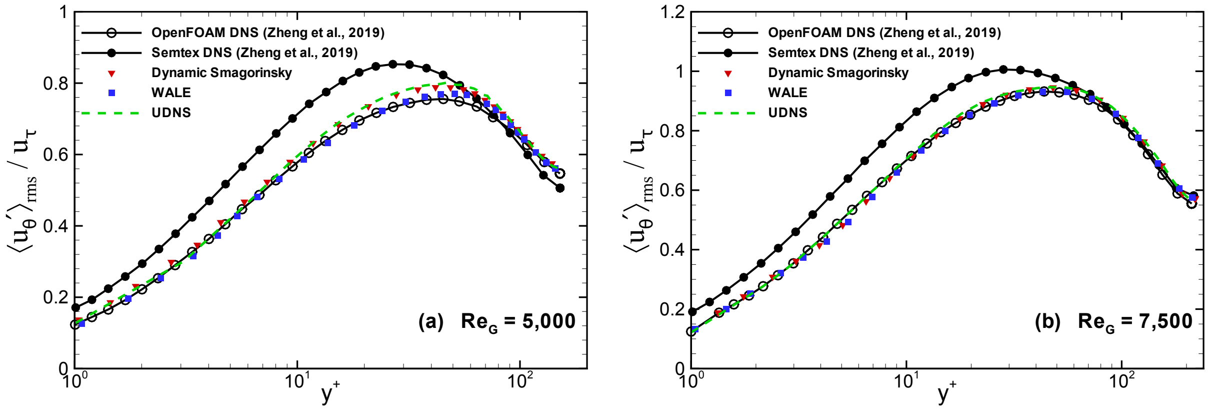

Source: Own elaboration.

Figure 4.10 shows the distribution of Reynolds shear stress. The profiles are normalized by u_τ^2. The Dynamic Smagorinsky and WALE models and the UDNS results agree well with DNS data of Zheng et al. (2019) for both generalized Reynolds numbers. The profiles of Reynolds shear stress obtained with LES follow the trend of the DNS results and correctly predict peak locations but present slightly larger values at these locations. The SGS models overpredict the peak value by approximately 6.5% for simulations at $Re_G = 5,000$, while the difference for the UDNS at the peak is 12% compared to OpenFOAM DNS data. For $Re_G = 7,500$, the Dynamic Smagorinsky and WALE models overpredict the peak value within 1.8%, while the maximum deviation from DNS data at the peak is 4.6% for the UDNS.

Figure 4.10 – Profiles of Reynolds shear stress of Herschel-Bulkley fluids plotted in wall units at different generalized Reynolds numbers, (a) $Re_G = 5,000$ and (b) $Re_G = 7,500$.

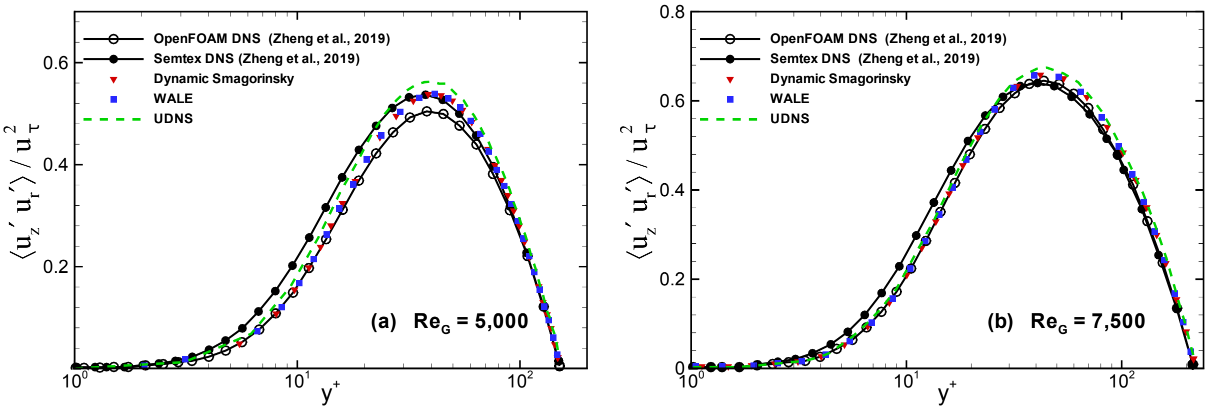

Source: Own elaboration.

It can be noted that the differences between the results of the first- and second-order statistics decreased as the Reynolds number increased, suggesting the difficulty of the code in computing transitional flows of non-Newtonian fluids.

Finally, an additional study regarding the turbulent intensities was performed at $Re_G = 7,500$ employing a coarse grid, mesh VI from Table 4.2, with grid resolution in wall units of $\Delta z^+ \approx 51$, $\Delta\theta^+ \approx 12$ and $\Delta r^+_{wall} = 0.52$. The distributions of the second-order statistics are shown in Figure 4.11. Even with a coarse grid, the results are in good agreement with the OpenFOAM DNS data of Zheng et al. (2019). The differences between the profiles obtained with SGS models and the results of the UDNS are small. However, following the trends presented above, the SGS models predict the peak values of the RMS velocity fluctuations in the radial and azimuthal directions and Reynolds shear stress better than the UDNS.

Figure 4.11 – Profiles of RMS velocity fluctuations in (a) axial, (b) radial, (c) azimuthal direction, and (d) Reynolds shear stress of Herschel–Bulkley fluid with the mesh VI plotted in wall units at $Re_G = 7,500$.

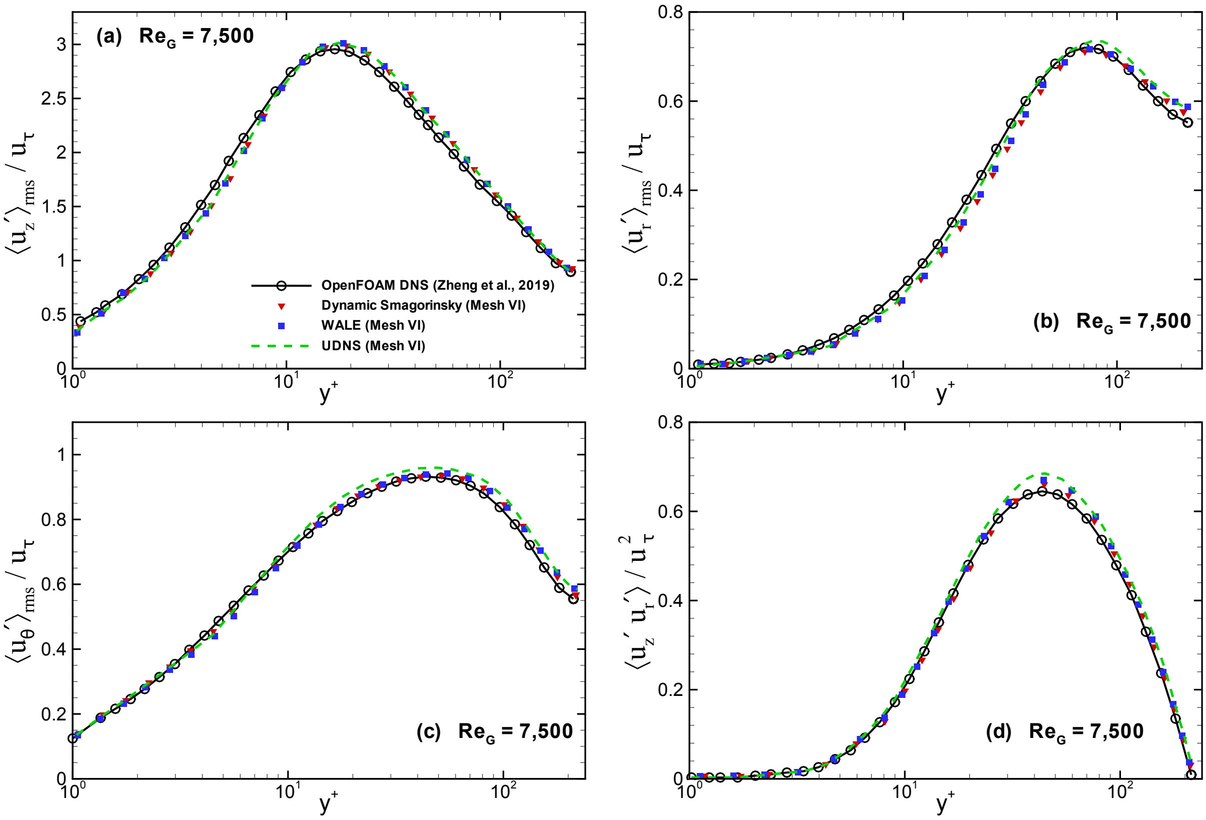

Source: Own elaboration.

4.1.5.3 Mean Viscosity and Shear Rate Profiles

The mean viscosity predictions normalized by the mean wall viscosity are plotted in Figure 4.12. The profiles obtained with the Dynamic Smagorinsky and WALE models and the results of the UDNS match the DNS data of Zheng et al. (2019) for both generalized Reynolds numbers. Near the wall, the apparent viscosity is constant up to the viscous sublayer ($y^+ < 5$).

Results for the mean shear rate normalized by u^2_τ/ν_w are illustrated in Figure 4.13. The profiles show that the highest shear rate values are located near the pipe wall. The most considerable difference in the mean shear rate between the LES computations and OpenFOAM DNS results of Zheng et al.

(2019) occurs near the wall, both SGS models and the predictions of the UDNS overestimate OpenFOAM DNS values. After that region, very similar results are observed. When the profiles computed by the OpenFOAM package are compared to *Semtex* DNS data from Zheng et al. (2019), the values are slightly smaller for the whole domain.

Figure 4.12 – Profiles of Reynolds shear stress of Herschel-Bulkley fluids plotted in wall units at different generalized Reynolds numbers, (a) $Re_G = 5,000$ and (b) $Re_G = 7,500$.

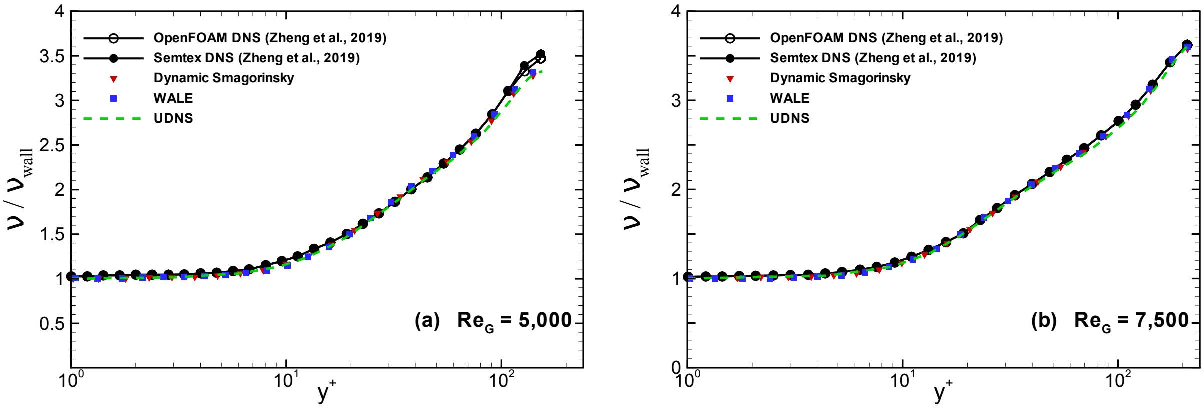

Source: Own elaboration.

Figure 4.13 – Profiles of Reynolds shear stress of Herschel-Bulkley fluids plotted in wall units at different generalized Reynolds numbers, (a) $Re_G = 5,000$ and (b) $Re_G = 7,500$.

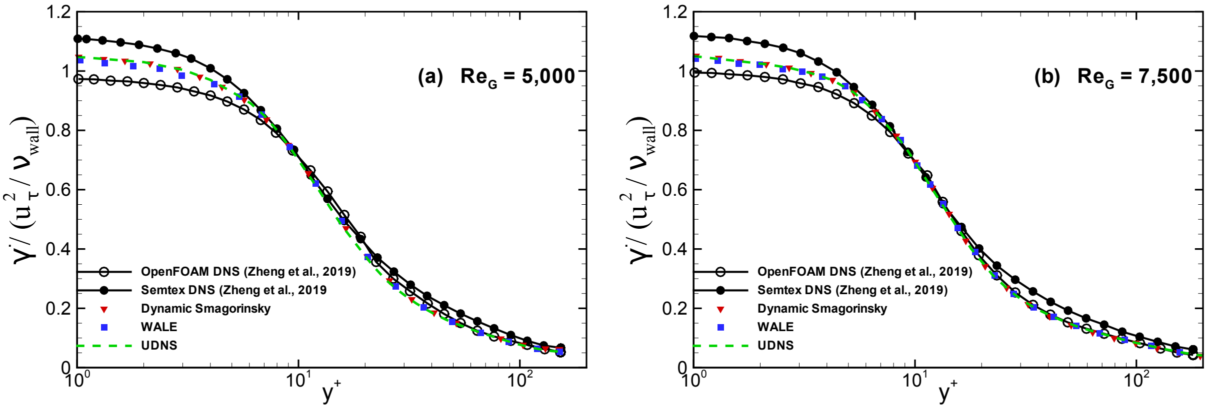

Source: Own elaboration.

4.1.5.4 Wall Shear Stress, Pressure Gradient, and Wall Viscosity

The mean wall shear stress τ_w and the mean pressure gradient dp/dz from the reference DNS data of Zheng et al. (2019), and their respective averaged quantities computed by LES are summarized in Table 4.5. The ensemble-averaged wall shear stress $\langle \tau_w \rangle$ and ensemble-averaged pressure gradient $\langle \partial P/\partial z \rangle$ are obtained *a posteriori*. The current computations agree well with the DNS results. The SGS models predict the mean wall shear stress better than the UDNS for both cases. It is worth noting that the maximum deviation from DNS data is approximately 4.5% for the UDNS.

Table 4.5 – Comparison between the reference DNS data of Zheng et al. (2019) for mean wall shear stress and mean pressure gradient with the ensemble-averaged quantities of wall shear stress and pressure gradient computed by LES.

	Case A		Case B	
	τ_w $[Pa]$	$\partial P/\partial z$ $[Pa\,m^{-1}]$	τ_w $[Pa]$	$\partial P/\partial z$ $[Pa\,m^{-1}]$
Semtex DNS (ZHENG et al., 2019)	3.70	148.0	3.35	134.0
OpenFOAM DNS (ZHENG et al., 2019)	3.70	148.0	3.35	134.0
	$\langle\tau_w\rangle$ $[Pa]$	$\langle\partial P/\partial z\rangle$ $[Pa\,m^{-1}]$	$\langle\tau_w\rangle$ $[Pa]$	$\langle\partial P/\partial z\rangle$ $[Pa\,m^{-1}]$
Dynamic Smagorinsky	3.76	150.5	3.45	138.0
WALE	3.77	150.8	3.45	138.0
UDNS	3.83	153.2	3.44	140

Source: Own elaboration.

The mean wall viscosity η_w is a crucial variable to quantify the generalized Reynolds number for GNFs. The mean wall viscosity (see Eq.2.10) can be determined *a priori* in experiments from the measurements of the mean pressure gradient (SINGH et al., 2017a). In contrast, the ensemble-averaged wall viscosity $\langle\eta_w\rangle$ is obtained *a posteriori* in simulations.

The ensemble-averaged wall viscosity computed by LES and the mean wall viscosity from the reference DNS data of Zheng et al. (2019) are summarized in Table 4.6. It can be observed that the differences between LES predictions and DNS data are smaller than 1.5% for all cases.

Table 4.6 – Comparison between the reference DNS data of Zheng et al. (2019) for mean wall viscosity with the ensemble-averaged wall viscosity computed by LES.

	Case A	Case B
	η_w $[Pa\ s]$	η_w $[Pa\ s]$
Semtex DNS (ZHENG et al., 2019)	1.999e-02	1.329e-02
OpenFOAM DNS (ZHENG et al., 2019)	1.999e-02	1.348e-02
	$\langle\eta_w\rangle$ $[Pa\ s]$	$\langle\eta_w\rangle$ $[Pa\ s]$
Dynamic Smagorinsky	2.014e-02	1.328e-02
WALE	2.016e-02	1.332e-02
UDNS	1.996e-02	1.319e-02

Source: Own elaboration.

4.1.5.5 Generalized Reynolds Number and the Fanning Friction Factor

The generalized Reynolds numbers obtained with LES and reference DNS values from Zheng et al. (2019) are presented in Table 4.7. The difference between the generalized Reynolds numbers values is mainly due to the velocity difference used in the simulations. The *Semtex* DNS of Zheng et al. (2019) underpredicts the bulk velocity by 4.9% and 7.2% for cases A and B, respectively. In contrast, the OpenFOAM DNS from Zheng et al. (2019) underestimates the bulk velocity by 1.9% for case B.

Table 4.7 – Reference DNS data of Zheng et al. (2019) and LES results for Generalized Reynolds numbers (the expected bulk velocity is 1.0 [$m\ s^{-1}$].

	Case A		Case B	
	Re_G	Actual U_b [$m\ s^{-1}$]	Re_G	Actual U_b [$m\ s^{-1}$]
Semtex DNS (ZHENG et al., 2019)	4757	0.9510	6980	0.9280
OpenFOAM DNS (ZHENG et al., 2019)	5018	1.003	7277	0.9810
Dynamic Smagorinsky	4965	1.00	7529	1.00
WALE	4960	1.00	7509	1.00
UDNS	5013	1.00	7583	1.00

Source: Own elaboration.

Table 4.8 compares the Fanning friction factor using LES with DNS data of Zheng et al. (2019). The Fanning friction factor, f, is defined as

$$f = \frac{\tau_w}{\frac{1}{2}\rho U_b^2} \tag{4.3}$$

For case A ($Re_G = 5,000$), the Fanning friction factor obtained with LES agrees well with the OpenFOAM DNS result of Zheng et al. (2019). The maximum deviation is approximately 1.5% for the SGS models and 3.5% for the UDNS. For case B ($Re_G = 7,500$), the UDNS matches the OpenFOAM DNS result of Zheng et al. (2019), while the Dynamic Smagorinsky and WALE models underpredict by about 1.5%.

When the friction factor computed by the OpenFOAM package is compared to *Semtex* DNS data from Zheng et al. (2019) the values are underestimated by around 12%.

Table 4.8 – Reference DNS data of Zheng et al. (2019) and LES results for Fanning friction factor (the expected bulk velocity is 1.0 [$m\ s^{-1}$].

	Case A		Case B	
	f x10^{-3}	Actual U_b [$m\ s^{-1}$]	f x10^{-3}	Actual U_b [$m\ s^{-1}$]
Semtex DNS (ZHENG et al., 2019)	8.20	0.9510	7.80	0.9280
OpenFOAM DNS (ZHENG et al., 2019)	7.40	1.003	7.00	0.9810
Dynamic Smagorinsky	7.52	1.00	6.90	1.00
WALE	7.54	1.00	6.90	1.00
UDNS	7.77	1.00	7.00	1.00

Source: Own elaboration.

4.1.6 Summary

Profiles of first- and second-order turbulence statistics computed by the Dynamic Smagorinsky and WALE models, and the UDNS (or no-model LES) agreed well with the DNS results from Zheng et al.

(2019) and experimental data from Den Toonder and Niewstadt (1997) for the simulations with Newtonian fluid in a turbulent pipe flow.

The results obtained using the SGS models and the UDNS for Herschel-Bulkley fluids showed a good agreement with reference DNS data. The current computations adequately reproduced the first- and second-order turbulence statistics.

The profiles computed with LES were qualitatively consistent with each other for second-order statistics of the velocity field. However, the SGS models agreed better with the DNS data than the UDNS predictions for the peak values of the RMS velocity fluctuations and Reynolds shear stresses. The maximum difference of the RMS velocity fluctuations was approximately 6% from the DNS results of OpenFOAM in predicting the peak in the azimuthal direction at $Re_G = 5,000$, while the peak value of the Reynolds shear stress is overestimated by 12%.

The differences between the results of the second-order statistics decreased as the Reynolds number increased. The LES simulations are qualitatively consistent with OpenFOAM DNS data for the RMS velocity fluctuations. The maximum difference was 4.6% in predicting the peak in the Reynolds shear stress at $Re_G = 7,500$ with the UDNS.

When the DNS results of RMS velocity fluctuations computed by the OpenFOAM package are compared to *Semtex* DNS data the relative differences in axial, radial, and azimuthal turbulence intensities at the peak for $Re_G = 5,000$ are 10.0%, 5.9% and 15.7%, respectively. For the simulations at $Re_G = 7,500$, the differences decreasing to 6.3%, 2.0% and 7.7% (ZHENG et al., 2019).

The distributions of mean viscosity, mean shear rate, mean wall shear stress, mean wall viscosity, and friction factor for Herschel-Bulkley fluids were also computed. The UDNS and the SGS models followed the trends of the DNS data.

4.2 Turbulent Flow in a Concentric Annulus

Numerical simulations of Newtonian fluid flow in a concentric annular with inner cylinder rotation were performed at $Re = 8,900$ for two different rotation rates ($N = 0.214$ and 0.429), following the work developed by Chung and Sung (2005). The rotation rate N is defined as

$$N = \frac{\Omega R_{rc}}{U_b} \tag{4.4}$$

where Ω is the angular velocity and R_{rc} is the radius of the rotating cylinder. The radius ratio, $R_r^* = R_i/R_o$, was set 0.5 for all simulations with R_i and R_o standing for the radius of the inner and outer cylinder, respectively.

The axial domain length was defined as $L_z = 18\delta$, where δ is one-half the cylinder gap, $\delta = (R_o - R_i)/2$ and the azimuthal domain size was set as $L_\theta = \pi/2$. As the work of Chung and Sung (2005) was also performed with LES using the Dynamic Smagorinsky model, the mesh analysis will not be accomplished. Figure 4.14 depicts a schematic view of the annular region, and Table 4.9 summarizes the computational domain and grids resolutions for the simulations.

Figure 4.14 – Schematic representation of the annular region for $L_\theta = \pi/2$.

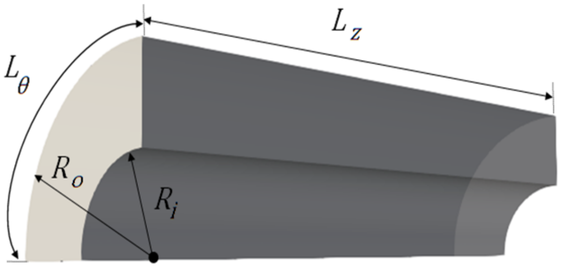

Source: Own elaboration.

Table 4.9 – Summary of the computational grid used for the flow simulations in a concentric annular region at $Re = 8,900$. Comparisons with the Chung and Sung (2005) data.

-	Chung and Sung (2005)	Present LES	Chung and Sung (2005)	Present LES
N	0.2145	0.2145	0.429	0.429
L_z	18 δ	18 δ	18 δ	18 δ
L_θ	$\pi/2$	$\pi/2$	$\pi/2$	$\pi/2$
N_z	128	128	192	192
N_r	65	65	65	65
N_θ	64	64	64	64
Δz^+	22.95	22.13	16.80	17.30
Δr^+_{in}	0.27	0.33	0.30	0.33
Δr^+_{out}	0.23	0.30	0.24	0.29
Δr^+_{max}	13.86	17.55	15.23	18.38
$R_{in}\Delta\theta^+$	8.01	7.74	8.80	8.39
$R_{out}\Delta\theta^+$	13.86	14.39	14.34	15.23

Source: Own elaboration.

4.2.1 Initial and Boundary Conditions

The same approach developed by DE VILLIERS (2006) was used in Section 4.1.1 to create the initial velocity field for the Newtonian case in a circular pipe was employed to initialize the flow field of the annular region.

Periodic boundary conditions were applied in the axial $\phi(z,r,\theta) = \phi(z+L_z,r,\theta)$ and circumferential directions $\phi(z,r,\theta) = \phi(z,r,\theta+L_\theta)$. The no-slip boundary condition was imposed on the walls; the inner wall rotated at a constant angular velocity while the outer wall remained stationary. The velocity field at the walls of the annular region was expressed as

$$\begin{cases} \mathbf{u}(z, r = R_i, \theta, t) &= -\Omega R_i \\ \mathbf{u}(z, r = R_o, \theta, t) &= \quad 0 \end{cases} \tag{4.5}$$

4.2.2 Averaging Procedure

Similar to the process described in Section 4.1.2, after the flow reaches a statistically steady state for the annular region, the statistical quantities were computed by $960\delta/U_b$, equivalent to 40 FTT. Then, the spatial averaging was performed over the homogeneous directions during the post-processing.

4.2.3 Results and Discussions

Figure 4.15 illustrates the profiles of mean axial and tangential velocity predicted by the Dynamic Smagorinsky and WALE models, UDNS, and the corresponding LES results of Chung and Sung (2005). The velocity profiles agree well with the reference data for both rotation rates, N = 0.2145 and N = 0.429.

Figure 4.15 – Profiles of (a) mean axial velocity normalized by the bulk velocity and (b) mean tangential velocity normalized by the velocity at the inner wall. Left: $N = 0.2145$; Right: $N = 0.429$. The parameter r^* stands for the non-dimensional radial coordinate, $r^* = (r-R_i)/(R_o-R_i)$.

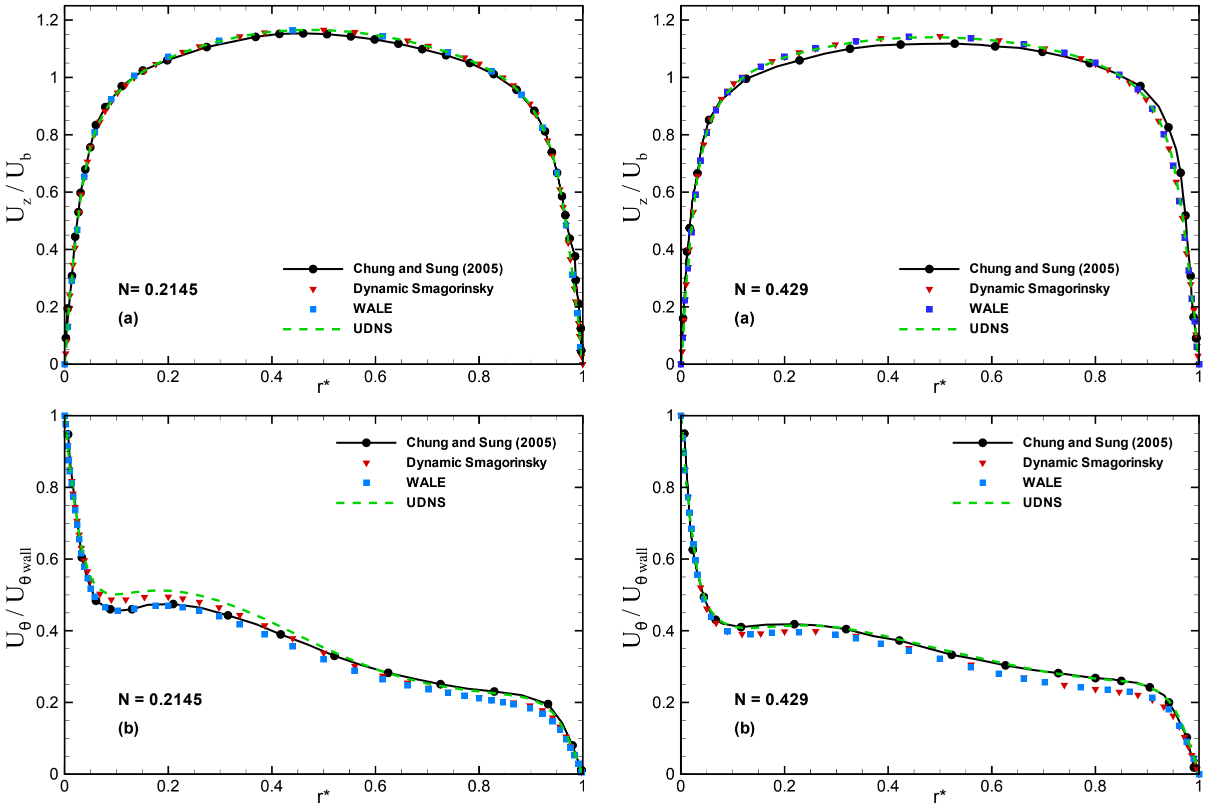

Source: Own elaboration.

Results for the RMS velocity fluctuations are plotted in Figure 4.16, while those obtained for the Reynolds stresses are presented in Figure 4.17. The profiles computed with the SGS models and the UDNS produce very similar distributions, and the predictions are qualitatively consistent with the Chung and Sung (2005) data, except for the Reynolds $r\theta$ stress components that deviate from the reference results for values above $r^* > 0.6$.

Figure 4.16 – Profiles of RMS velocity fluctuations in (a) axial, (b) radial, and (c) azimuthal direction. Left: $N = 0.2145$; Right: $N = 0.429$. The parameter r^* stand for the non-dimensional radial coordinate, $r^* = (r - R_i)/(R_o - R_i)$.

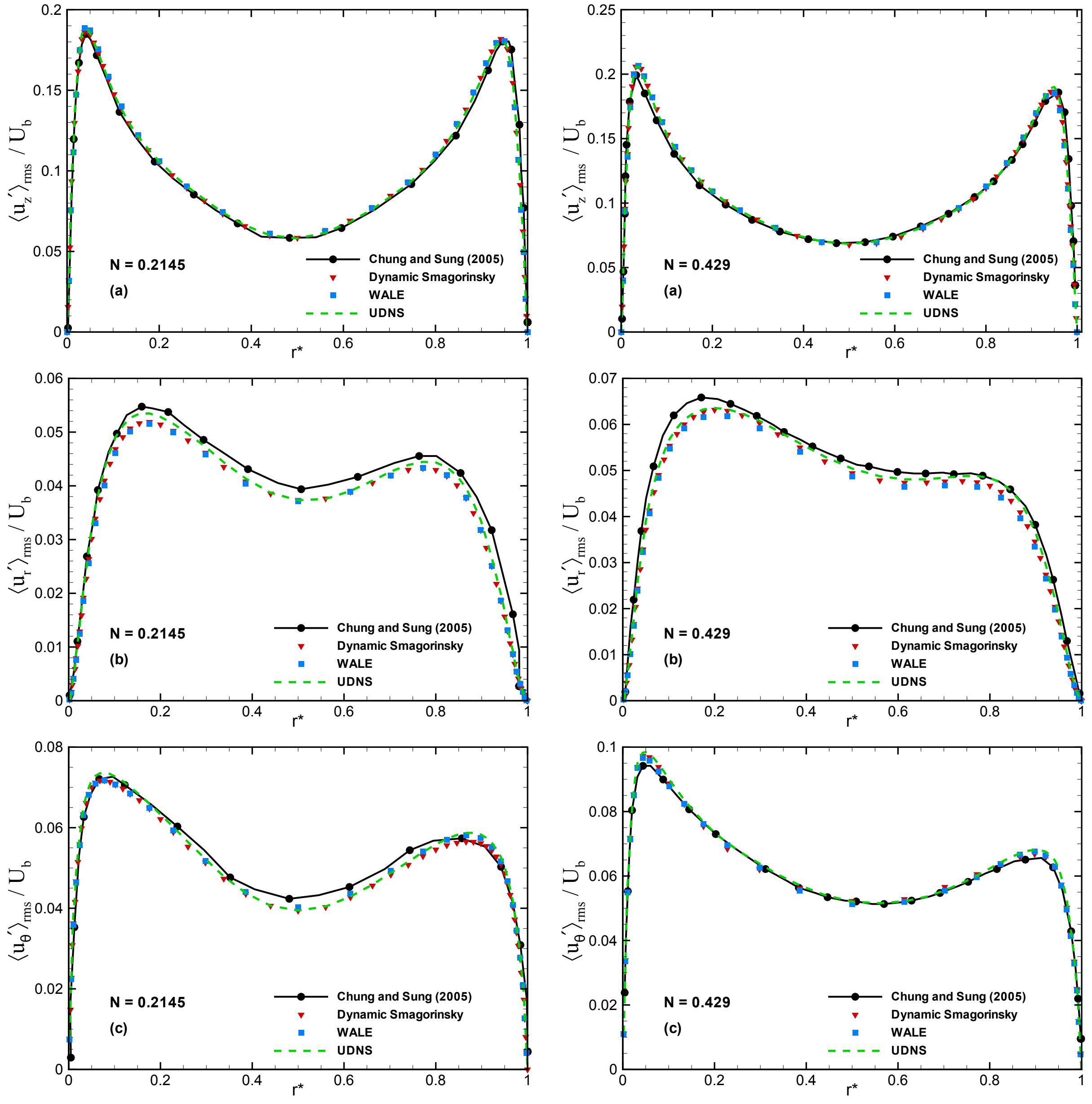

Source: Own elaboration.

Figure 4.17 – Profiles of the Reynolds stress, (a) Reynolds zr stress component and (b) Reynolds $r\theta$ stress component. Left: $N = 0.2145$; Right: $N = 0.429$.

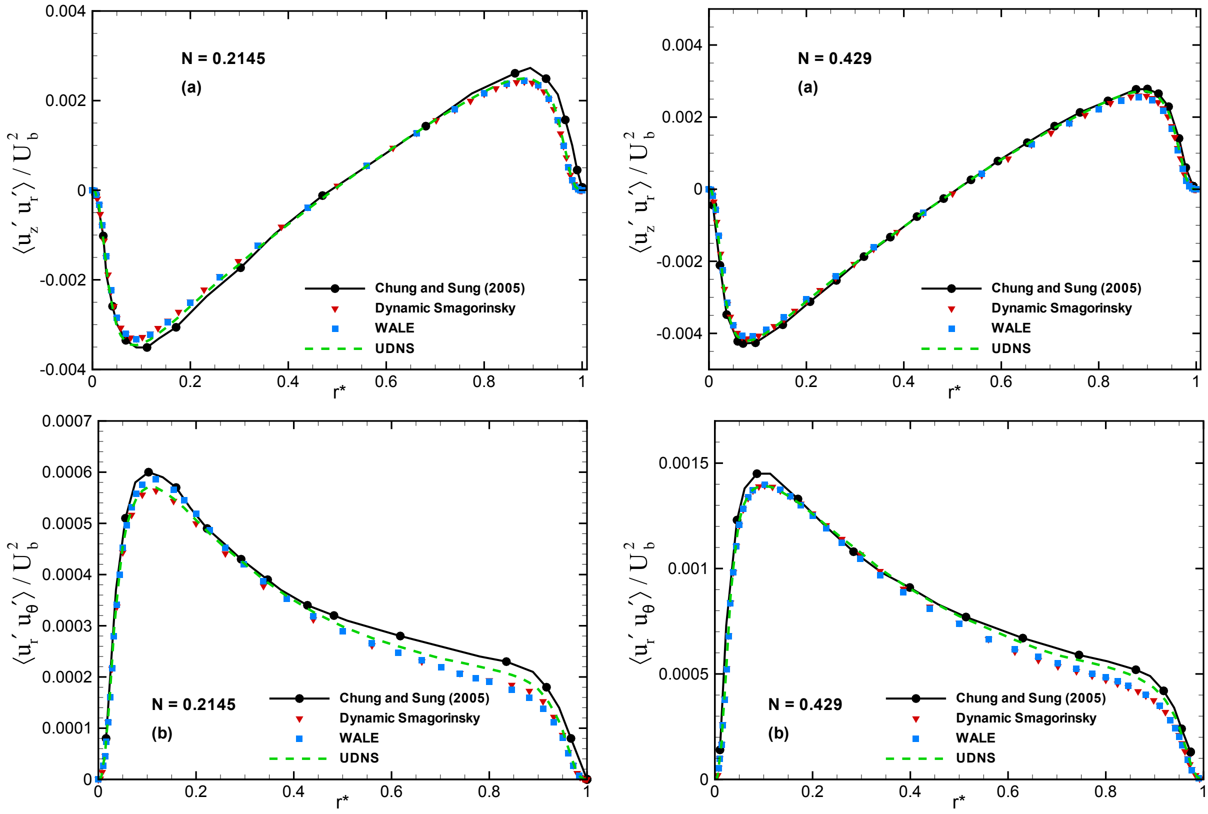

Source: Own elaboration.

Chapter Summary

In this chapter, simulations were performed to assess the capacity and limitations of the present numerical method. The LES predictions obtained with Dynamic Smagorinsky and WALE models and the results of the UDNS demonstrated good predictability compared to the reference data for turbulent pipe flows with both Newtonian and Herschel-Bulkley fluids and turbulent flows in an annular section with Newtonian fluid. Therefore, in the following chapter, the present methodology will perform numerical simulations of turbulent flows in a concentric annular section with Herschel-Bulkley fluids.

5 TURBULENT FLOW OF HERSCHEL-BULKLEY FLUIDS IN A CONCENTRIC ANNULAR SECTION WITH ROTATION OF THE INNER CYLINDER

This chapter presents the results of the turbulent concentric annular flow of Herschel-Bulkley fluids with inner cylinder rotation. The LES methodology considered in the previous section is used here. The influence of the fluid behavior index n, the Bingham number B_n, and the Rotation number N on the flow quantities are discussed. The chapter is organized as follows. The flow parameters studied are described in the next section. In sequence, details of the geometrical configuration, initial field, and averaging procedure are presented. The grid convergence study is also given. In section 5.5, the fluid behavior index results are discussed; in Section 5.6 the influence of the Bingham number is reported. In Section 5.7, the effect of the Rotation number is considered; and in Section 5.8, the comparison between SGS models and UDNS is provided.

5.1 Flow Parameters

In order to assess the influence of the flow behavior index *n*, three values are considered; $n = 0.65, 0.70$ and 0.75. For values below $n = 0.65$, the simulations show a re-laminarization of turbulent flow at $Re_G \approx 9,000$. The effect of the Bingham number on the flow quantities is measured with $B_n = 0.10, 0.25$ and 0.40. The effect of the inner cylinder rotation is investigated at $N = \Omega R_{rc}/U_b = 0.15$ and $N = 0.30$. In the present work, $N = 0.15$ stands for the inner cylinder rotating at 55 rpm and $N = 0.30$ corresponds to 110 rpm. These rotation ranges generally are employed in the drill pipe to help the hole cleaning during the oil drilling process (KELIN et al., 2013). Table 5.1 summarizes the parameters that will be analyzed in this chapter.

Table 5.1 – Summary of the flow parameters evaluated.

Parameters	Values
Bingham number B_n	0.10; 0.25; 0.40
Flow behavior index n	0.65; 0.70; 0.75
Rotation rate N	0.15; 0.30

Source: Own elaboration.

Simulations were run at the fixed mass flow rate. For cases at $N = 0.15$, the generalized Reynolds numbers measured *a posteriori* are around $Re_G \approx 9,000$, while for those performed at $N = 0.30$, the generalized Reynolds numbers increased slightly to $Re_G \approx 9,200$ due to the rotation effect. Table 5.2 presents the set of case studies in this chapter.

From Table 5.2, it is possible to select some cases to study the parameters individually. For instance, comparing simulations 01, 02, and 03, only the n effect on the flow characteristics is evaluated. Additionally, comparing simulations 03, 05, and 07, the Bingham number is varied and its influence on the flow features is analyzed, while the other parameters remain fixed.

Table 5.2 – Set of simulations to investigate the flow features.

Sim	B_n	n	U_b $[m\ s^{-1}]$	N	Re_G
01	0.10	0.75	1.93	0.15	9,030
02	0.10	0.70	1.93	0.15	9,010
03	0.10	0.65	1.93	0.15	9,060
04	0.25	0.70	1.93	0.15	9,020
05	0.25	0.65	1.93	0.15	9,050
06	0.40	0.70	1.93	0.15	9,020
07	0.40	0.65	1.93	0.15	9,020
08	0.10	0.75	1.93	0.30	9,110
09	0.10	0.65	1.93	0.30	9,190
10	0.25	0.75	1.93	0.30	9,160
11	0.25	0.70	1.93	0.30	9,190
12	0.25	0.65	1.93	0.30	9,180
13	0.40	0.75	1.93	0.30	9,100
14	0.40	0.70	1.93	0.30	9,180
15	0.40	0.65	1.93	0.30	9,190

Source: Own elaboration.

The LES simulations up to section 5.7 were executed with the WALE model as it has a lower computational cost ($\approx$7%) than other methods.

5.2 Details of the Geometrical Configuration

The flow of non-Newtonian fluids is bounded by two concentric cylinders, where the inner cylinder rotates at a constant angular velocity while the outer one is stationary. The geometry is illustrated in Figure 5.1. The computational length of the annular section in the axial direction varies from $L_z = 24\delta$ to $L_z = 26\delta$ and the azimuthal domain size is fixed to $L_\theta = 9\pi/9.1$. In addition, the radius ratio, $R_r^* = R_i/R_o$, was set 0.5 for all simulations.

Since periodic boundary conditions are applied in the axial and azimuthal directions, the sizes of computational domains are verified via two-point correlations to ensure that the periodicity does not influence the results. The axial and azimuthal two-point correlations for the axial velocity fluctuations are defined as (RODI et al., 2013; BAGUERI et al., 2020)

$$R_{zz}(\Delta z) = \frac{\langle u_z'(z,\theta,r,t)\ u_z'(z+\Delta z,\theta,r,t)\rangle}{\langle u_z'(z,\theta,r,t)\ u_z'(z,\theta,r,t)\rangle} \tag{5.1}$$

Figure 5.1 – Schematic representation of the annular section

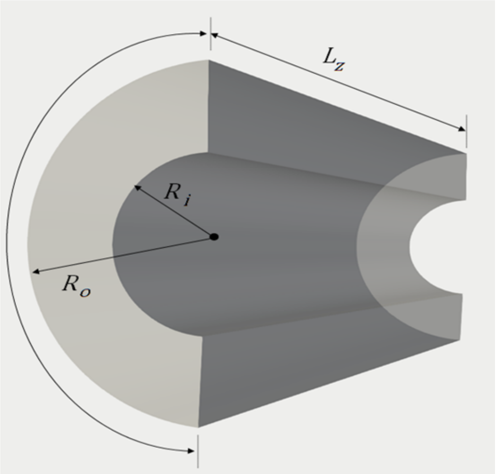

Source: Own elaboration.

and

$$R_{zz}(\Delta\theta) = \frac{\langle u'_z(z,\theta,r,t)\, u'_z(z,\theta+\Delta\theta,r,t)\rangle}{\langle u'_z(z,\theta,r,t)\, u'_z(z,\theta,r,t)\rangle} \tag{5.2}$$

respectively.

The $R_{zz}(\Delta z)$ correlation was evaluated at three radial locations; on the surface of the inner and outer walls at $y^+ = 15$, near the point where the axial turbulence intensity reaches its peak value and at the middle of the gap of the annular section. Figure 5.2 depicts the profiles of the two-point correlation of the axial velocity fluctuations in the streamwise direction for Sim 01 and Sim 08 (most developed turbulent flow for $N = 0.15$ and $N = 0.30$, respectively) and Sim 07 and Sim 15 (simulations with weaker turbulent structures for $N = 0.15$ and $N = 0.30$, correspondingly). As introduced in the literature review, the reduction of *n* and the increase of yield stress act as turbulence dampers for fluid flow at the same Reynolds number.

For all simulations performed with the Rotation number $N = 0.15$, the axial domain length is fixed to $L_z = 26\delta$, while for those with $N = 0.30$ the domain is set to $L_z = 24\delta$. This difference in the L_z occurs because in simulations with $N = 0.15$ and $L_z = 24\delta$ the $R_{zz}(\Delta z)$ quantities were around 0.2, so the axial length was increased to reduce the $R_{zz}(\Delta z)$ values to close to zero. Therefore, from Figure 5.2, the results suggest that the sizes of computational domains in the axial direction are appropriate for all cases.

Figure 5.3 shows the two-point correlations $R_{zz}(\Delta\theta)$ of the axial velocity fluctuations in the azimuthal direction for Sim 07 and Sim 08 at $y^+ = 15$ on the surfaces of the inner and outer walls. It can be noted that the profiles fall off to zero, suggesting that the computational domain size in the azimuthal direction is adequate for the simulations.

Figure 5.2 – Profiles of two-point correlation functions of the axial velocity fluctuation computed over the surface located at $y^+ = 15$ from the inner and outer walls and the middle of the gap. Top: $N = 0.15$; bottom: $N = 0.30$.

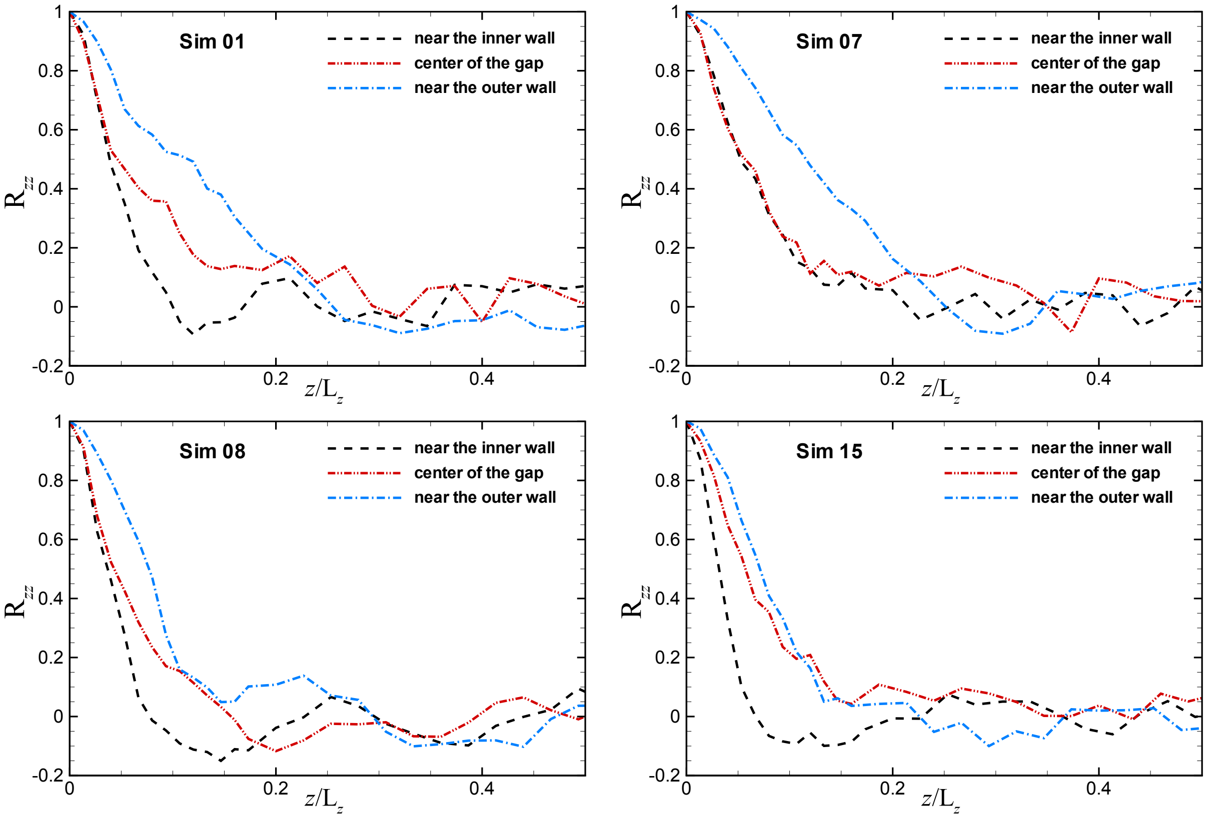

Source: Own elaboration.

Figure 5.3 – Profiles of two-point correlation functions of the axial velocity fluctuation in the azimuthal direction computed over the surface located at $y^+ = 15$ from the inner and outer walls.

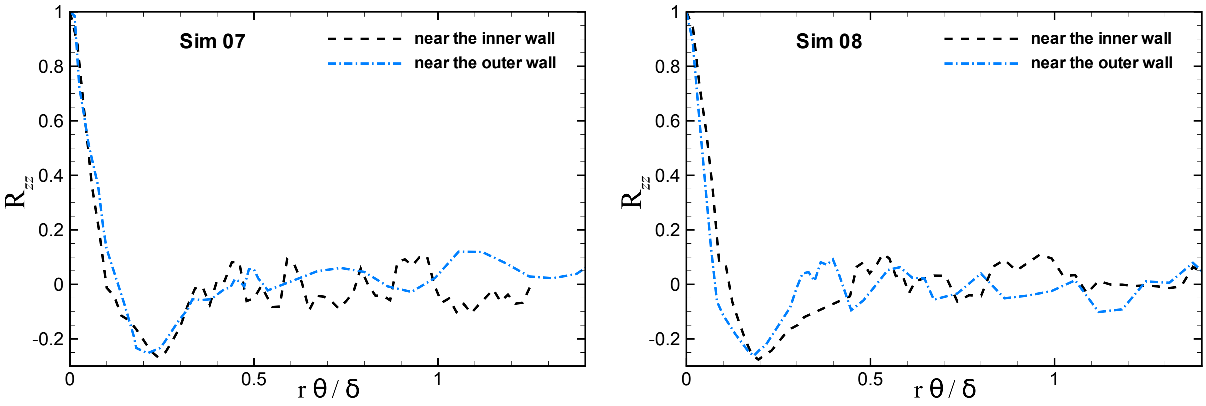

Source: Own elaboration.

5.3 Initial Field and Averaging Procedure

Similar to the discussion introduced in subsections 4.1.1 and 4.1.2. The simulations with Herschel-Bulkley fluids were initialized with a fully developed Newtonian flow field. The DE VILLIERS (2006)'s approach was employed to create an initial field for the Newtonian case. Regarding the computations of statistical quantities, 10 *FTT* are skipped from time averaging until a statistically steady state is reached. Subsequently, statistics were collected for 40 *FTT*. As the final step, the spatial averaging was carried out over the homogeneous directions during the post-processing.

5.4 Grid Convergence Study

Table 5.3 summarizes the grid resolutions used by several authors for simulations of the turbulent concentric annular pipe flow of Newtonian fluid performed with the DNS and LES methods at $Re \approx 8900$. Therefore, it provides insight regarding the proper mesh density to perform in the current simulations.

Four different grid levels were considered to assess the sensitivity of the results. The mesh parameters, including non-dimensional grid resolutions Δr^+, $R\Delta\theta^+$ and Δz^+, and the number of cells for $\Delta r^+ \leq 5$ (viscous sublayer) and $\Delta r^+ \leq 10$ are given in Table 5.4. The grid points are equally spaced in both axial and azimuthal directions, while in the radial coordinate the elements were distributed by geometric progression to ensure $\Delta r^+ < 1$ for the first volume adjacent to the wall. The mesh convergence study is executed with Sim 08, as it is the case that presents the most developed turbulent flow (higher flow behavior index and Rotation number, and lower Bingham number).

Table 5.3 – Grid resolutions used by several authors for the turbulent concentric annular flow of Newtonian fluid performed with DNS and LES at $Re \approx 8900$

-	Chung et al. (2002) - DNS	Chung and Sung (2005) - LES	Schneider et al. (2017) - LES
Δz^+	14.30	22.95	24
Δr^+_{in}	0.13	0.27	0.31
Δr^+_{out}	0.12	0.23	0.27
Δr^+_{max}	12.96	13.86	21.40
$R_{in}\Delta\theta^+$	3.75	8.01	5.70
$R_{out}\Delta\theta^+$	7.10	13.86	10.40

Source: Own elaboration.

Table 5.4 – Details of considered grid resolutions for the convergence study.

Mesh	I	II	III	IV
N$_z$ x N_r x N_θ	100x54x75	50x54x150	100x54x150	150x54x150
Number of cells	405,000	405,000	810,000	1,215,000
Δz^+	37.5	76.60	37	24.5
Δr^+_{in}	0.43	0.50	0.42	0.42
Δr^+_{out}	0.32	0.40	0.31	0.31
Δr^+_{max}	18.5	19	18.5	18.3
$R_{in}\Delta\theta^+$	13.72	7.3	7.1	7.0
$R_{out}\Delta\theta^+$	20	10.5	10.8	10.4
Number of cells for $r^+ \leq 5$	9	9	9	9
Number of cells for $r^+ \leq 10$	14	4	14	14

Source: Own elaboration.

Profiles of the mean axial velocity normalized by the bulk velocity and the azimuthal velocity normalized by the rotational velocity of the inner wall are reported in Figure 5.4. On the horizontal axis, $r^* = (R - R_i)/(R_o - R_i) = 0$ and 1 correspond to the inner- and outer-cylindrical wall surfaces, respectively.

Figure 5.4 – Profiles of the mean (a) axial and (b) azimuthal velocity for different grid resolutions. The bulk velocity normalizes the mean axial velocity, and the mean azimuthal velocity is normalized by the rotational velocity of the inner wall.

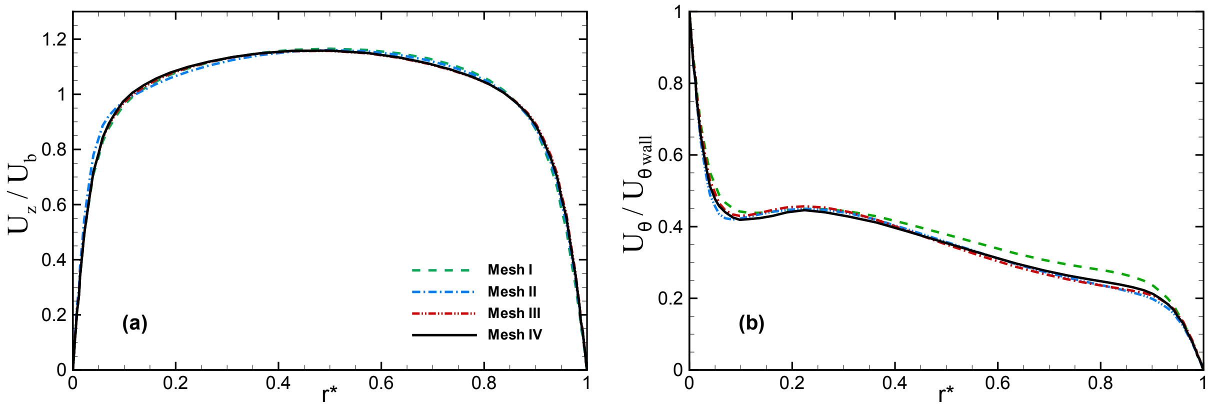

Source: Own elaboration.

There is no significant difference between the analyzed meshes for the mean axial velocity profiles (Figure. 5.4a). For the mean azimuthal velocity profiles (Figure 5.4b), results from meshes II, III, and IV are similar, while mesh I show a discrepancy between the region $0.2 < r^* < 0.97$.

The RMS velocity fluctuations and Reynolds $u_z'\ u_r'$ shear stress components predicted with different grid resolutions are plotted in Figure 5.5. Results for the second-order quantities obtained with meshes III and IV are in close agreement. The major difference between meshes III and IV in axial, radial and azimuthal turbulence intensities are 3,9%, 3.25%, and 4.7%, respectively. Conversely, profiles obtained with the grid resolutions I and II deviate significantly compared with denser grids for all second-order statistics.

Additionally, Figure 5.6 shows the ratio of the SGS viscosity to molecular viscosity, ν_{SGS}/ν. As introduced in the Section 2.6, the ratio of the SGS viscosity to molecular viscosity represents the degree of modeling in an LES simulation. According to Durbin and Pettersson-Reif (2015), when the ratio ν_{SGS}/ν is smaller than 10 %, LES is found to be accurate. Although meshes II, III and IV present values lower than 0.1 for the entire computational domain, only meshes III and IV follow the guidelines of a high-resolution grid and show similar results for the second-order statistics of the velocity field as illustrated in Figure 5.5.

Based on the grid convergence study, mesh III presents a compromise between accuracy and computational cost and, therefore, all computational results hereafter were obtained with mesh III.

Figure 5.5 – Profiles of RMS velocity fluctuations in (a) axial, (b) radial, and (c) azimuthal direction, and (d) Reynolds $u'_z u'_r$ shear stress component predicted with different mesh resolutions.

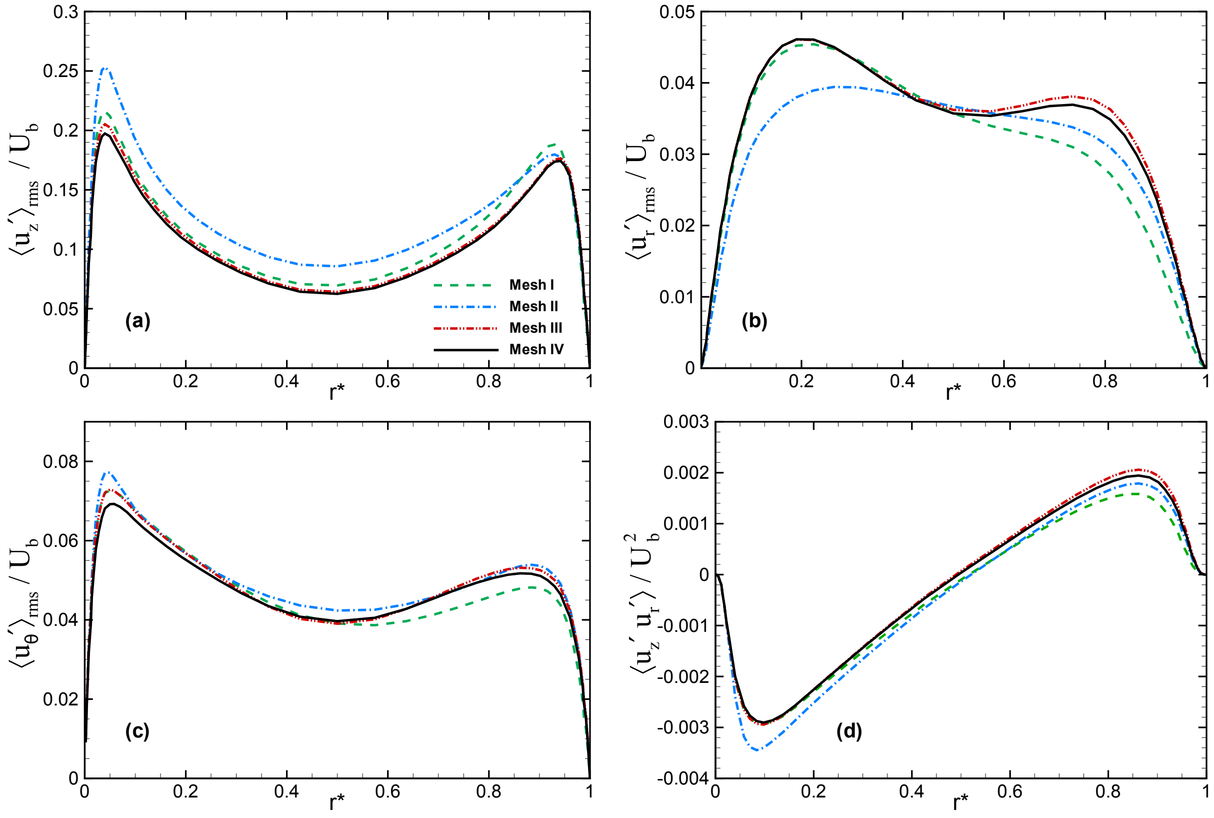

Source: Own elaboration.

Figure 5.6 – Ratio of the SGS viscosity to molecular viscosity computed for diferent grid resolutions.

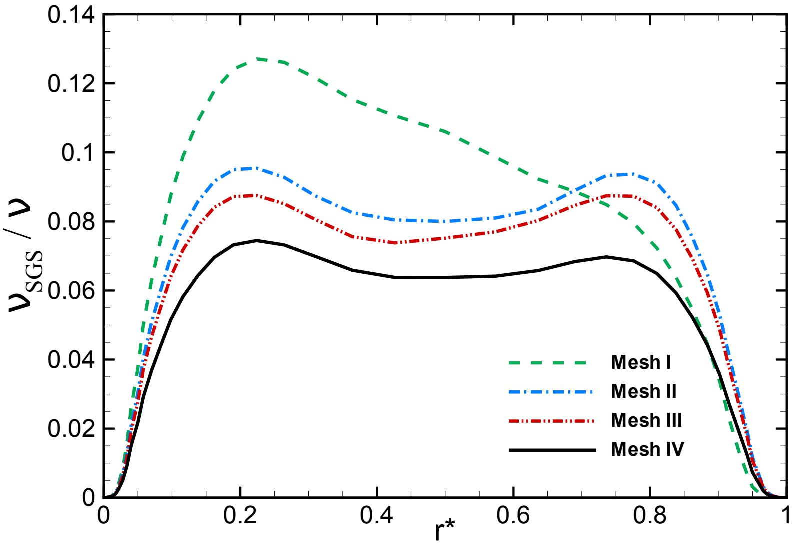

Source: Own elaboration.

5.5 Effect of Flow Behavior Index

The effect of *n* on the flow quantities is investigated with two distinct flow configurations. The cases explored in this section are summarized in Table 5.5. Case A reports the effect of flow behavior index at fixed $B_n = 0.10$ and Rotation number $N = 0.15$, and case B refers to the simulations performed at $B_n = 0.25$ with $N = 0.30$.

Table 5.5 – Set of simulations for investigating the effect of the flow behavior index on the flow quantities

	Sim	Bingham number (B_n)	Flow behavior index (n)	Rotation number (N)	Bulk Velocity [$m\ s^{-1}$]
Case A	01	0.10	0.75	0.15	1.93
	02	0.10	0.70	0.15	1.93
	03	0.10	0.65	0.15	1.93
Case B	10	0.25	0.75	0.30	1.93
	11	0.25	0.70	0.30	1.93
	12	0.25	0.65	0.30	1.93

Source: Own elaboration.

5.5.1 Instantaneous Flow

As the first step, the effect of n on instantaneous flow structures is analyzed. Figure 5.7 depicts the example of an axial-azimuthal plane used to extract the contours of the instantaneous flow. In this subsection, only the values of $n = 0.75$ and 0.65 will be considered to facilitate the flow visualization.

Figure 5.7 – Example of an axial-azimuthal plane used to extract the instantaneous velocity and viscosity contours. Contours of instantaneous axial velocity at the core region $y^+ \approx 150$ for Sim 01. The values ranging from $1U_b$ to $1.35U_b$. Red color stands for maximum values, and blue for the minimum.

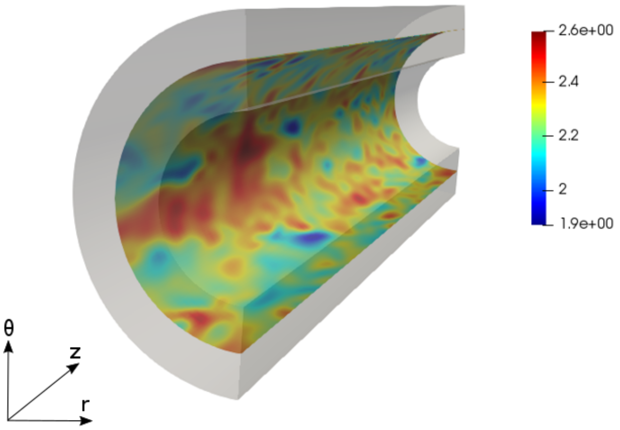

Source: Own elaboration.

Figure 5.8 shows the contours of instantaneous axial velocity; the $z - \theta$ plane is located near the outer wall at $y^+ \approx 15$, where the highest velocity fluctuations are expected. Even using the same bulk velocity, reducing the n value elongates the low-speed streaks (dark blue shades) and reduces the fluctuations in the flow. According to Singh et al. (2017a), the longer low-speed streaks for lower n are associated with reduced wall-normal turbulence intensities by shear-thinning.

Figure 5.8 – Contours of instantaneous axial velocity at $y^+ \approx 15$ from the outer wall (a) case A ($n = 0.75$ and 0.65 at $B_n = 0.10$ and $N = 0.15$); (b) case B ($n = 0.75$ and 0.65 at $B_n = 0.25$ and $N = 0.30$). The values ranging from $0.34U_b$ to $1.29U_b$. Red color stands for maximum values, and blue for the minimum. Top: flow behavior index $n = 0.75$; bottom: flow behavior index $n = 0.65$.

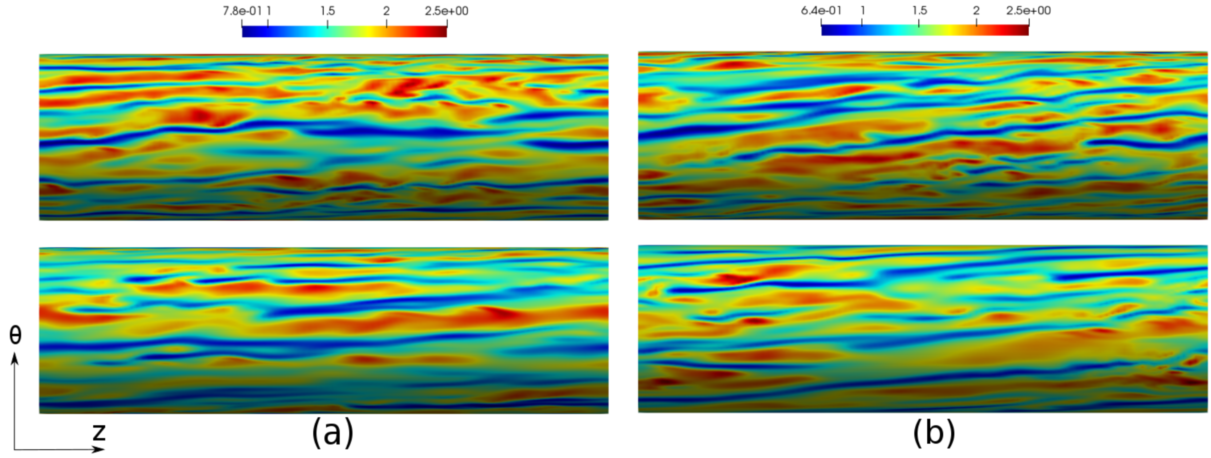

Source: Own elaboration.

Contours of instantaneous viscosity are plotted in Figure 5.9; the $z - \theta$ plane is located near the middle of the annular section at $y^+ \approx 100$ from the outer wall where the influence of n is more evident and will be discussed later in section 5.5.2, and the highest viscosity values are expected. The most significant values for viscosity fluctuations compared to the wall viscosity are found in fluids with more shear-thinning behavior, indicating a more viscous flow. The differences between the maximum viscosity fluctuations are approximately 1.6 and 1.9 times for cases A and B, respectively.

The vortical structure is visualized through the Q-criterion method. The Q-criterion can be determined as (JEONG; HUSSAIN, 1995)

$$Q = \frac{1}{2}(||\mathbf{\Omega}||^2 - ||\mathbf{S}||^2) \tag{5.3}$$

where $Q > 0$ depicts the existence of a vortex, $\mathbf{S}$ is the rate-of-strain tensor and $\mathbf{\Omega}$ is the vorticity tensor. Essentially, this parameter means that a vortex is a region where the vorticity tensor prevails over the rate-of-strain tensor.

Figure 5.10 exhibits the iso-surfaces of the Q-criterion for both cases. It can be noticed that the vortices regions decrease for fluids with higher shear-thinning behavior (lower n value). This phenomenon may be associated with the growth in flow viscosity that, as a consequence, generates weaker turbulence structures. A projection of case A in 3D perspective is illustrated in Figure 5.11.

Figure 5.9 – Contours of instantaneous viscosity at $y^+ \approx 100$ from the outer wall (a) case A ($n = 0.75$ and 0.65 at $B_n = 0.10$ and $N = 0.154$) ranging from $1\nu_{wall}$ to 7.2 ν_{wall}; (b) case B ($n = 0.75$ and 0.65 at $B_n = 0.25$ and $N = 0.30$) ranging from $1\nu_{wall}$ to 9.7 ν_{wall}. Red color stands for maximum values, and dark blue for the minimum. Top: flow behavior index $n = 0.75$; bottom: flow behavior index $n = 0.65$.

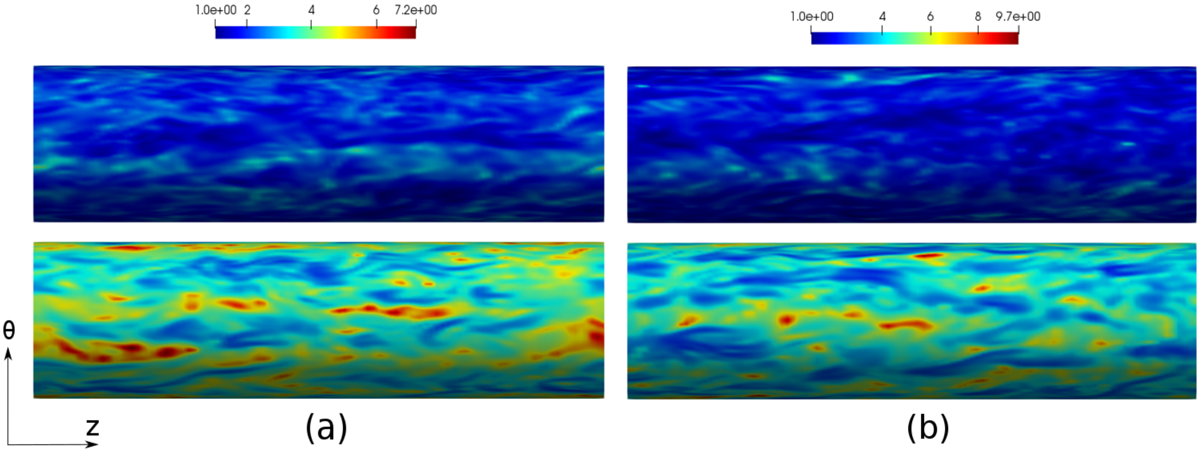

Source: Own elaboration.

From Figures 5.10 and 5.11 can also be observed that for flows with $n = 0.75$ the vortices are more uniformly distributed throughout the domain than $n = 0.65$. For flow behavior index $n = 0.65$, the vortices are concentrated near the inner cylinder, where the highest velocity gradients and the lowest viscosity values of the annular region are located. In the present work, the values of $Q = 750$ represent 10% of the range of the Q-criterion, as lower values of Q result in an excessive amount of structures that make visualization difficult.

Figure 5.10 – Top view of the iso-surfaces of the Q-criterion ($Q = 750$) colored by the instantaneous axial velocity. The $Q = 750$ represents the value of 10% of the Q-criterion range. (a) Case A ($n = 0.75$ and 0.65 at $B_n = 0.10$ and $N = 0.154$); (b) case B ($n = 0.75$ and 0.65 at $B_n = 0.25$ and $N = 0.30$) ranging from $1\nu_{wall}$ to 9.8 ν_{wall}. Red color stands for maximum values, and blue for the minimum. Top: flow behavior index $n = 0.75$; bottom: flow behavior index $n = 0.65$.

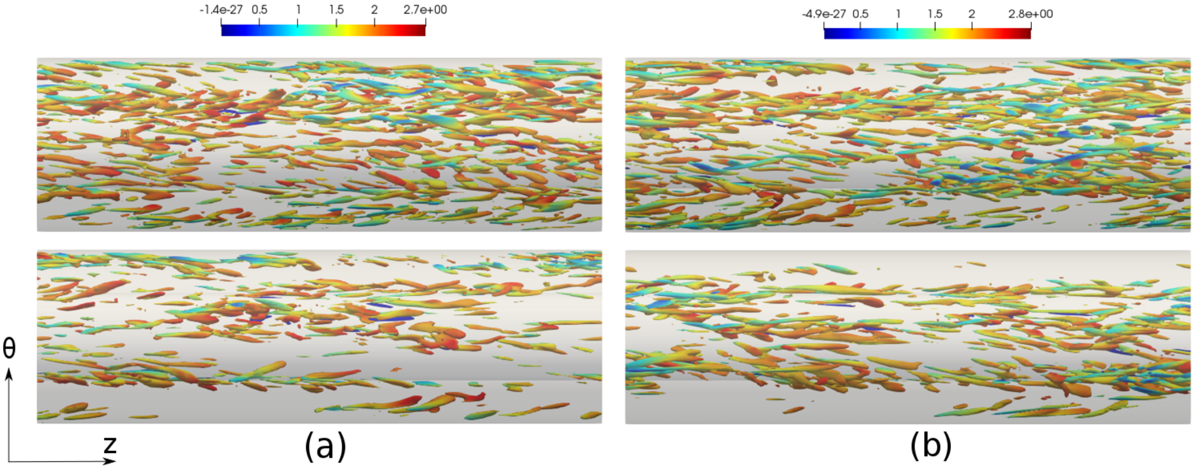

Source: Own elaboration.

Figure 5.11 – Iso-surfaces of the Q-criterion ($Q = 750$) colored by instantaneous axial velocity for case A: (a) flow behavior index $n = 0.75$; (b) flow behavior index $n = 0.65$.

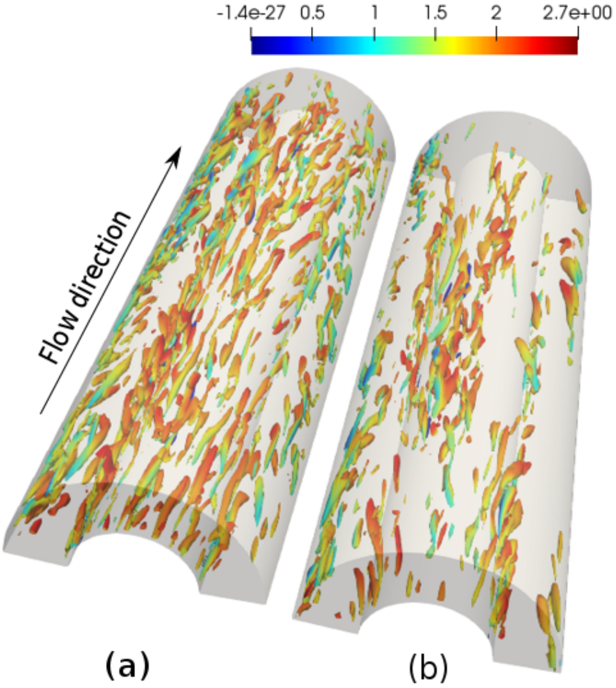

Source: Own elaboration.

5.5.2 Mean Flow Quantities

Distributions of mean axial and azimuthal velocity components for cases A and B are shown in Figure 5.12. The mean axial velocity profiles normalized by U_b did not show disparities for different n. For the present work, it is noted that the velocity profiles obtained for the annular region via numerical simulation are symmetric for this range of Reynolds number. It is worth mentioning that the asymmetries were observed experimentally by several authors and during the transition regime in pipe flow. The mean azimuthal velocity profiles present a high-velocity gradient close to the walls due to the boundary conditions applied in these regions. In the middle of the gap, between the region $0.2 < r^* < 0.85$, the mean angular momentum decreases almost linearly.

The influence of flow behavior index *n* on the mean axial velocity is more evident in the logarithmic velocity profile plotted as a function of the distance from the wall y^+. These profiles are illustrated in Figure 5.13. The law of the wall proposed by Anbarlooei et al. (2015) for both power-law and Herschel-Bulkley fluids are plotted for comparison. The authors argue that the proposed law of the wall fits better than the “Newtonian” law of the wall.

From Figure 5.13, the effect of n on the mean axial velocity becomes visible for $y^+ > 10$. As the flow behavior index *n* decreases, the higher the shear-thinning characteristic, the slope of the mean axial velocity profiles enhances. This behavior suggests that the flow with $n = 0.65$ is more transitional. Similar trends have been noticed in turbulent pipe flows of Power-law fluids in Rudman et al. (2004), Singh et al. (2017a), and Gavrilov and Rudyak (2016).

Figure 5.12 – Profiles of the mean (a) axial and (b) azimuthal velocity. The bulk velocity normalizes the mean axial velocity, and the mean azimuthal velocity is normalized by the rotational velocity of the inner wall. Left: case A ($n = 0.75$,0.70 and 0.65 at $B_n = 0.10$ and $N = 0.15$); right: case B ($n = 0.75$,0.70 and 0.65 at $B_n = 0.25$ and $N = 0.30$).

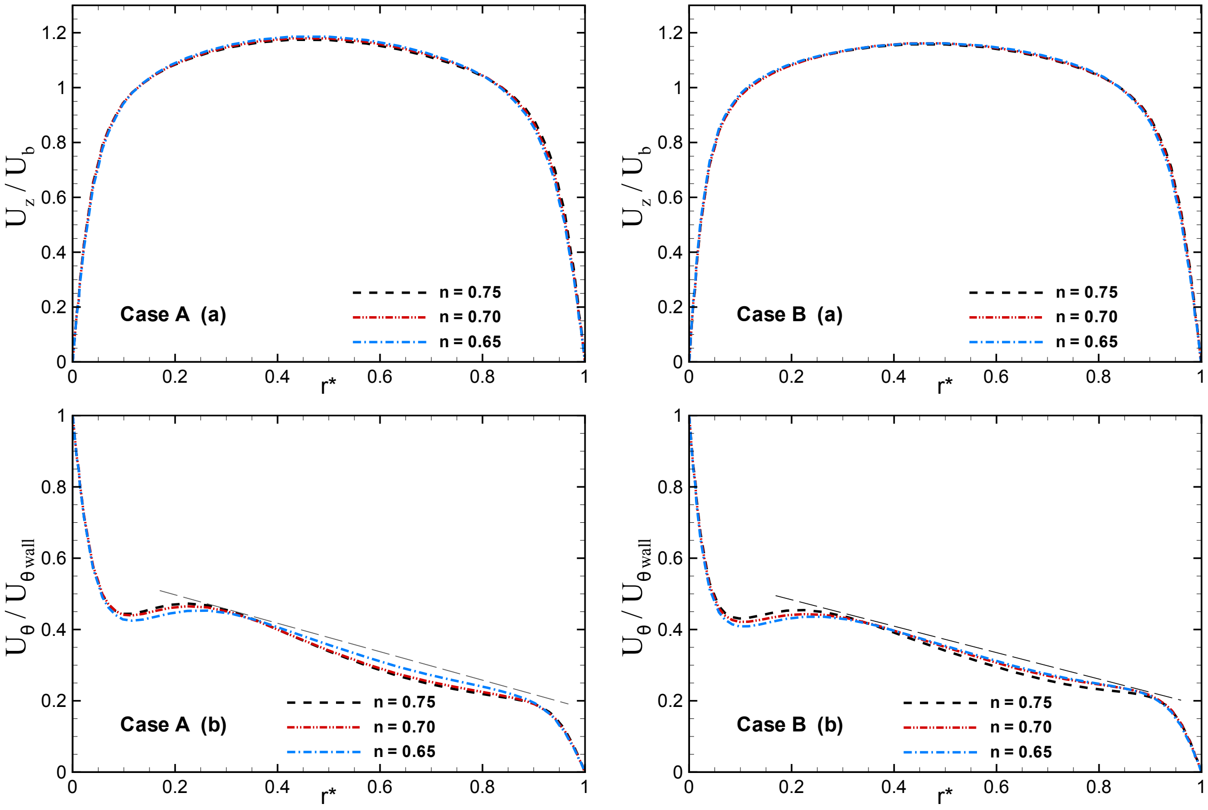

Source: Own elaboration.

The difference observed in the logarithm region, $y^+ > 30$, near the inner and outer walls (Figures 5.13a and 5.13b) is attributed to the rotation effect of the inner cylinder, which increases the friction velocity. The mean axial velocity profiles in the logarithm region near the outer wall are located above the logarithmic law of the wall, while profiles close to the inner wall lie in the same region or below the logarithmic law of the wall. This behavior is consistent with profiles observed by Chung and Sung (2005) and Schneider et al. (2017).

Profiles of the mean viscosity normalized by the wall viscosity ν_{wall} are shown in Figure 5.14 for both analyzed cases in this section. From the figures illustrated in wall coordinates (Figures 5.14b and 5.14c), it can be noted that near the walls, the mean viscosity profiles are constant up to $y^+ \approx 5$. The effect of flow behavior index n becomes apparent after $y^+ \geq 10$, the mean viscosity increases towards the center of the annular section. Shear-thinning fluids exhibit a dependence of the apparent viscosity on shear rate, whose viscosity decreases as the shear rate enhances, indicating that the regions close to the walls have the highest shear rate values. In addition, the ratio between the maximum value (at the center of the annular section) and the minimum value (near the wall) of the normalized mean viscosity increases for higher shear-thinning fluids.

Figure 5.13 – Profiles of the mean axial velocity plotted in wall units, (a) near the inner wall; (b) near the outer wall. Left: case A ($n = 0.75$, 0.70 and 0.65 at $B_n = 0.10$ and $N = 0.15$); right: case B ($n = 0.75$, 0.70 and 0.65 at $B_n = 0.25$ and $N = 0.30$).

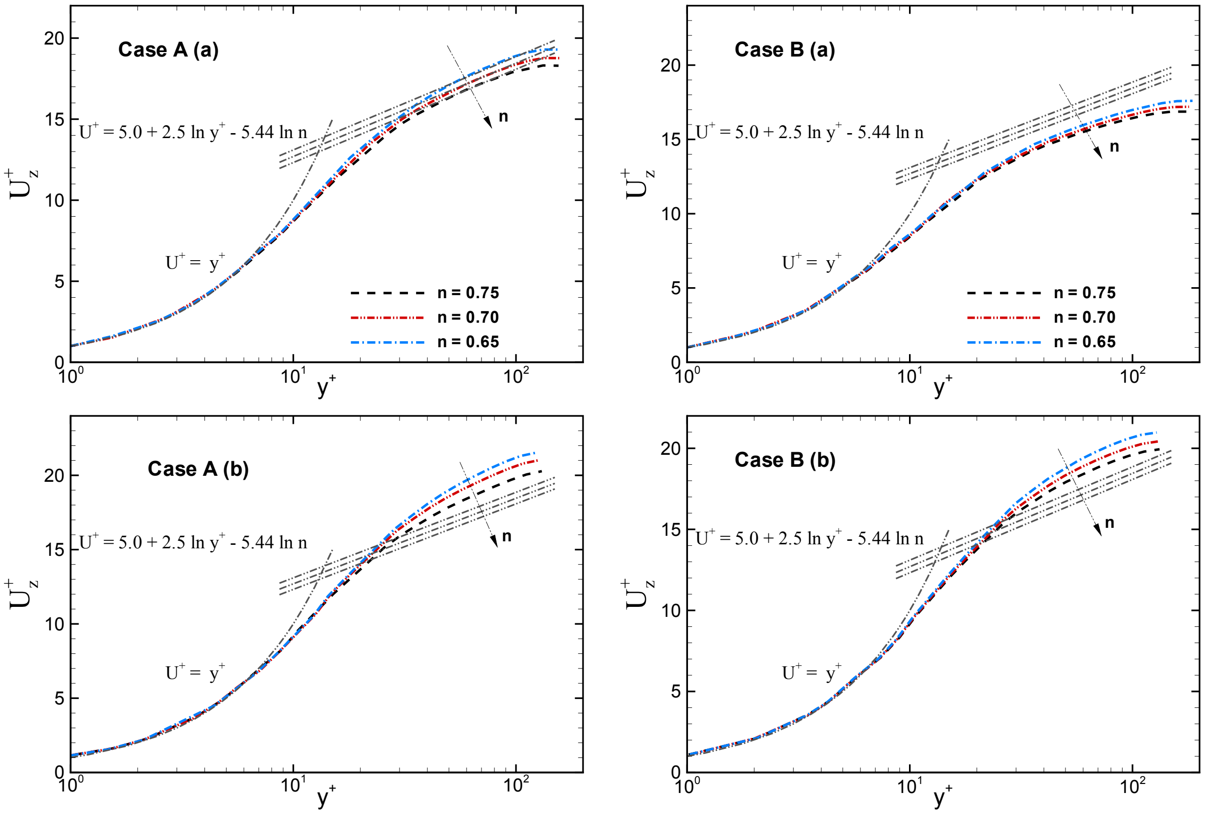

Source: Own elaboration.

The RMS velocity fluctuations plotted in wall units for cases A and B are illustrated in Figures 5.15 and 5.16, respectively, and these properties normalized by the bulk velocity are reported in Figure 5.17. From Figures 5.15 and 5.16, it can be observed that by reducing the fluid behavior index *n*, the RMS axial velocity fluctuations are enhanced. Conversely, the RMS velocity fluctuations in the radial and azimuthal directions decreased. Singh et al. (2017a) suggest that this behavior for shear-thinning fluids is due to the strong dependence of u_r^+ and u_θ^+ on the mean fluid viscosity. The increase in viscosity with reducing n (see Figure 5.14) dampens the velocity fluctuations normal to the wall. Gavrilov and Rudyak (2017) also argue that the increase in turbulent anisotropy is due to the reduced energy transport from the axial to the transverse fluctuations due to the increase in viscosity as a function of distance from the wall. As a result, this behaviour leads to an enhancement of the axial velocity fluctuations and an attenuation of the fluctuations of the radial and azimuthal components.

Figure 5.14 – Profiles of the normalized mean viscosity ν/ν_{wall}. (a) Plotted as a function of r^*, (b) Plotted as a function of y^+, near the inner wall; (c) Plotted as a function of y^+, near the outer wall. Left: case A ($n = 0.75$, 0.70 and 0.65 at $B_n = 0.10$ and $N = 0.15$); right: case B ($n = 0.75$, 0.70 and 0.65 at $B_n = 0.25$ and $N = 0.30$).

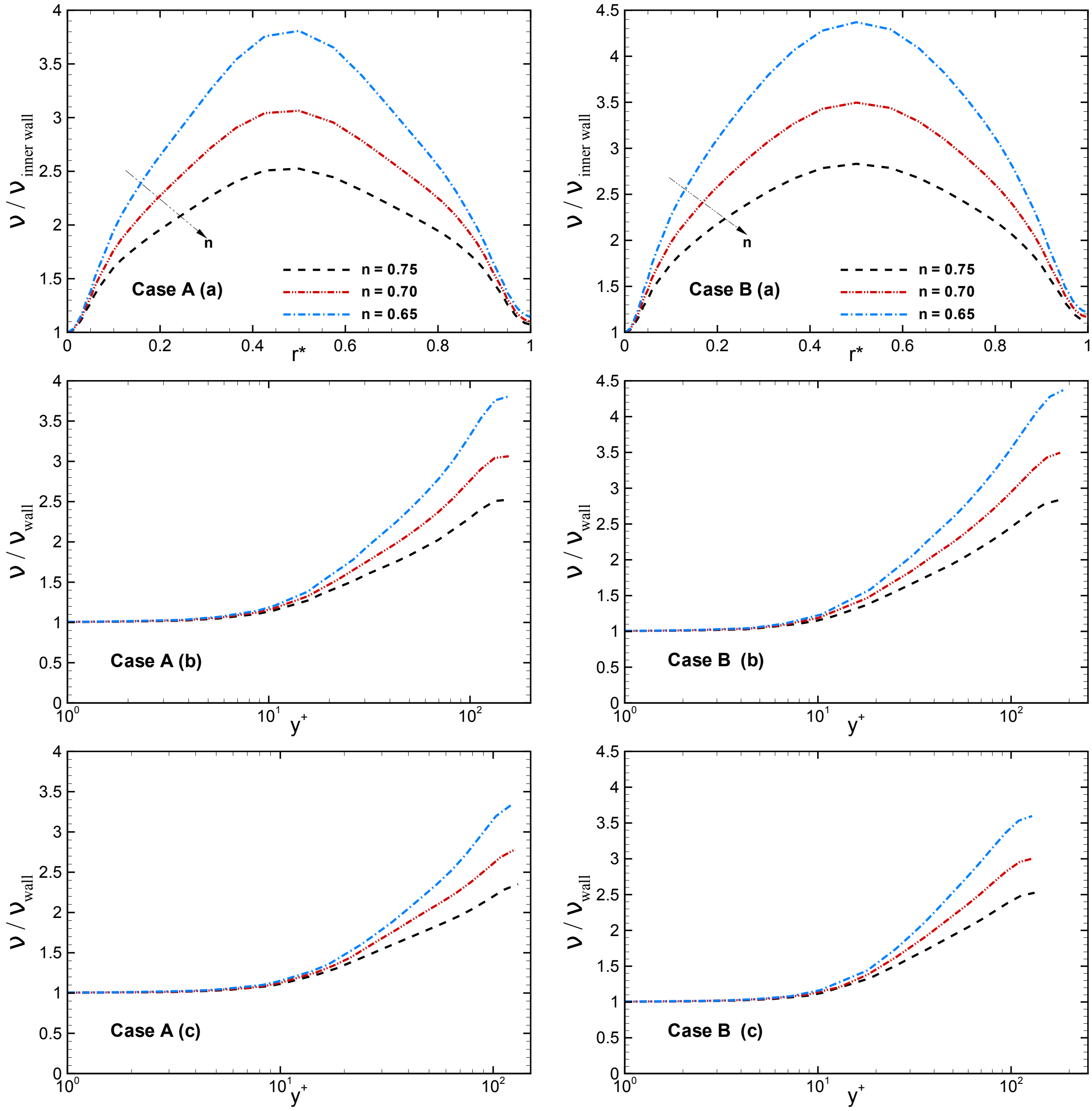

Source: Own elaboration.

Profiles of RMS velocity fluctuations normalized by the bulk velocity illustrated in Figure 5.17 show similar trends to the RMS velocity fluctuations plotted in wall units, Figures 5.15 and 5.16. However, asymmetries in the RMS velocity fluctuation profiles become evident due to the increase in the rotation of the inner cylinder for $N = 0.30$.

Figure 5.15 – Profiles of RMS velocity fluctuations plotted in wall units for case A ($n = 0.75$, 0.70 and 0.65 at $B_n = 0.10$ and $N = 0.15$), (a) axial, (b) radial, and (c) azimuthal direction. Left: near the inner wall; right: near the outer wall.

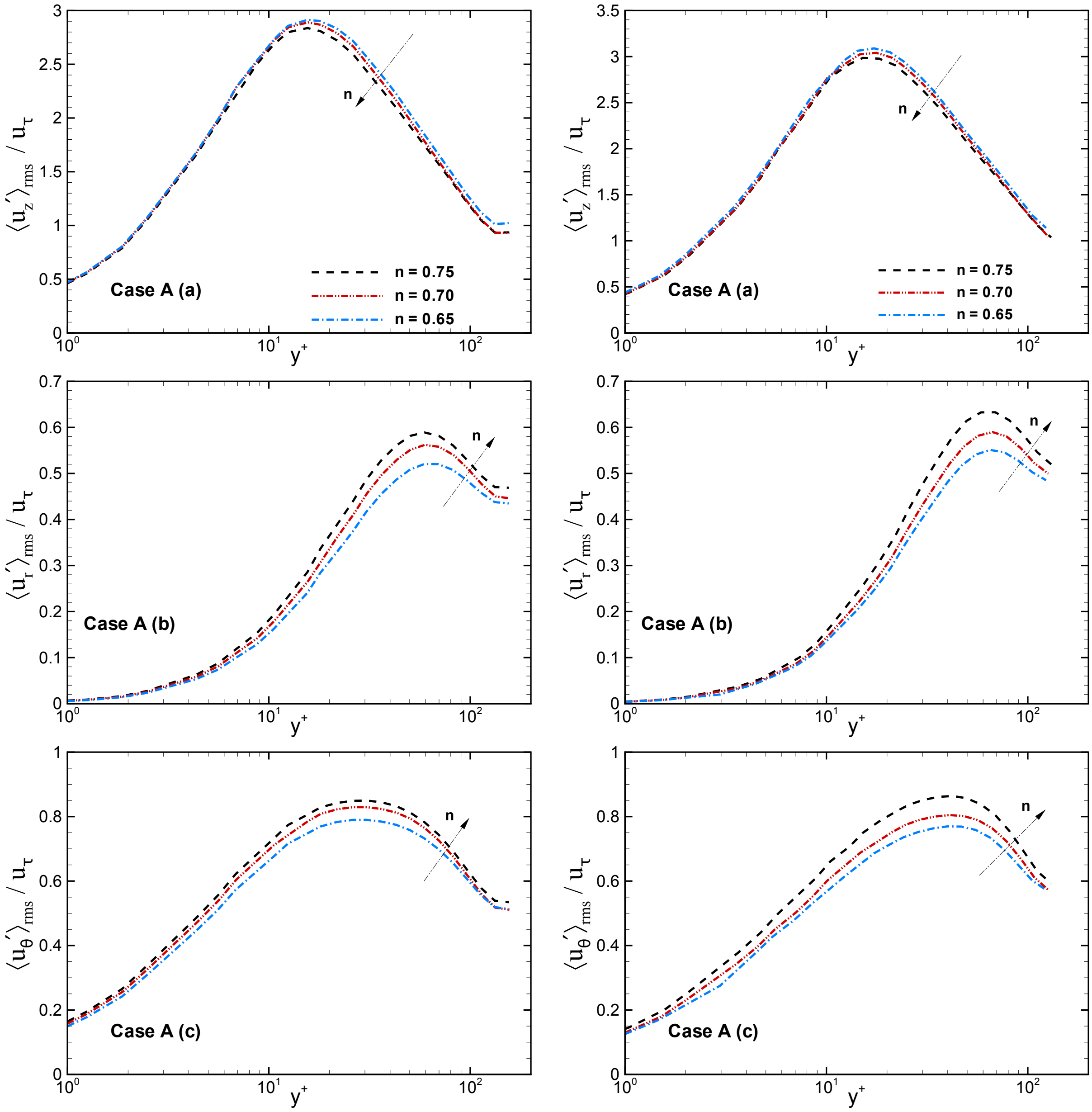

Source: Own elaboration.

The Reynolds shear stress is shown in Figure 5.18. The effect of n on these quantities is comparable to the RMS velocity fluctuations in the radial and azimuthal directions. The Reynolds shear stress components reduce with increasing shear-thinning behavior. The Reynolds $r\theta$ stress component (Figure 5.18b) is zero in non-rotating annular. The higher values of this term near the inner wall than the outer wall are attributed to the more active turbulence events in that region. According to Liu and Lu (2005), the annular section rotation enhances the correlation between the radial velocity fluctuation generated by the near-wall turbulence events (coherent turbulent structures) and the azimuthal velocity fluctuation in the wall regions.

Figure 5.16 – Profiles of RMS velocity fluctuations plotted in wall units for case B ($n = 0.75$, 0.70 and 0.65 at $B_n = 0.25$ and $N = 0.30$), (a) axial, (b) radial, and (c) azimuthal direction. Left: near the inner wall; right: near the outer wall.

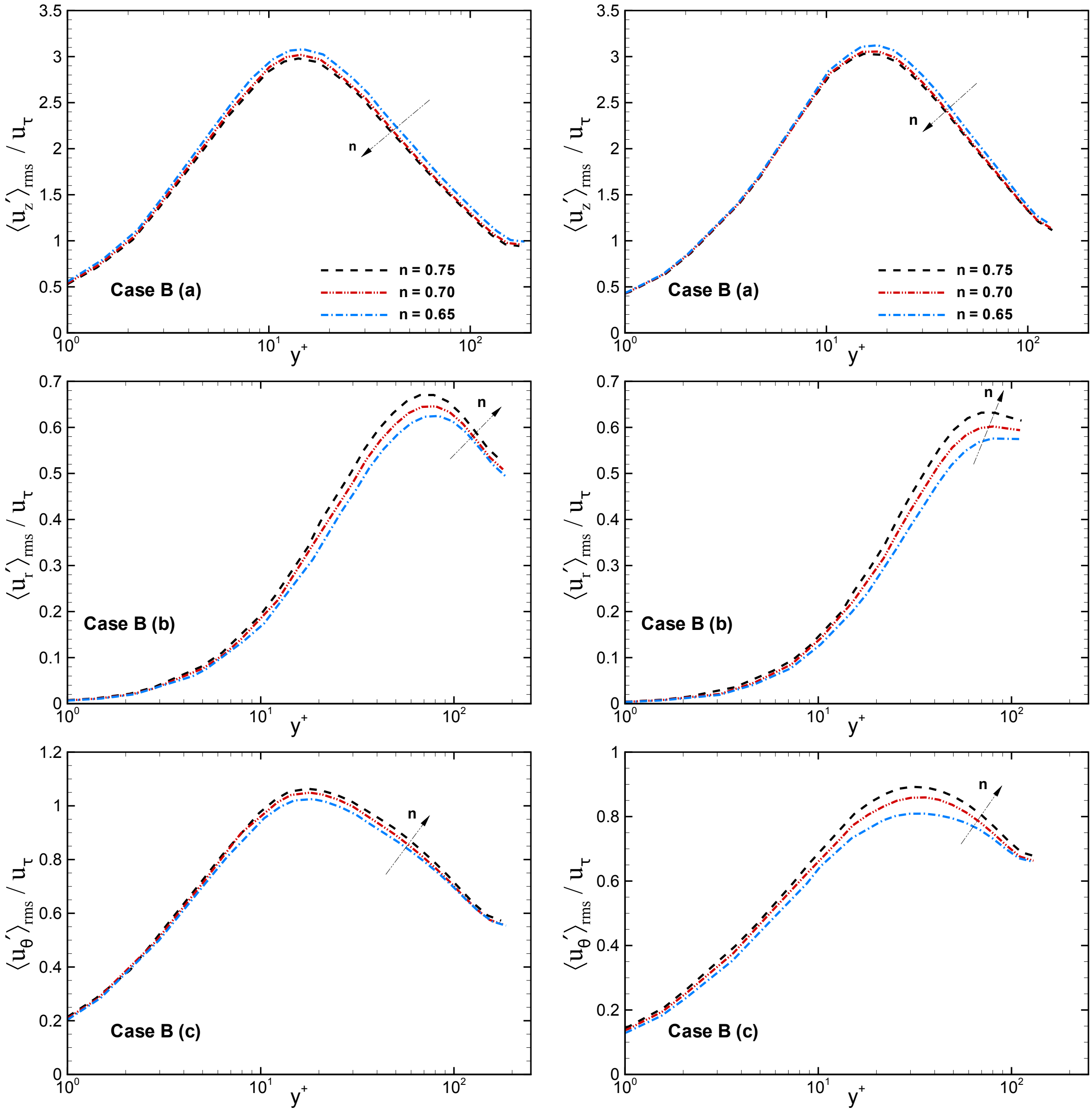

Source: Own elaboration.

Distributions of mean turbulence kinetic energy (TKE) per unit mass $k = \frac{1}{2} \sum_i \overline{u_i' u_i'}$ are reported in Figure 5.19. The mean TKE presents the peak values near the inner and outer walls, located in wall units by around $y^+ \approx 16$. From the profiles normalized by ${U_b}^2$ (Figure 5.19a), the TKE distributions deviate slightly. However, the fluid with the higher n has the highest peak values. On the contrary, when the TKE profiles are plotted in wall coordinates using the respective friction velocity values for the inner and outer walls (Figures 5.19b and 5.19c), the TKE profiles follow the pattern RMS axial velocity fluctuations. By reducing the fluid behavior index n, the TKE enhances.

Figure 5.17 – Profiles of RMS velocity fluctuations normalized by the bulk velocity U_b, (a) axial, (b) radial, and (c) azimuthal direction. Left: case A ($n = 0.75$, 0.70 and 0.65 at $B_n = 0.10$ and $N = 0.15$); right: case B ($n = 0.75$, 0.70 and 0.65 at $B_n = 0.25$ and $N = 0.30$).

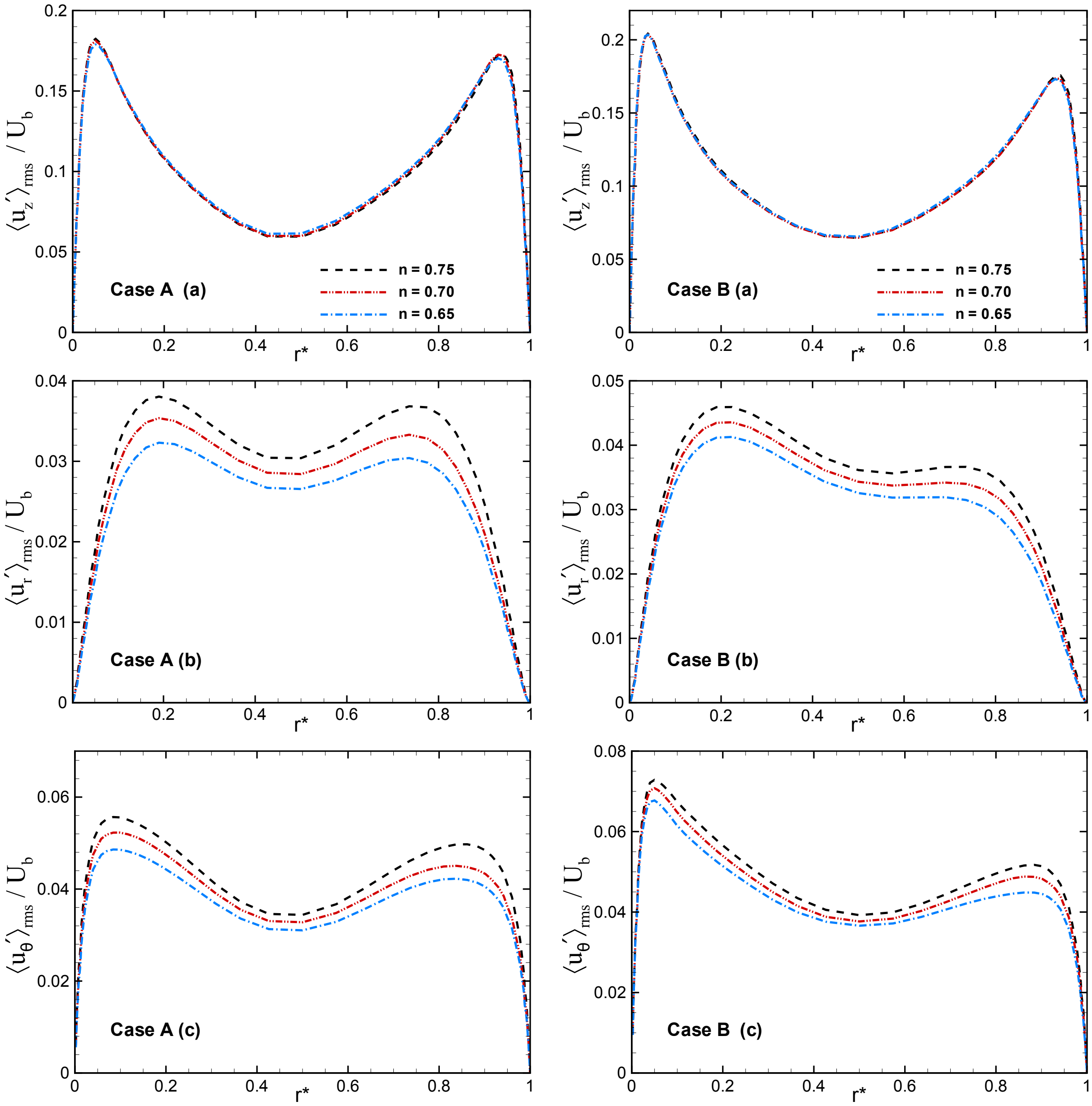

Source: Own elaboration.

The similarity between the profiles of TKE and axial turbulent intensity occurs as the contribution of the streamwise turbulent intensity to the TKE is always more significant than the contribution of the other two normal components (PONCET et al., 2014). While axial turbulence fluctuation is generated by mean flow shear, the radial and azimuthal turbulence fluctuations are yielded by the sweep and ejection events related to the high- and low-speed elongated streaks in the near-wall regions (LIU; LU, 2005).

Figure 5.18 – Profiles of Reynolds shear stress normalized by U_b^2, (a) Reynolds rz stress component and (b) Reynolds $r\theta$ stress component. Left: case A ($n = 0.75$, 0.70 and 0.65 at $B_n = 0.10$ and $N = 0.15$); right: case B ($n = 0.75$, 0.70 and 0.65 at $B_n = 0.25$ and $N = 0.30$).

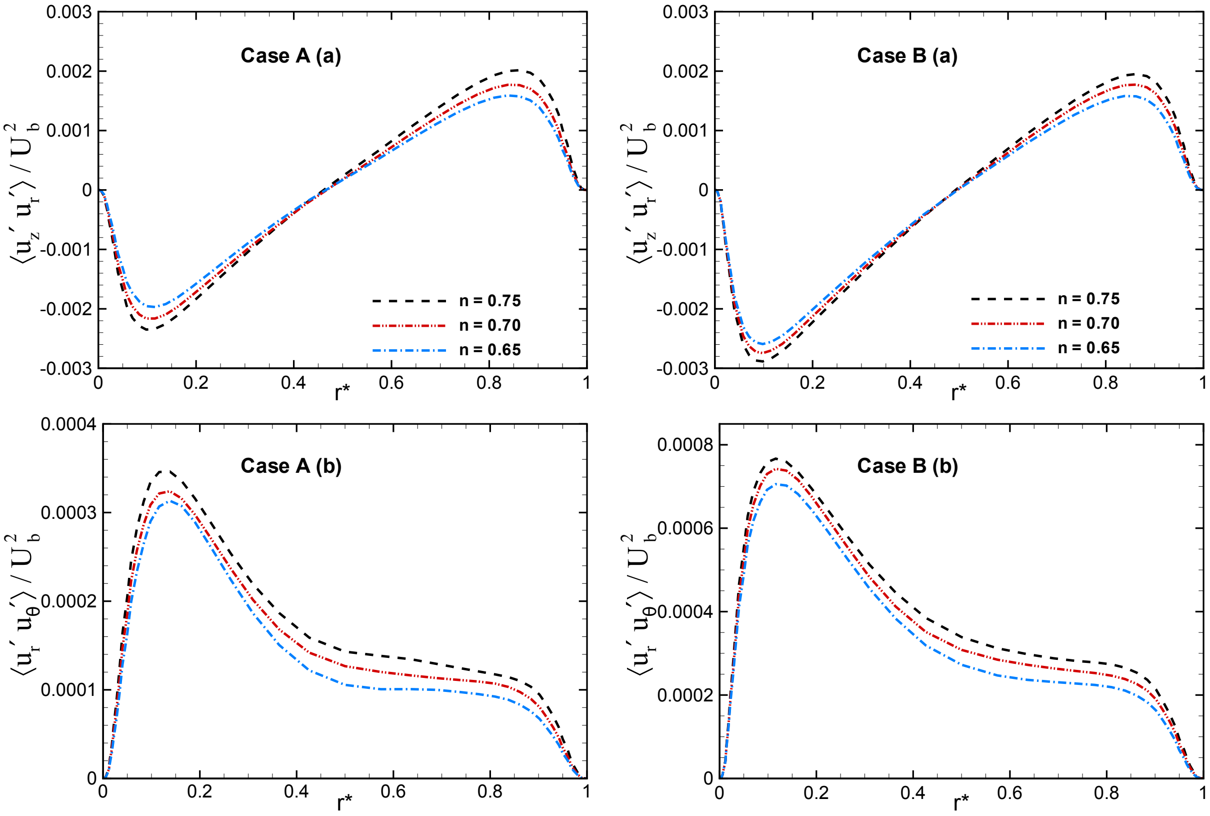

Source: Own elaboration.

The influence of the flow behavior index n on the pressure gradient and skin friction coefficients are given in Table 5.6 and Table 5.7, respectively. The mean axial pressure gradient for an annular section can be determined as (BAGUERI et al., 2020)

$$\Psi = \frac{2(\tau_{w,i}\, R_i + \tau_{w,o}\, R_o)}{R_o^2 - R_i^2} \tag{5.4}$$

where $\tau_{w,i}$ and $\tau_{w,o}$ are the mean wall shear stress on the inner and outer cylinders, respectively. The values of $\tau_{w,i}$ and $\tau_{w,o}$ are different due to the rotation and curvature effects of the inner and outer cylinders. The skin friction coefficient, $f = \tau_w/(\rho {U_b}^2/2)$, was already introduced in the previous chapter (Eq.4.3).

Figure 5.19 – Profiles of turbulence kinetic energy. (a) Plotted as a function of $r*$ and normalized by U_b^2; (b) Plotted as a function of y^+ and normalized by u_τ^2, near the inner wall; (c) Plotted as a function of y^+ and normalized by u_τ^2, near the outer wall. Left: case A ($n = 0.75, 0.70$ and 0.65 at $B_n = 0.10$ and $N = 0.15$); right: case B ($n = 0.75, 0.70$ and 0.65 at $B_n = 0.25$ and $N = 0.30$).

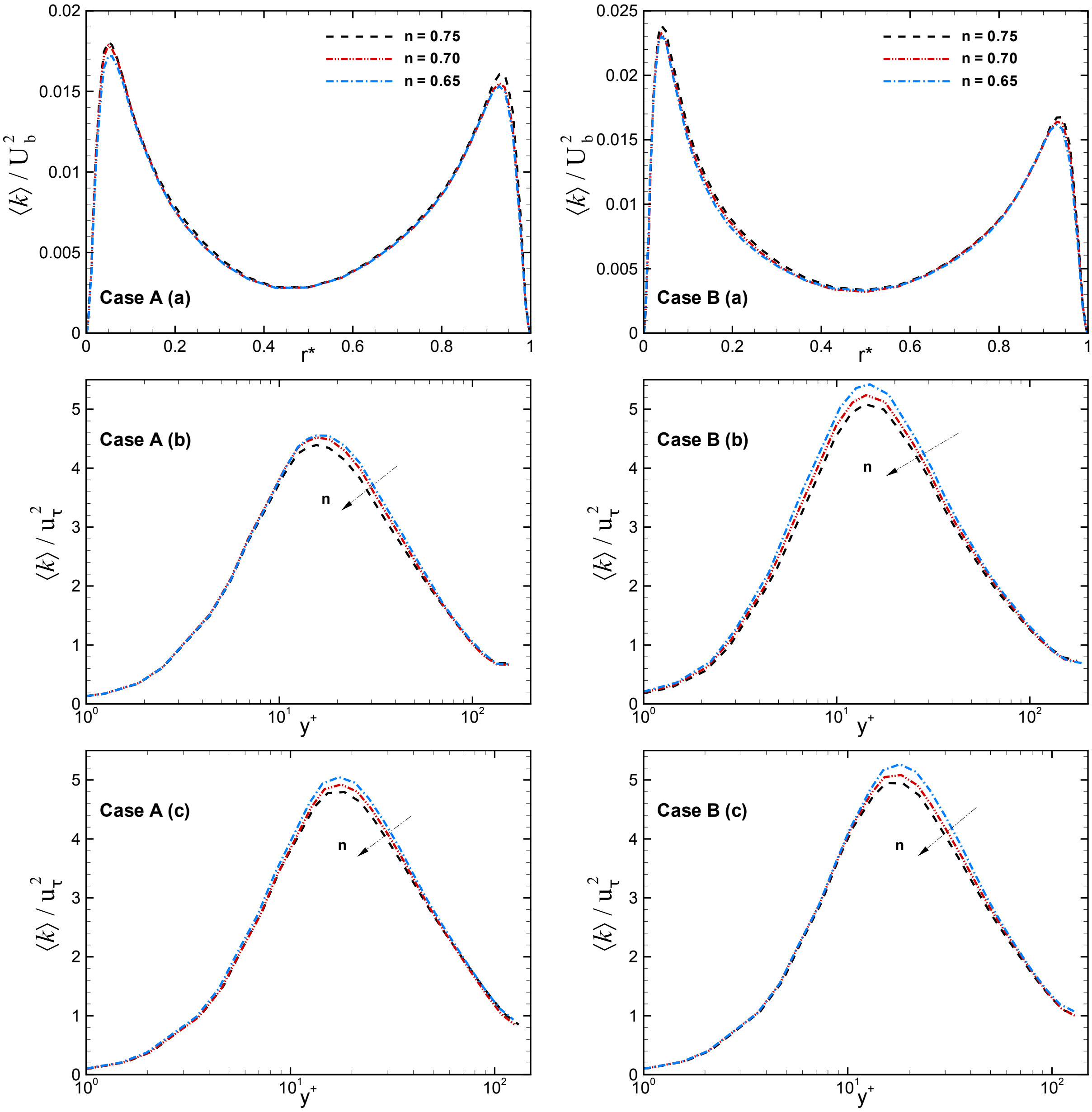

Source: Own elaboration.

These two quantities – pressure gradient and the skin friction coefficients – depend on the τ_w. As can be noticed, by reducing n, the values of these quantities fall. This behavior is related to the reduction of wall-normal turbulence intensities, as shown in Figure 5.17, which generate weaker turbulent structures and smaller amounts of high-speed fluid near the wall regions where wall shear stress is produced (RUDMAN; BLACKBURN, 2006).

Table 5.6 – Pressure gradient computed for different flow behavior indices *n*.

	Sim	Bingham number (B_n)	Flow behavior index (n)	Rotation number (N)	Pressure gradient [$Pa\, m^{-1}$]
Case A	01	0.10	0.75	0.15	537.1
	02	0.10	0.70	0.15	509.1
	03	0.10	0.65	0.15	488.8
Case B	10	0.25	0.75	0.30	568.3
	11	0.25	0.70	0.30	549.2
	12	0.25	0.65	0.30	522.9

Source: Own elaboration.

Table 5.7 – Skin friction coefficients estimated for different flow behavior indices *n*.

	Sim	Bingham number (B_n)	Flow behavior index (n)	Rotation number (N)	$f_{inner\ wall}$ x10^{-3}	$f_{outer\ wall}$ x10^{-3}
Case A	01	0.10	0.75	0.15	8.23	6.70
	02	0.10	0.70	0.15	7.90	6.30
	03	0.10	0.65	0.15	7.55	6.07
Case B	10	0.25	0.75	0.30	9.35	6.77
	11	0.25	0.70	0.30	9.07	6.52
	12	0.25	0.65	0.30	8.78	6.14

Source: Own elaboration.

5.6 Effect of the Bingham Number

This section evaluates the effect of the Bingham number B_n on the flow quantities. The set of simulations is reported in Table 5.8. The simulations of case C account for the flow behavior index $n = 0.65$ and $N = 0.15$, while the Bingham number varies from 0.10 to 0.45. Case D evaluates the dependence of B_n with $n = 0.75$ and $N = 0.30$. As mentioned earlier in Chapter 2, the B_n is the ratio of yield stress force to the viscous force (ALEXANDROU et al., 2003).

Table 5.8 – Set of simulations for investigating the effect of Bingham number on the flow quantities.

	Sim	Bingham number (B_n)	Flow behavior index (n)	Rotation number (N)	Bulk Velocity [$m\ s^{-1}$]
Case C	03	0.10	0.65	0.15	1.93
	05	0.25	0.65	0.15	1.93
	07	0.40	0.65	0.15	1.93
Case D	08	0.10	0.75	0.30	1.93
	10	0.25	0.75	0.30	1.93
	13	0.40	0.75	0.30	1.93

Source: Own elaboration.

5.6.1 Instantaneous Flow

Figure 5.20 shows contours of instantaneous axial velocity in a $z - \theta$ plane located at $y^+ \approx 15$ from the outer wall for $B_n = 0.10$ and 0.40. The low-speed streaks become more evident and elongated in the streamwise direction for a higher B_n number, suggesting weaker turbulent structures that bring less high-speed fluids from the central zones into the near-wall areas due to the higher viscosity in the core region compared with a flow containing a lower B_n number. This flow pattern for viscoplastic fluids was also observed by Singh et al. (2017b) and LUGARINI DE SOUZA (2020) for turbulent flows with Bingham fluids.

Figure 5.20 – Contours of instantaneous axial velocity at $y^+ \approx 15$ from the outer wall (a) case C ($B_n = 0.10$ and 0.40 at $n = 0.65$ and $N = 0.15$) ranging from $0.43U_b$ to $1.30U_b$; (b) case D ($B_n = 0.10$ and 0.40 at $n = 0.75$ and $N = 0.30$) ranging from $0.48U_b$ to $1.34U_b$. Red color stands for maximum values, and blue for the minimum. Top: Bingham number $B_n = 0.10$; bottom: Bingham number $B_n = 0.40$.

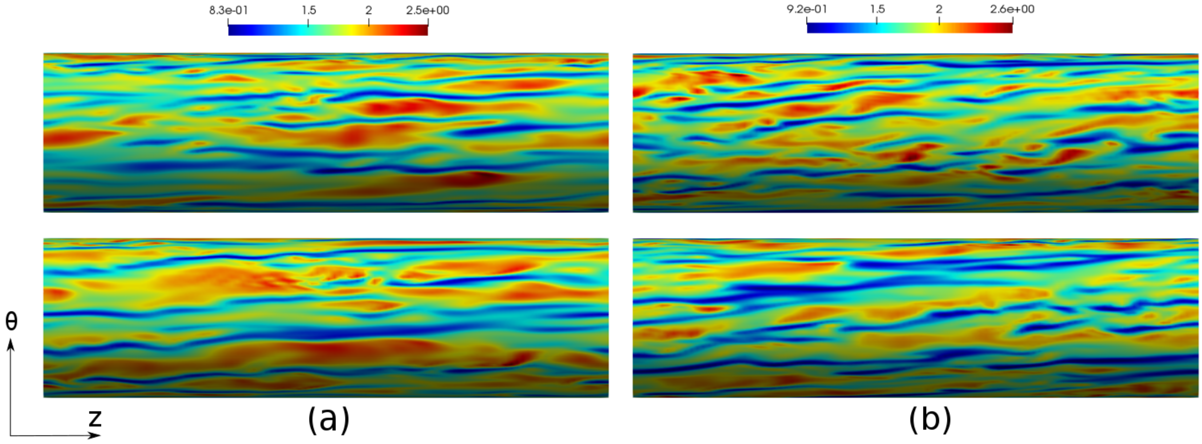

Source: Own elaboration.

Contours of instantaneous viscosity located at $y^+ \approx 100$ from the outer wall are plotted in Figure 5.21. As the number of B_n increases, the simulations show regions with higher instantaneous viscosity values. It is worth mentioning that even in the case C for $B_n = 0.40$ (Sim 07) with viscosity fluctuations on the order of 13.2 ν_{wall}, no unyielded zones ($\dot{\gamma} \to 0$ [s^{-1}]) were noticed. The lowest instantaneous and mean strain rates observed for Sim 07 have values of $\dot{\gamma} = 2.63$ [s^{-1}] and $\dot{\gamma} = 16.63$ [s^{-1}], respectively.

The vortex structures for the flows at $B_n = 0.10$ and 0.40 are shown in Figure 5.22 . For $B_n = 0.10$, there are more vortices throughout the computational domain than $B_n = 0.40$, exhibiting more developed turbulence characteristics. Combination of the small flow behavior index ($n = 0.65$) and high Bingham number ($B_n = 0.40$) is shown in Figure 5.22a. For iso-surface of $Q = 750$, the vortical structures are scarce. The flow exhibits a weak turbulent activity at the gap center due to the high viscosity coexisting with more energetic turbulent regions close to the inner wall as a consequence of the rotation effect.

Figure 5.21 – Contours of instantaneous viscosity at $y^+ \approx 100$ from the outer wall (a) case C ($B_n = 0.10$ and 0.40 at $n = 0.65$ and $N = 0.15$) ranging from $1\nu_{wall}$ to $13.5\nu_{wall}$; (b) case D ($B_n = 0.10$ and 0.40 at $n = 0.75$ and $N = 0.30$) ranging from $1\nu_{wall}$ to $6.6\nu_{wall}$. Red color stands for maximum values, and blue for the minimum. Top: Bingham number $B_n = 0.10$; bottom: Bingham number $B_n = 0.40$.

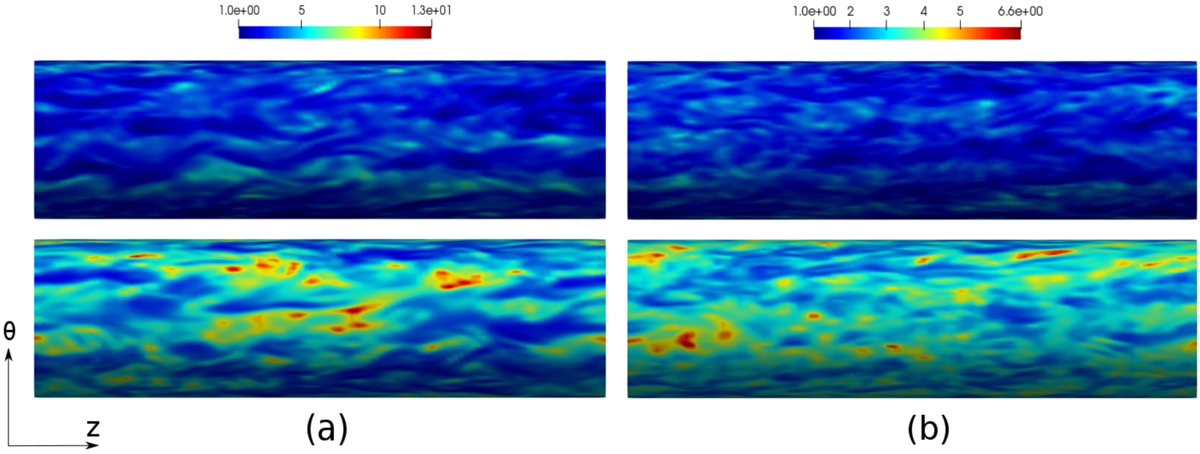

Source: Own elaboration.

Figure 5.22 – Top view of the iso-surfaces of the Q-criterion ($Q = 750$) colored by the instantaneous axial velocity (a) case C ($B_n = 0.10$ and 0.40 at $n = 0.65$ and $N = 0.15$); (b) case D ($B_n = 0.10$ and 0.40 at $n = 0.75$ and $N = 0.30$). Red color stands for maximum values, and blue for the minimum. Top: Bingham number $B_n = 0.10$; bottom: Bingham number $B_n = 0.40$.

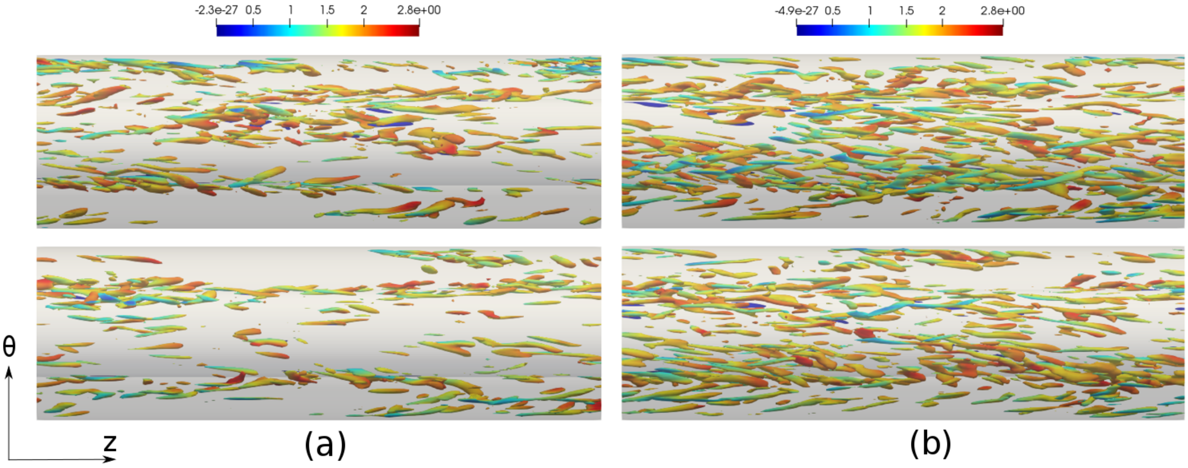

Source: Own elaboration.

5.6.2 Mean flow Quantities

Profiles of mean axial and azimuthal velocity components for cases C and D are illustrated in Figure 5.23. The bulk velocity normalizes the mean axial velocity, and the mean azimuthal velocity is normalized by the rotational velocity of the inner wall. From Figure 5.23, no significant difference was observed in the mean axial velocity. A strong velocity gradient exists near the walls in the mean azimuthal velocity profiles.

Figure 5.23 – Profiles of the mean (a) axial and (b) azimuthal velocity. The bulk velocity normalizes the mean axial velocity, and the mean azimuthal velocity is normalized by the rotational velocity of the inner wall. Left: case C ($B_n = 0.10, 0.25$ and 0.40 at $n = 0.65$ and $N = 0.15$); right: case D ($B_n = 0.10, 0.25$ and 0.40 at $n = 0.75$ and $N = 0.30$).

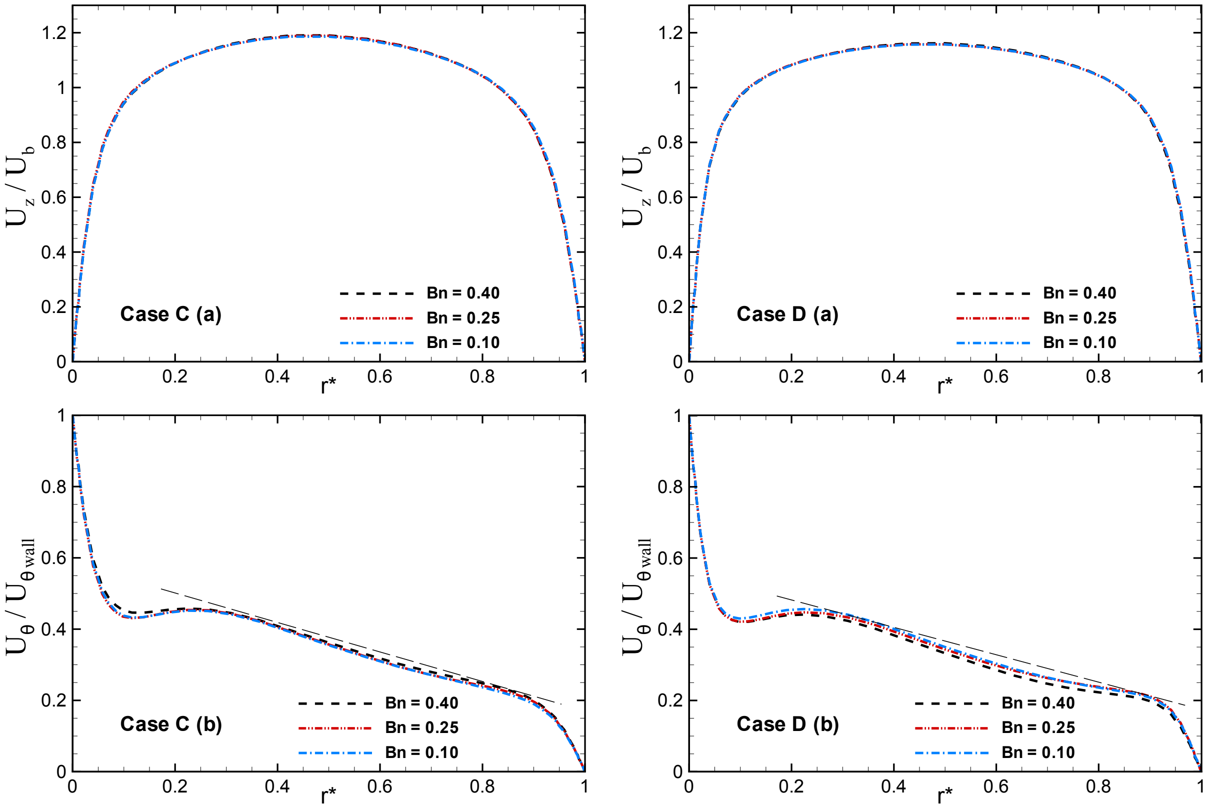

Source: Own elaboration.

The mean axial velocity profiles plotted in wall units in Figure 5.24 show a Bingham number dependence only for $y^+ \geq 30$. As the Bingham number grows, the slope of the mean axial velocity increases slightly. The variations in these profiles are attributed to the friction velocity that slightly decreases as the number of Bn increases. This pattern in the axial velocity profiles indicates that the flow with $B_n = 0.40$ tends to be more transitional.

Figure 5.24 – Profiles of the mean axial velocity plotted in wall units, (a) near the inner wall; (b) near the outer wall. Left: case C ($B_n = 0.10, 0.25$ and 0.40 at $n = 0.65$ and $N = 0.15$); right: case D ($B_n = 0.10, 0.25$ and 0.40 at $n = 0.75$ and $N = 0.30$).

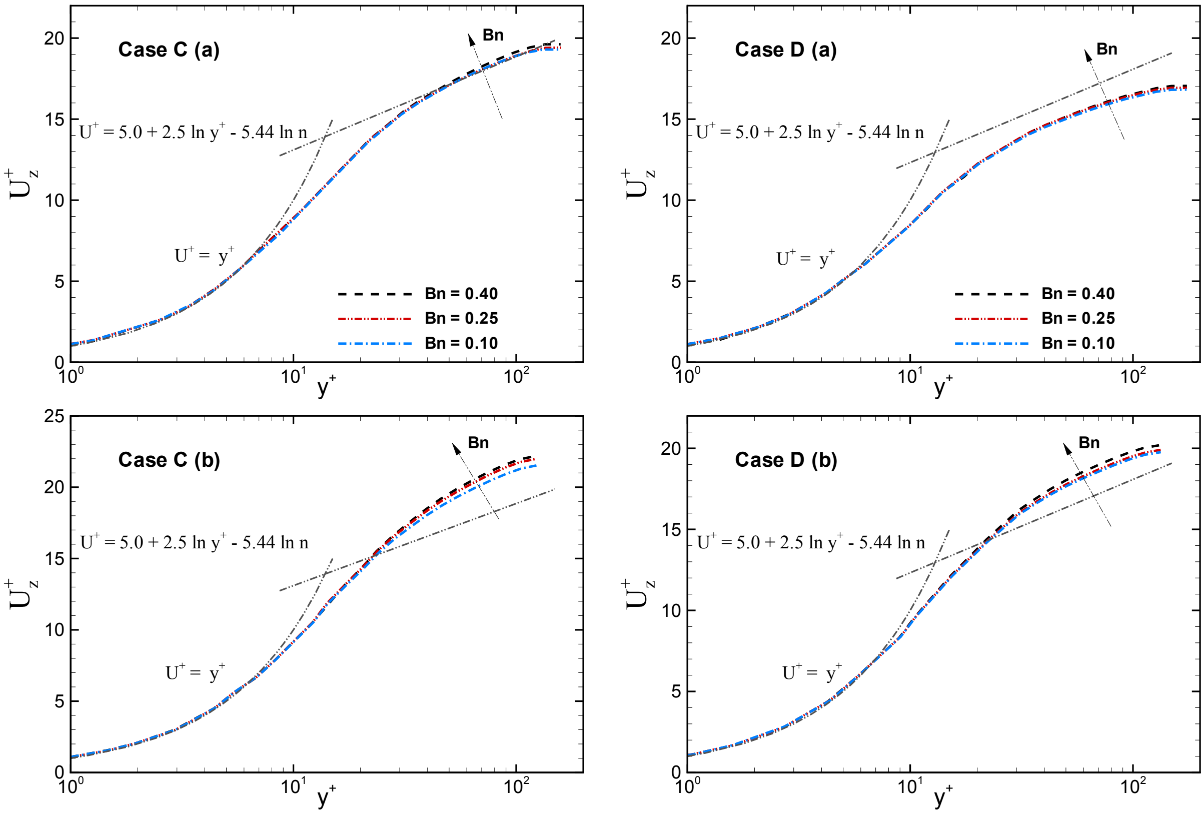

Source: Own elaboration.

Distributions of the mean viscosity normalized by the wall viscosity ν_{wall} are depicted in Figure 5.25. Increasing B_n, the ratio between the maximum value (at the center of the annular section) and the minimum value (near the walls) of the mean viscosity also grows. Similar to the effect of flow behavior index n, the mean viscosity profiles are constant up to $y^+ \approx 5$, and at around $y^+ \geq 10$ the mean viscosity increases rapidly towards the center of the annular section.

Figure 5.25 – Profiles of the normalized mean viscosity ν/ν_{wall} (a) Plotted as a function of r^*; (b) Plotted as a function of y^+, near the inner wall; (c) Plotted as a function of y^+, near the outer wall. Left: case C ($B_n = 0.10, 0.25$ and 0.40 at $n = 0.65$ and $N = 0.15$); right: case D ($B_n = 0.10, 0.25$ and 0.40 at $n = 0.75$ and $N = 0.30$).

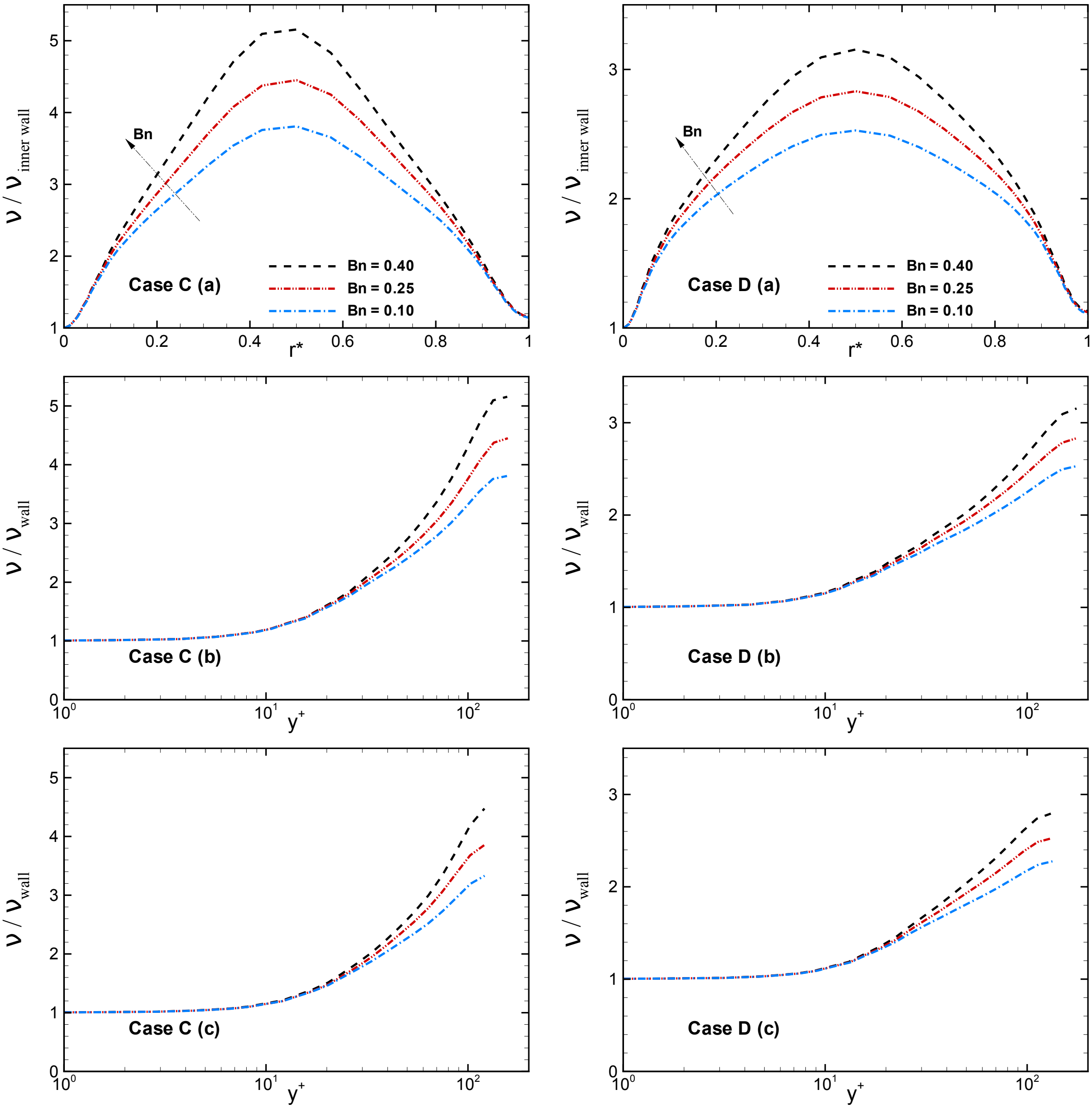

Source: Own elaboration.

The RMS velocity fluctuations and Reynolds shear stress components normalized by the bulk velocity $\mathrm{U_b}$ are shown in Figure 5.26 and Figure 5.27, respectively. Increasing the Bingham number is comparable to reducing the flow behavior index for the flow characteristics. The differences between the RMS velocity fluctuations in the axial direction are negligible. However, the values of the other second-order quantities decrease, showing a flow with weaker turbulent structures.

Figure 5.26 – Profiles of RMS velocity fluctuations in (a) axial, (b) radial, and (c) azimuthal direction. Left: case C ($B_n = 0.10, 0.25$ and 0.40 at $n = 0.65$ and $N = 0.15$); right: case D ($B_n = 0.10, 0.25$ and 0.40 at $n = 0.75$ and $N = 0.30$).

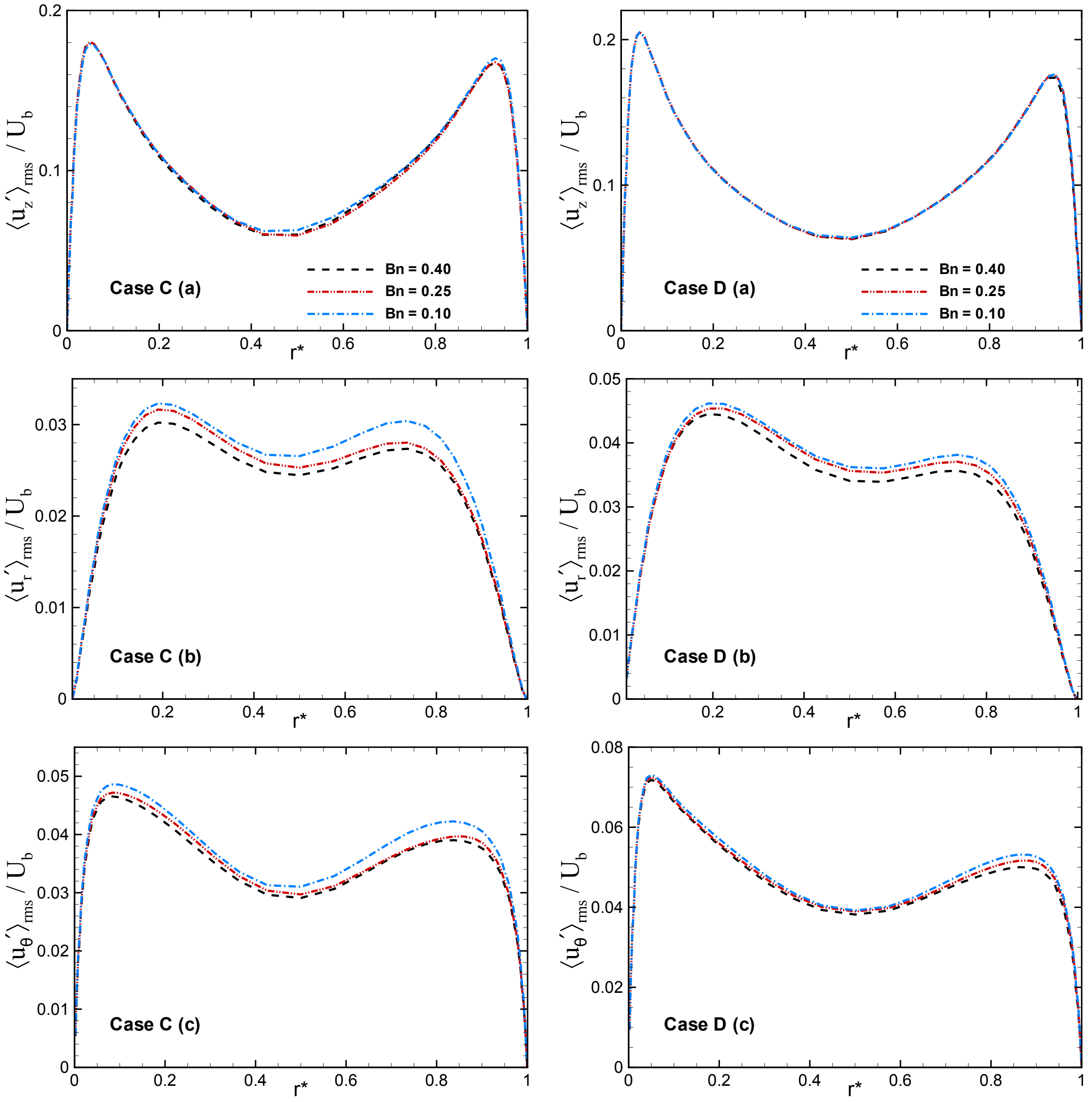

Source: Own elaboration.

Figure 5.28 exhibts the TKE profiles obtained for different Bingham numbers. The highest peak values are observed for the lowest values of B_n. Although the profiles differences are not very significant, the behavior reasonably agrees with the result (RUDMAN; BLACKBURN, 2006). The author argues that increasing yield stress reduces the TKE of the flow.

The effect of the Bingham number B_n on the pressure gradient and the skin friction coefficients are given in Table 5.9 and Table 5.10, respectively. Similar to the augment of the shear-thinning property, the increase of Bn reduces the turbulence intensities, consequently decreasing the pressure gradient and the skin friction coefficients.

Figure 5.27 – Profiles of Reynolds shear stress normalized by U_b^2, (a) Reynolds rz stress component and (b) Reynolds $r\theta$ stress component. Left: case C ($B_n = 0.10, 0.25$ and 0.40 at $n = 0.65$ and $N = 0.15$); right: case D ($B_n = 0.10, 0.25$ and 0.40 at $n = 0.75$ and $N = 0.30$).

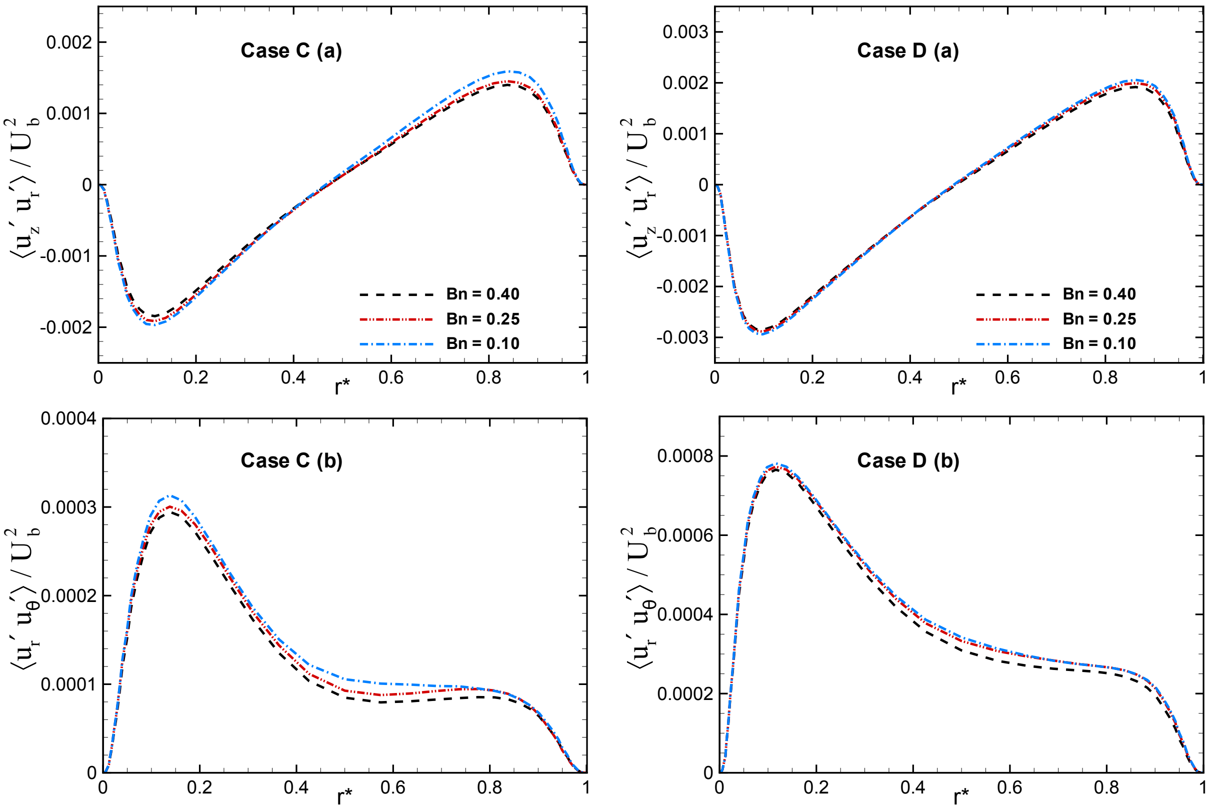

Source: Own elaboration.

Figure 5.28 – Profiles of the turbulence kinetic energy normalized by U_b^2. Left: case C ($B_n = 0.10, 0.25$ and 0.40 at $n = 0.65$ and $N = 0.15$); right: case D ($B_n = 0.10, 0.25$ and 0.40 at $n = 0.75$ and $N = 0.30$).

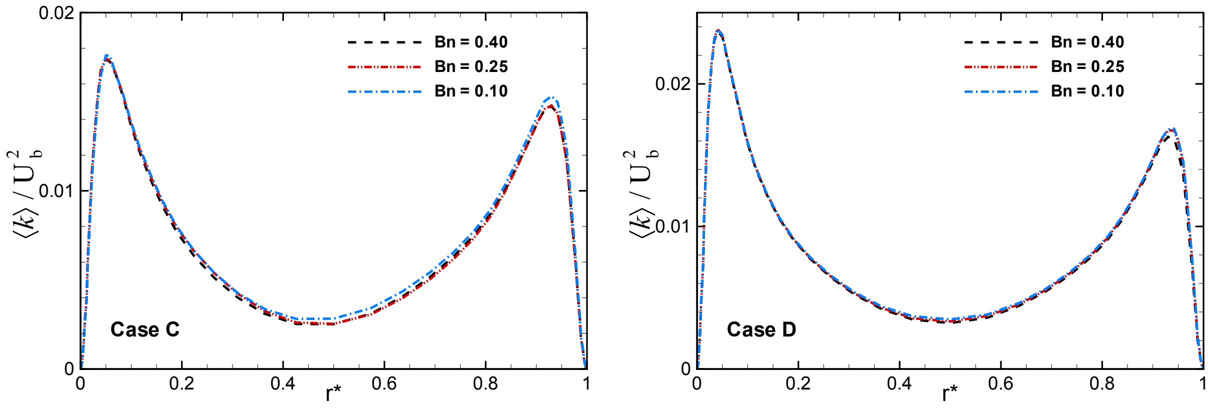

Source: Own elaboration.

Table 5.9 – Pressure gradient computed for different Bingham numbers.

	Sim	Bingham number (B_n)	Flow behavior index (n)	Rotation number (N)	Pressure gradient [$Pa\, m^{-1}$]
Case C	03	0.10	0.65	0.15	488.8
	05	0.25	0.65	0.15	477.1
	07	0.40	0.65	0.15	472.5
Case D	08	0.10	0.75	0.30	575.8
	10	0.25	0.75	0.30	566.9
	13	0.40	0.75	0.30	559.3

Source: Own elaboration.

Table 5.10 – Skin friction coefficients estimated for different Bingham numbers.

	Sim	Bingham number (B_n)	Flow behavior index (n)	Rotation number (N)	$f_{inner\ wall}$ x10^{-3}	$f_{outer\ wall}$ x10^{-3}
Case C	03	0.10	0.65	0.15	7.55	6.07
	05	0.25	0.65	0.15	7.50	5.86
	07	0.40	0.65	0.15	7.37	5.83
Case D	08	0.10	0.75	0.30	9.47	6.86
	10	0.25	0.75	0.30	9.39	6.72
	13	0.40	0.75	0.30	9.28	6.62

Source: Own elaboration.

5.7 Effect of the Rotation Number

Here is investigated the effect of the Rotation number (N) on the flow features. Table 5.11 summarizes the configuration of the cases studied.

Table 5.11 – Set of simulations for investigating the effect of Rotation number on the flow quantities.

	Sim	Bingham number (B_n)	Flow behavior index (n)	Rotation number (N)	BulkVelocity [$m\ s^{-1}$]
Case E	03	0.10	0.65	0.15	1.93
	09	0.10	0.65	0.30	1.93
Case F	06	0.40	0.70	0.15	1.93
	14	0.40	0.70	0.30	1,93

Source: Own elaboration.

5.7.1 Instantaneous Flow

Figures 5.29 and 5.30 exhibit the contours of instantaneous axial velocity at a distance $y^+ \approx 15$ from the inner and outer wall, respectively. It is worth noting that the rotation effect is more significant close to the inner walls. Contours of instantaneous axial velocity are almost parallel to the streamwise axis for flows with Rotation number $N = 0.15$. On the other hand, as N rises, these contours become inclined to the streamwise axis, indicating that the centrifugal force imposed by the rotation affects the flow pattern in that region. Near the outer wall (Figure 5.30), the streaks showed alignment with the axial direction for both cases. In addition, close to both walls, the increase in rotation reduced the size of low-speed streaks and enhanced the number of high-speed streaks regions.

Figure 5.29 – Contours of instantaneous axial velocity at $y^+ \approx 15$ from the inner wall (a) case E ($B_n = 0.10$ and $n = 0.65$) ranging from $0.34U_b$ to $1.5U_b$; (b) case F ($B_n = 0.40$ and $n = 0.70$) ranging from $0.42U_b$ to $1.48U_b$. Red color stands for maximum values, and blue for the minimum. Top: Rotation number $N = 0.15$; bottom: Rotation number $N = 0.30$.

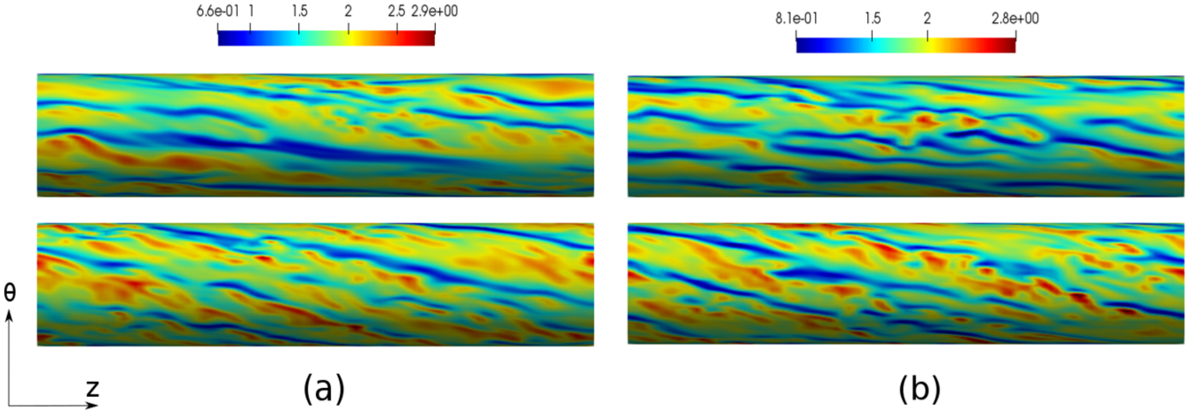

Source: Own elaboration.

Figure 5.30 – Contours of instantaneous axial velocity at $y^+ \approx 15$ from the outer wall (a) case E ($B_n = 0.10$ and $n = 0.65$) ranging from $0.34U_b$ to $1.3U_b$; (b) case F ($B_n = 0.40$ and $n = 0.70$) ranging from $0.36U_b$ to $1.3U_b$. Red color stands for maximum values, and blue for the minimum. Top: Rotation number $N = 0.15$; bottom: Rotation number $N = 0.30$.

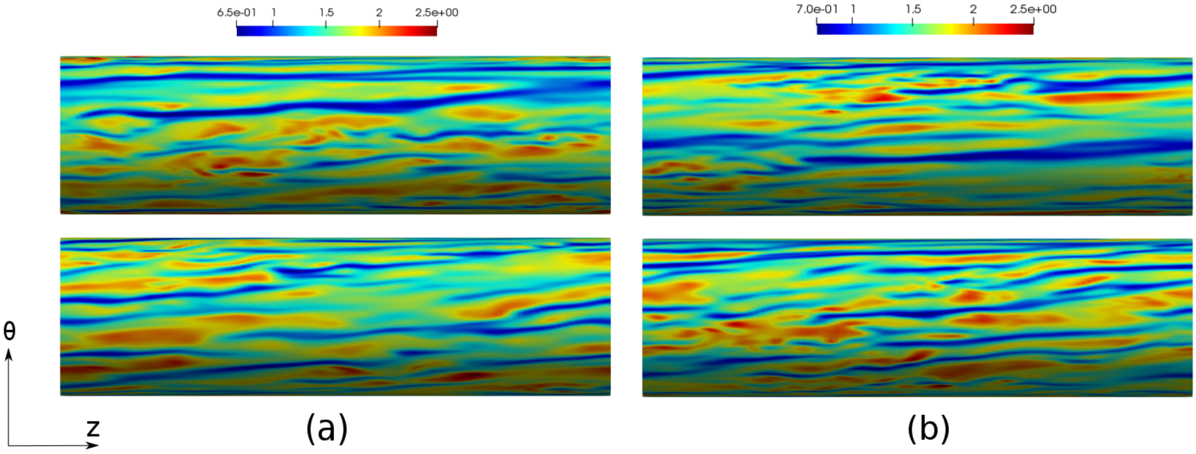

Source: Own elaboration.

The rotation effect on instantaneous viscosity over a $z - \theta$ plane located at $y^+ \approx 100$ is reported in Figure 5.31. There are no significant differences over the instantaneous viscosity field. The ranges of viscosity fluctuations are very close for both rotation numbers.

Figure 5.31 – Contours of instantaneous viscosity at $y^+ \approx 100$ from the outer wall (a) case E ($B_n = 0.10$ and $n = 0.65$) ranging from $1\nu_{wall}$ to $8\nu_{wall}$; (b) case F ($B_n = 0.40$ and $n = 0.70$) ranging from $1\nu_{wall}$ to $11\nu_{wall}$. Red color stands for maximum values, and blue for the minimum. Top: Rotation number $N = 0.15$; bottom: Rotation number $N = 0.30$.

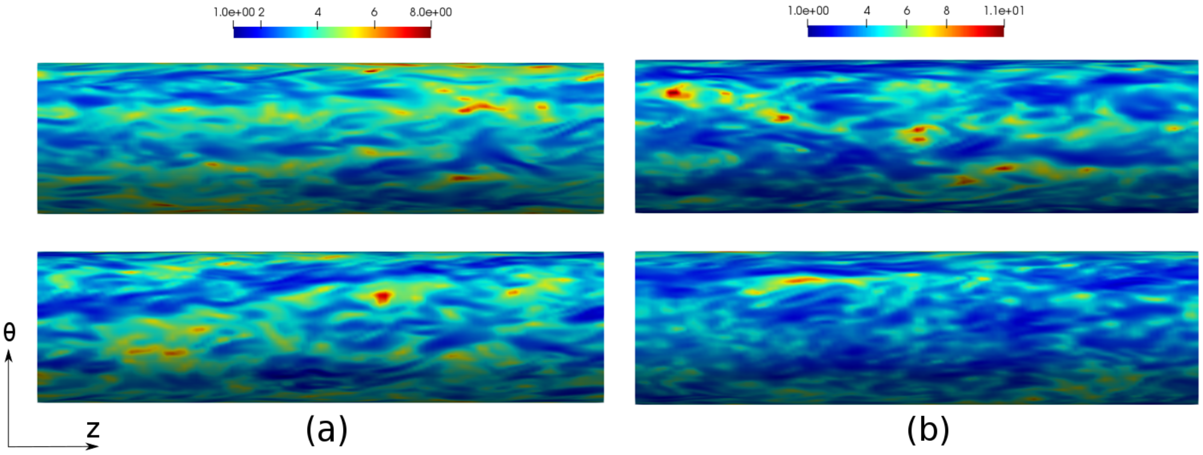

Source: Own elaboration.

Figure 5.32 shows the vortical structure through the instantaneous iso-surfaces of the Q-criterion. The increase in the rotation of the inner cylinder yields an enhancement in the number of vortices present in the flow, indicating a more vigorous turbulent activity.

Figure 5.32 – Top view of the iso-surfaces of the Q-criterion (Q=750) colored by the instantaneous axial velocity (a) case E ($B_n = 0.10$ and $n = 0.65$); (b) case F ($B_n = 0.40$ and $n = 0.70$). Red color stands for maximum values, and blue for the minimum. Top: Rotation number $N = 0.15$; bottom: Rotation number $N = 0.30$.

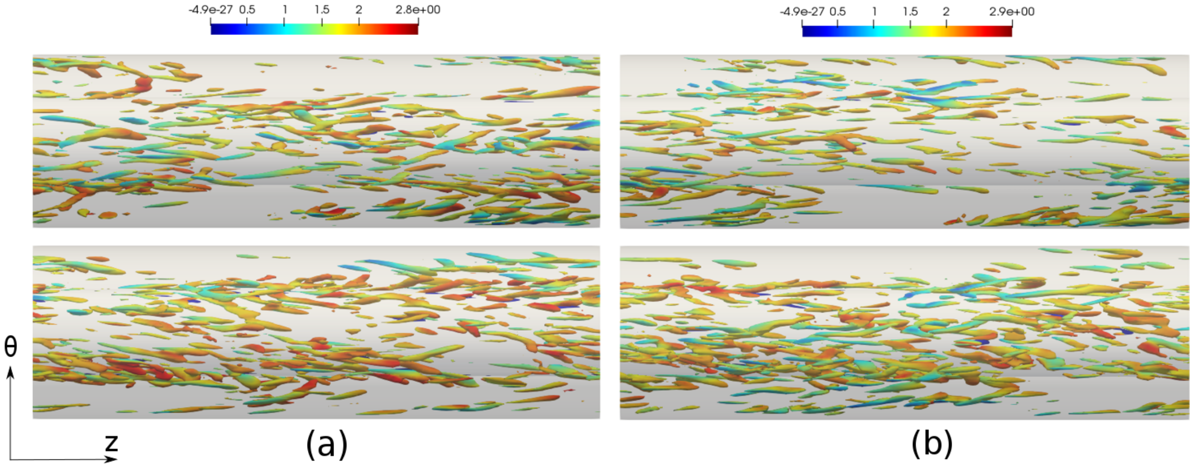

Source: Own elaboration.

5.7.2 Mean Flow Quantities

Figure 5.33 depicts the mean axial and azimuthal velocity profiles. The bulk velocity normalizes the mean axial velocity distributions, and the azimuthal velocity components are normalized by the rotational velocity of the inner wall. As also observed by Nouri and Whitelaw (1994), Okamoto and Shima (2005), and Chung and Sung (2005) the mean axial velocity profiles become flattered with increasing the rotating number N. From Figure 5.33b, it can be observed that for a higher value of N, the azimuthal velocity gradient near the walls also enhanced.

Figure 5.33 – Profiles of the mean (a) axial and (b) azimuthal velocity. The bulk velocity normalizes the mean axial velocity, and the mean azimuthal velocity is normalized by the rotational velocity of the inner wall. Left: case E ($N = 0.15$ and $N = 0.30$ at $B_n = 0.10$ and $n = 0.70$); right: case F ($N = 0.15$ and $N = 0.30$ at $B_n = 0.40$ and $n = 0.65$).

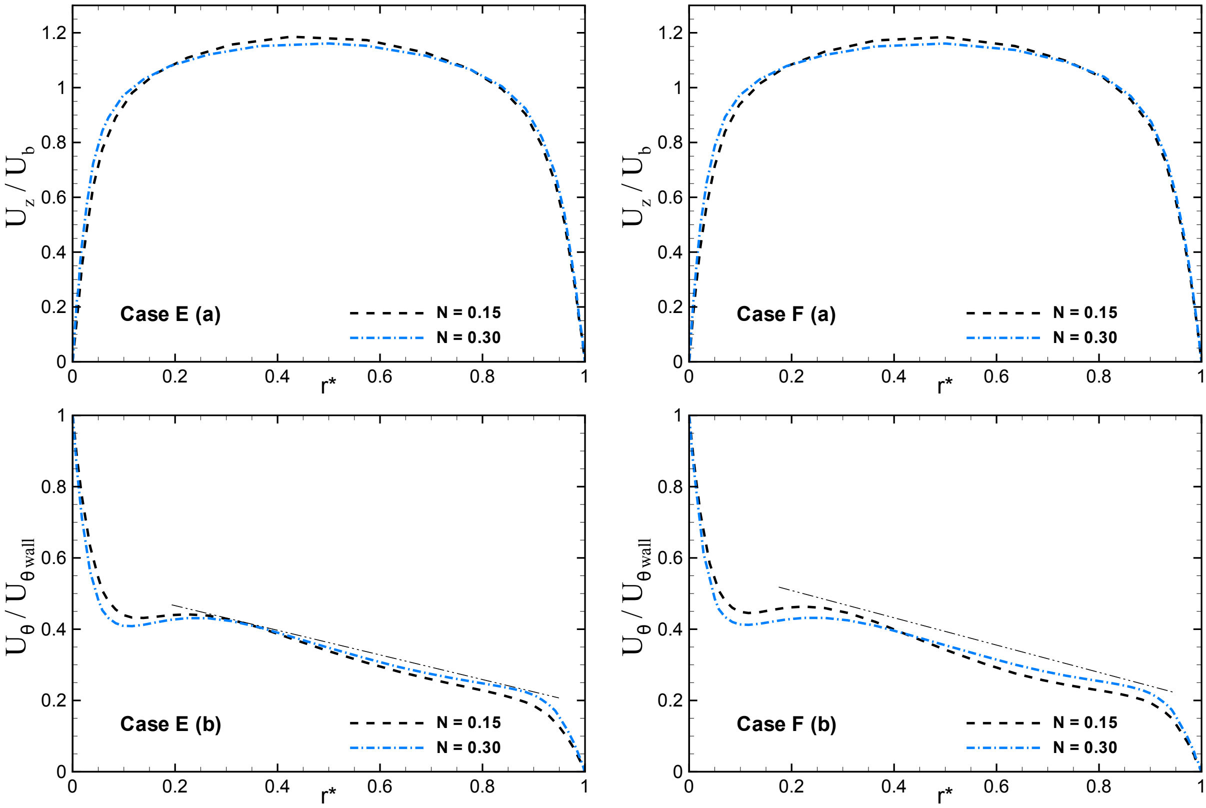

Source: Own elaboration.

The mean axial velocity profiles plotted in wall units are reported in Figure 5.34. The difference observed near the inner and outer walls is due to the rotation effect of the inner cylinder, which results in an augment of the wall shear stress. The rotation effect is most evident near the inner wall, although it propagates through the gap and is also seen to a smaller degree in the vicinity of the outer one.

Figure 5.34 – Profiles of the mean axial velocity plotted in wall units, (a) near the inner wall; (b) near the outer wall. Left: case E ($N = 0.15$ and $N = 0.30$ at $B_n = 0.10$ and $n = 0.70$); right: case F ($N = 0.15$ and $N = 0.30$ at $B_n = 0.40$ and $n = 0.65$).

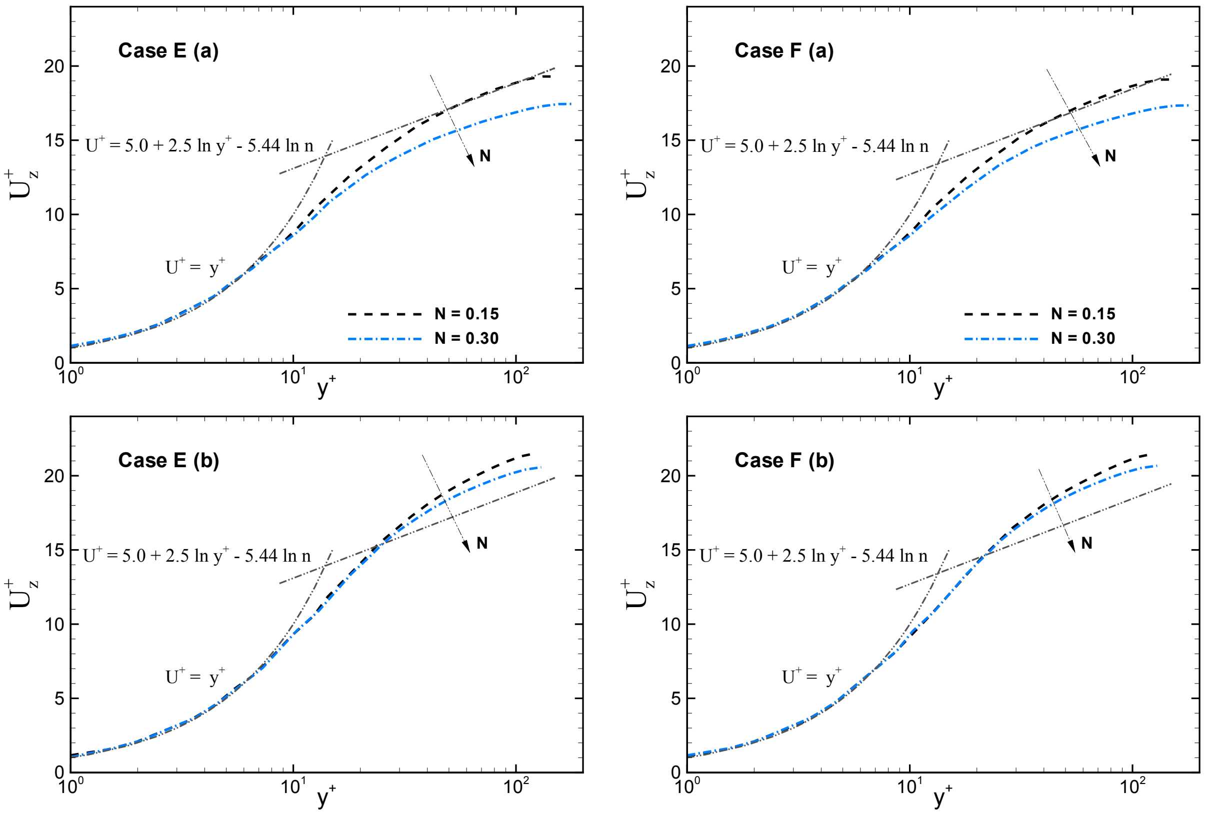

Source: Own elaboration.

Profiles of mean viscosity ν of normalized by ν_{wall} for cases E and F are shown in Figure 5.35. From Figure 5.35a, it can be noticed that the rotation effect does not produce considerable discrepancies in the viscosity profiles, as seen previously for the effects of flow behavior index and Bingham number. The ratio between the maximum value (in the center of the annular region) and the minimum value (near the walls) of the mean viscosity distribution is similar for both rotation numbers, although the profiles for $N = 0.30$ present a more parabolic behavior. Distributions of mean viscosity plotted in wall coordinates (Figures 5.35b and 5.35c) follow the tendency of the analyses discussed above. The profiles are constant up to $y^+ \approx 5$ and after $y^+ \geq 10$, the mean viscosity increases towards the center of the annular section.

The RMS velocity fluctuations normalized by the bulk velocity are reported in Figure 5.36. A variation in the peak value of the RMS axial velocity fluctuations near the inner wall region appears as N increases. However, the rotation effect is more evident in the RMS velocity fluctuations in radial and azimuthal directions. The fluctuation levels increase in strength and become asymmetric, which can be attributed to the destabilizing effect of the centrifugal forces arising from the rotation of the inner cylinder. (CHUNG; SUNG, 2005; PONCET et al., 2014).

Figure 5.35 – Profiles of the normalized mean viscosity ν/ν_{wall}. (a) Plotted as a function of r^*, (b) Plotted as a function of y^+, near the inner wall; (c) Plotted as a function of y^+, near the outer wall. Left: case E ($N = 0.15$ and $N = 0.30$ at $B_n = 0.10$ and $n = 0.70$); right: case F ($N = 0.15$ and $N = 0.30$ at $B_n = 0.40$ and $n = 0.65$).

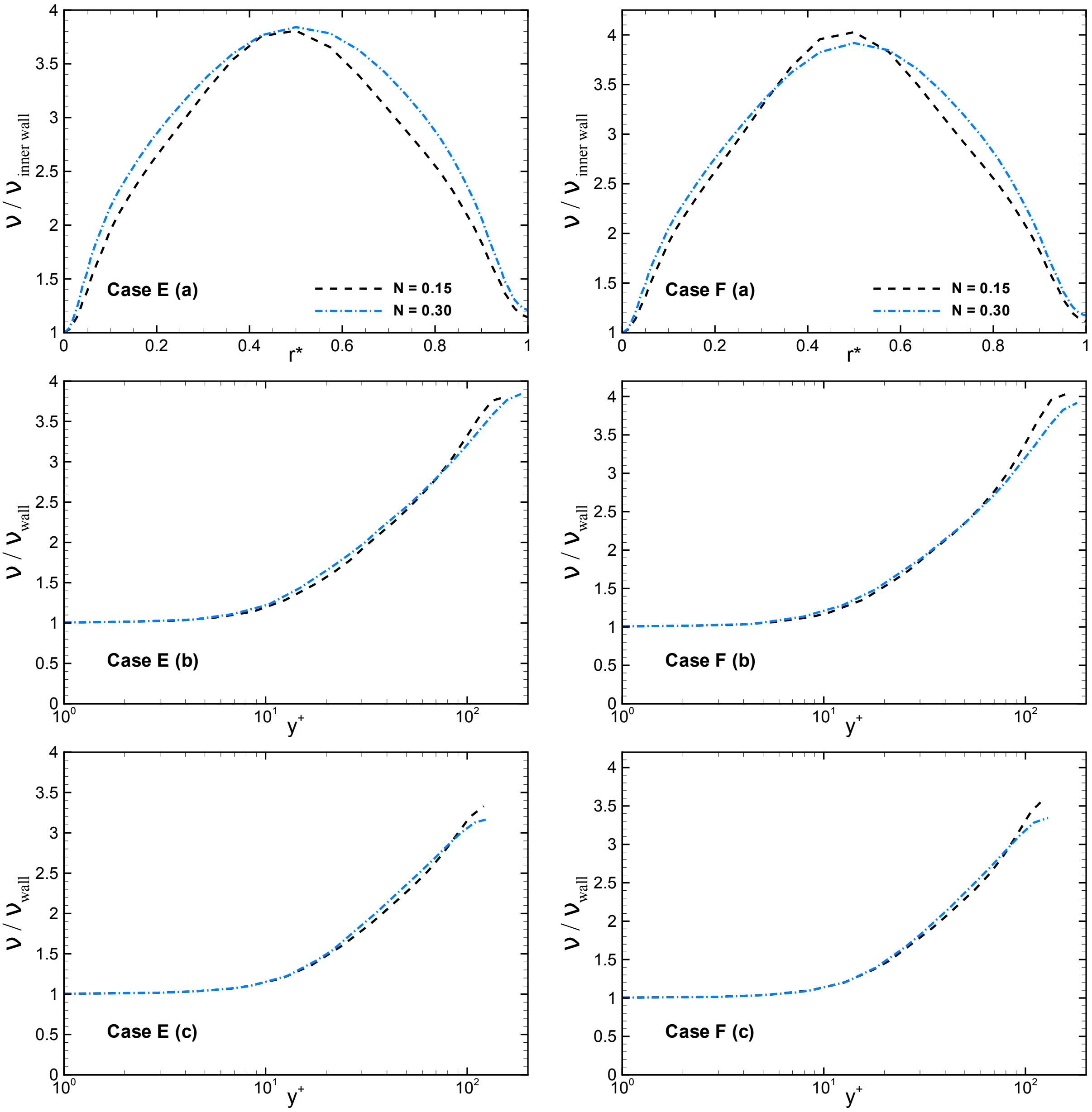

Source: Own elaboration.

Figure 5.36 – Profiles of RMS velocity fluctuations in (a) axial, (b) radial, and (c) azimuthal directions. Left: case E ($N = 0.15$ and $N = 0.30$ at $B_n = 0.10$ and $n = 0.70$); right: case F ($N = 0.15$ and $N = 0.30$ at $B_n = 0.40$ and $n = 0.65$).

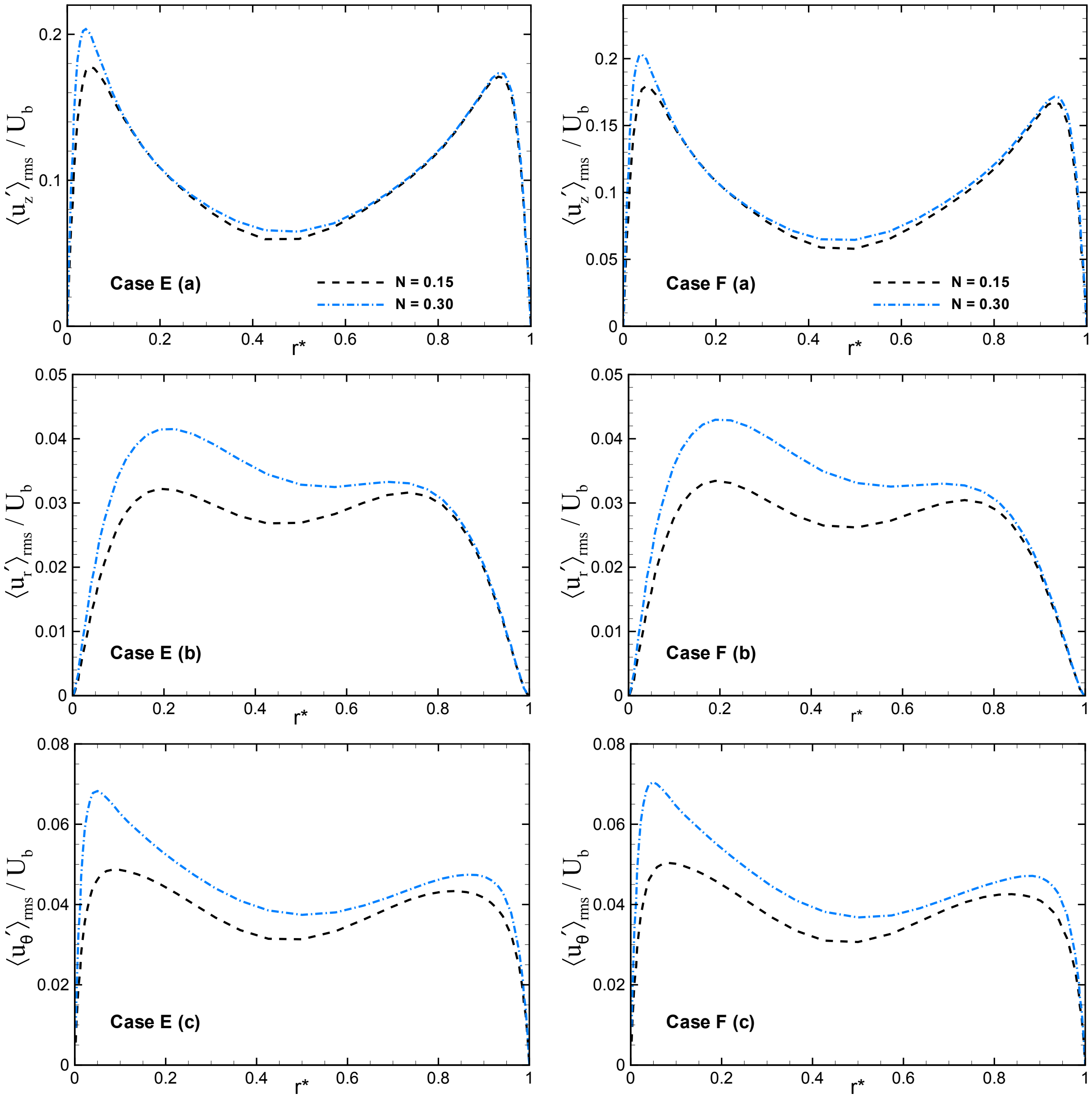

Source: Own elaboration.

The Reynolds shear stress components normalized by the bulk velocity are illustrated in Figure 5.37. The profiles also enhance in amplitude as N increases. The Reynolds $r\theta$ stress term demonstrates a significant sensitivity to the rotation rate generated by augmenting radial and azimuthal velocity fluctuations due to the higher amount of near-wall turbulence events (high- and low-speed elongated streaks and vortical structures) as illustrated in Figures 5.29 and 5.32.

Figure 5.37 – Profiles of Reynolds shear stress normalized by U_b^2, (a) Reynolds rz stress component and (b) Reynolds $r\theta$ stress component. Left: case E ($N = 0.15$ and $N = 0.30$ at $B_n = 0.10$ and $n = 0.70$); right: case F ($N = 0.15$ and $N = 0.30$ at $B_n = 0.40$ and $n = 0.65$).

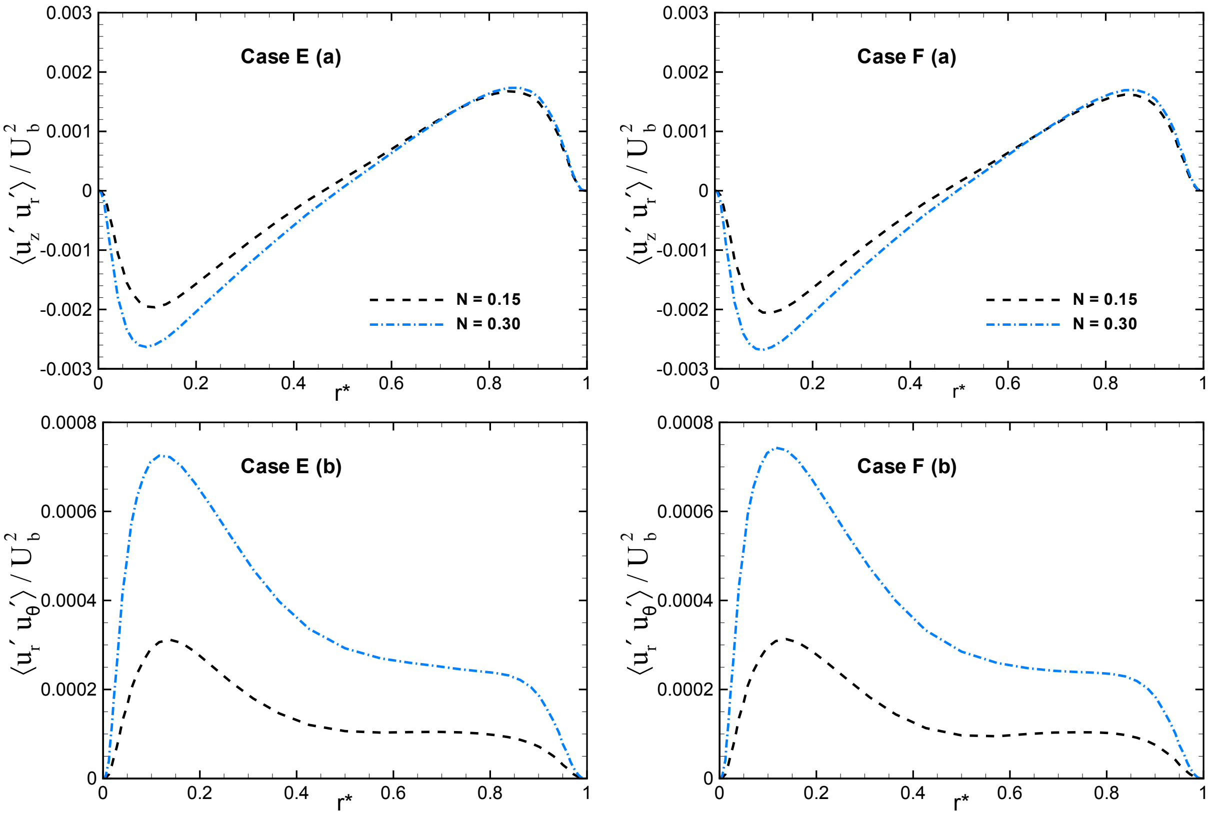

Source: Own elaboration.

Profiles of mean turbulence kinetic energy (TKE) are reported in Figure 5.38. The rotation effect of the inner cylinder produces an increase of TKE across the domain, with a significantly higher peak value ($\approx 33\%$) near the inner wall. In addition, the TKE distribution becomes more asymmetrical with a higher value of N.

The contribution of the Rotation number N to the pressure gradient is given in Table 5.12. Due to the enhancement of wall shear stress induced by the rotation effect, the pressure gradient (Eq. 5.4) rises by around 9% in both cases.

The effect of the Rotation number on the skin friction coefficients is reported in Table 5.13. The difference in the friction coefficient on the inner wall is approximately 15% for both cases. On the other hand, the effect of rotation number on the outer wall is less sensitive; the difference between N for f values is 5%.

Figure 5.38 – Profiles of the turbulence kinetic energy normalized by U_b^2. Left: case E ($N = 0.15$ and $N = 0.30$ at $B_n = 0.10$ and $n = 0.70$); right: case F ($N = 0.15$ and $N = 0.30$ at $B_n = 0.40$ and $n = 0.65$).

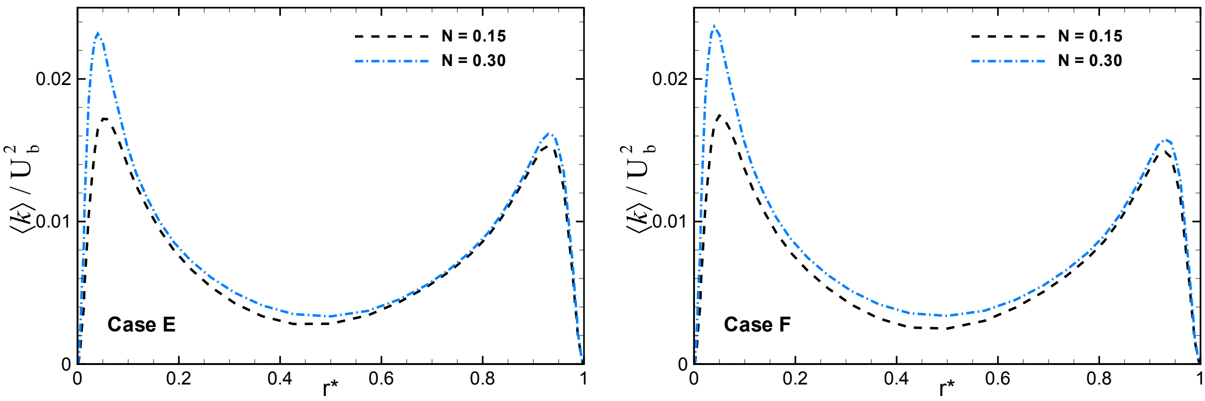

Source: Own elaboration.

Table 5.12 – Pressure gradient computed for different rotation numbers.

	Sim	Bingham number (B_n)	Flow behavior index (n)	Rotation number (N)	Pressure gradient [$Pa\, m^{-1}$]
Case E	03	0.10	0.65	0.15	488.8
	09	0.10	0.65	0.30	536.3
Case F	06	0.40	0.70	0.15	492.9
	14	0.40	0.70	0.30	535.6

Source: Own elaboration.

Table 5.13 – Skin friction coefficients estimated for different rotation numbers.

	Sim	Bingham number (B_n)	Flow behavior index (n)	Rotation number (N)	$f_{inner\ wall}$ x10^{-3}	$f_{outer\ wall}$ x10^{-3}
Case E	03	0.10	0.65	0.15	7.55	6.07
	09	0.10	0.65	0.30	8.86	6.37
Case F	06	0.40	0.70	0.15	7.69	6.08
	14	0.40	0.70	0.30	8.95	6.31

Source: Own elaboration.

5.8 Comparison Between SGS Models and the UDNS

This section explores the performance of two SGS models, namely Dynamic Smagorinsky and WALE models, and the UDNS (no-model LES) on the flow features is studied. The cases analyzed in this section are reported in Table 5.14.

The Dynamic Smagorinsky and WALE models calculate the eddy viscosity ν_{SGS} differently. The Dynamic Smagorinsky is an algebraic model in which subgrid-scale stresses are parameterized using the resolved turbulent stresses, and the underlying assumption is that the small scales are in local equilibrium

Table 5.14 – Set of simulations used to compare the performance of SGS models and the UDNS.

	Sim	Bingham number (B_n)	Flow behavior index (n)	Rotation number (N)	Bulk velocity $[m\ s^{-1}]$
Case G	04	0.25	0.70	0.15	1.93
Case H	15	0.40	0.65	0.30	1.93

Source: Own elaboration.

between energy production and dissipation (GERMANO et al., 1991). On the other hand, the WALE model is based on the square of the velocity gradient tensor and considers the effects of both the strain and the rotation rate of the smallest resolved turbulent fluctuations (NICOUD; DUCROS, 1999).

Figure 5.39 exhibits the mean axial velocity and azimuthal velocity profiles for different SGS models and the UDNS. The SGS models and the UDNS match well with each other for the mean axial velocity, while a maximum difference of 6% was observed between the Dynamic Smagorinsky model and UDNS at $r^* = 0.5$ in the azimuthal velocity component for case G.

Figure 5.39 – Profiles of the mean (a) axial and (b) azimuthal velocity. The bulk velocity normalizes the mean axial velocity, and the mean azimuthal velocity is normalized by the rotational velocity of the inner wall. Left: case G ($N = 0.15$, $B_n = 0.25$ and $n = 0.70$); right: case H ($N = 0.30$, $B_n = 0.40$ and $n = 0.65$).

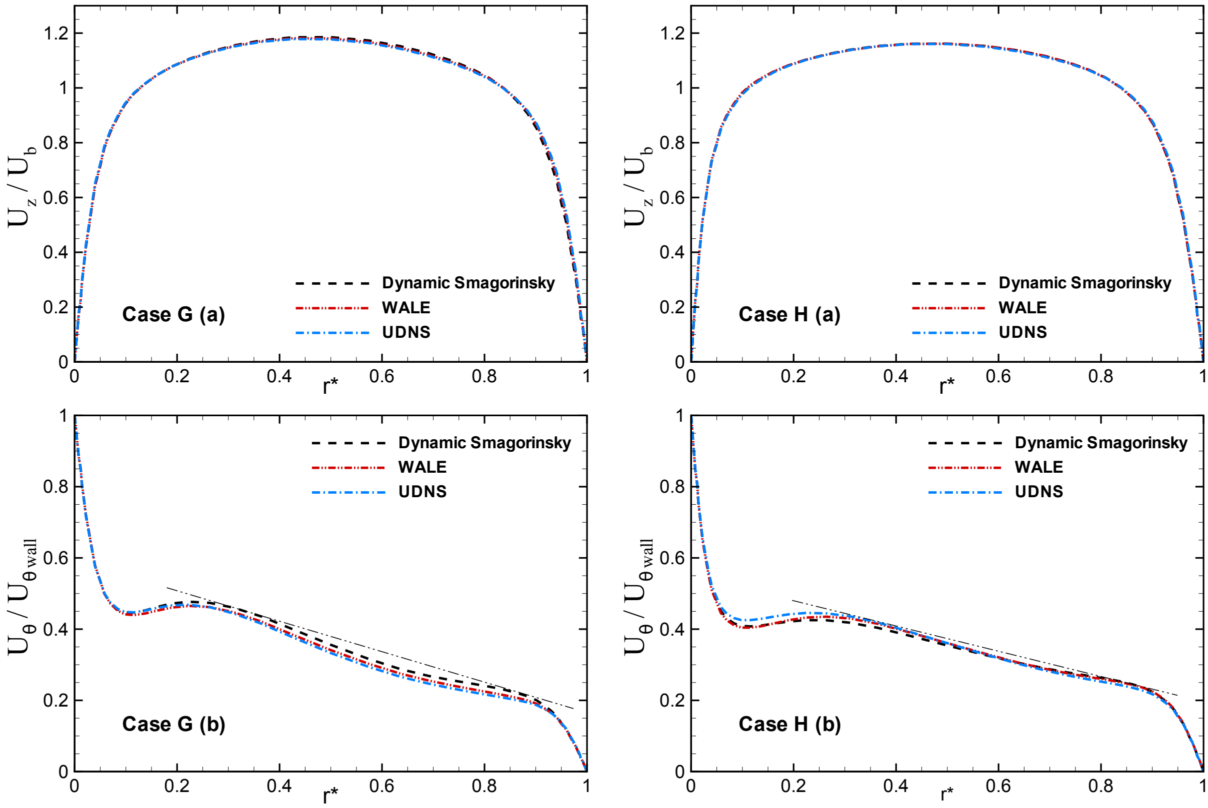

Source: Own elaboration.

Figure 5.40 shows the mean axial velocity distributions plotted in wall units, the profiles obtained with the SGS models and the UDNS results are qualitatively consistent with each other near the inner wall, whereas near the outer wall due to the higher friction velocity value the UDNS underpredict ($\approx$1,1%) the results at $y^+ > 30$. Even the inner wall presenting a higher value of the wall shear stress for UDNS compared to SGS models, the rotation effect seems to cancel out the friction velocity influence for $y^+ > 30$.

Figure 5.40 – Profiles of the mean axial velocity plotted in wall units (a) near the inner wall and (b) near the outer wall. Left: case G ($N = 0.15$, $B_n = 0.25$ and $n = 0.70$); Right: case H ($N = 0.30$, $B_n = 0.40$ and $n = 0.65$).

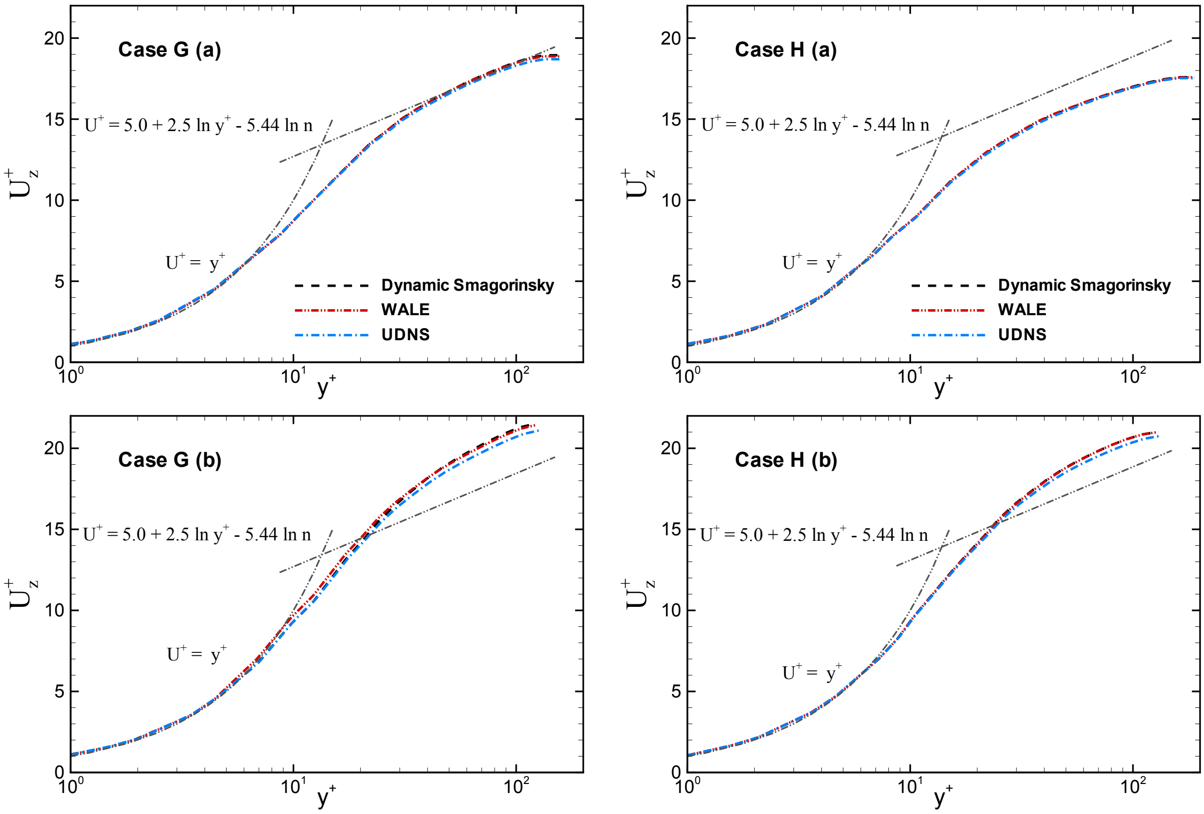

Source: Own elaboration.

Profiles of mean viscosity normalized by ν_{wall} and the mean turbulence kinetic energy (TKE) per unit mass normalized by U_b^2 are illustrated in Figures 5.41 and 5.42, respectively. For both flow properties, the SGS models agree with the UDNS results.

Figure 5.41 – Profiles of the normalized mean viscosity ν/ν_{wall}. (a) Plotted as a function of r^*, (b) plotted as a function of y^+, near the inner wall; (c) plotted as a function of y^+, near the outer wall. Left: case G ($N = 0.15$, $B_n = 0.25$ and $n = 0.70$); Right: case H ($N = 0.30$, $B_n = 0.40$ and $n = 0.65$).

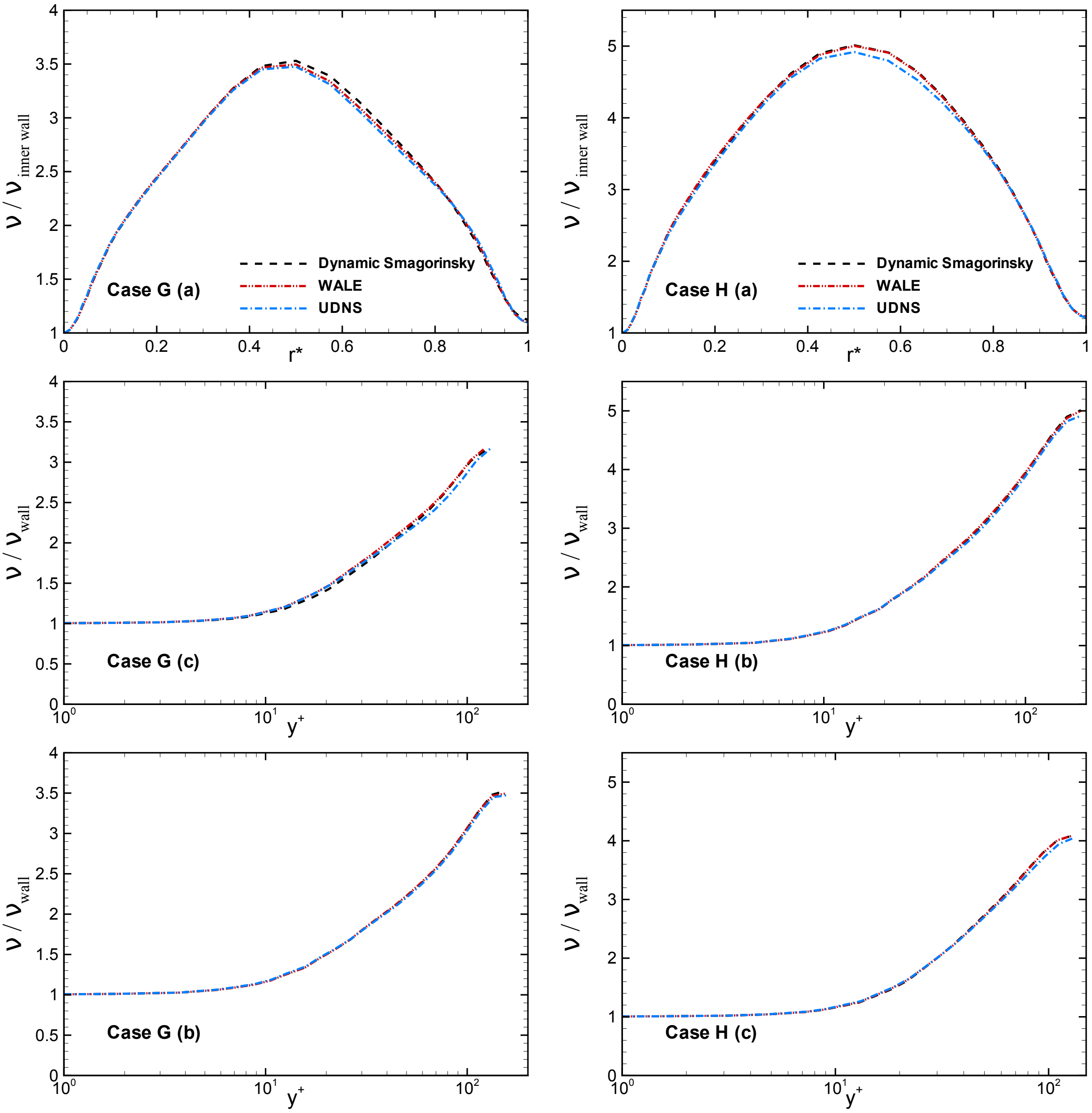

Source: Own elaboration.

The RMS velocity fluctuations computed with different SGS models and the UDNS are shown in Figure 5.43. Results for Dynamic Smagorinsky and WALE models are in close agreement. The UDNS overpredicts the peak values compared with SGS models in the radial and azimuthal RMS velocity fluctuations. The major differences between SGS models and the UDNS in the radial component are around 5.5% and 4.2% near the outer wall ($r^* \approx 0.80$) for cases G and H, respectively, while the maximum deviations between SGS models and the UDNS in the azimuthal direction are approximately 6% for case G and 4% for case H.

Figure 5.42 – Profiles of the turbulence kinetic energy normalized by U_b^2. Left: case G ($N = 0.15$, $B_n = 0.25$ and $n = 0.70$); Right: case H ($N = 0.30$, $B_n = 0.40$ and $n = 0.65$).

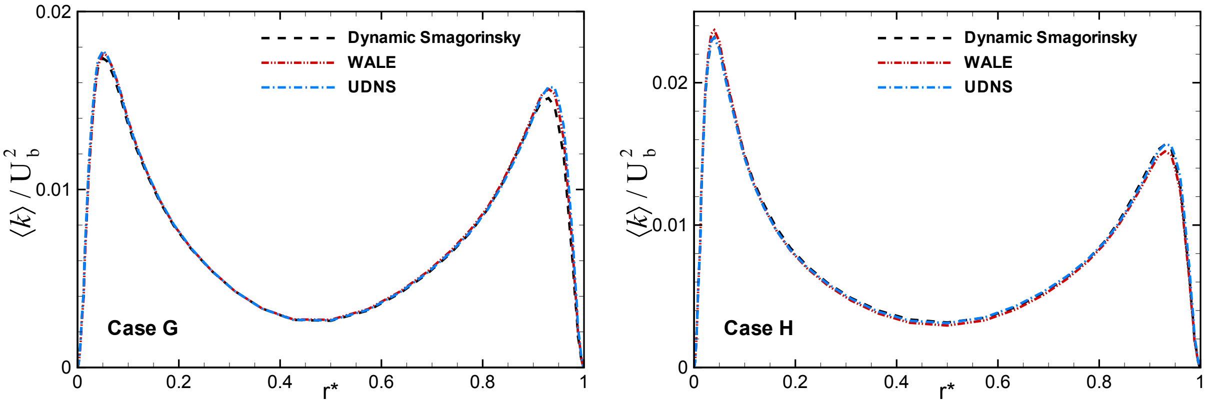

Source: Own elaboration.

Figure 5.44 depicts the profiles of Reynolds shear stress. The UDNS and the SGS models present similar trends. However, the UDNS slightly overestimate the peaks of the Reynolds shear stress $u_z'u_r'$ component.

The pressure gradient computed for different SGS models and the UDNS is given in Table 5.15. The Dynamic Smagorinsky and WALE models are in good agreement. On the other hand, the UDNS overpredicts pressure gradient values by around 3%.

Table 5.15 – Pressure gradient computed for different SGS models and the UDNS. Left: case G ($N = 0.15$, $B_n = 0.25$ and $n = 0.70$); right: case H ($N = 0.30$, $B_n = 0.40$ and $n = 0.65$).

	Case G	Case H
	Pressure Gradient $[Pa\ m^{-1}]$	Pressure Gradient $[Pa\ m^{-1}]$
Dynamic Smagorinsky	495.6	520.3
WALE	495.8	520.6
UDNS	518.6	572.7

Source: Own elaboration.

The skin friction coefficients f estimated for different SGS models and the UDNS are reported in Table 5.16. The Dynamic Smagorinsky and WALE models match each other. The UDNS overpredicts the f values by less than 1% compared with SGS models in the inner walls, while in the outer walls the difference between SGS models and the UDNS for the skin friction coefficients is approximately 4%.

Overall, as also noted in the previous chapter, the results obtained with Dynamic Smagorinsky and WALE models match well with each other; and when the SGS models predictions are compared with the UDNS results, the differences between the two approaches in the flow characteristics are lesser than 6%.

Figure 5.43 – Profiles of RMS velocity fluctuations normalized by the bulk velocity U_b (a) axial, (b) radial, and (c) azimuthal directions. Left: case G ($N = 0.15$, $B_n = 0.25$ and $n = 0.70$); Right: case H ($N = 0.30$, $B_n = 0.40$ and $n = 0.65$).

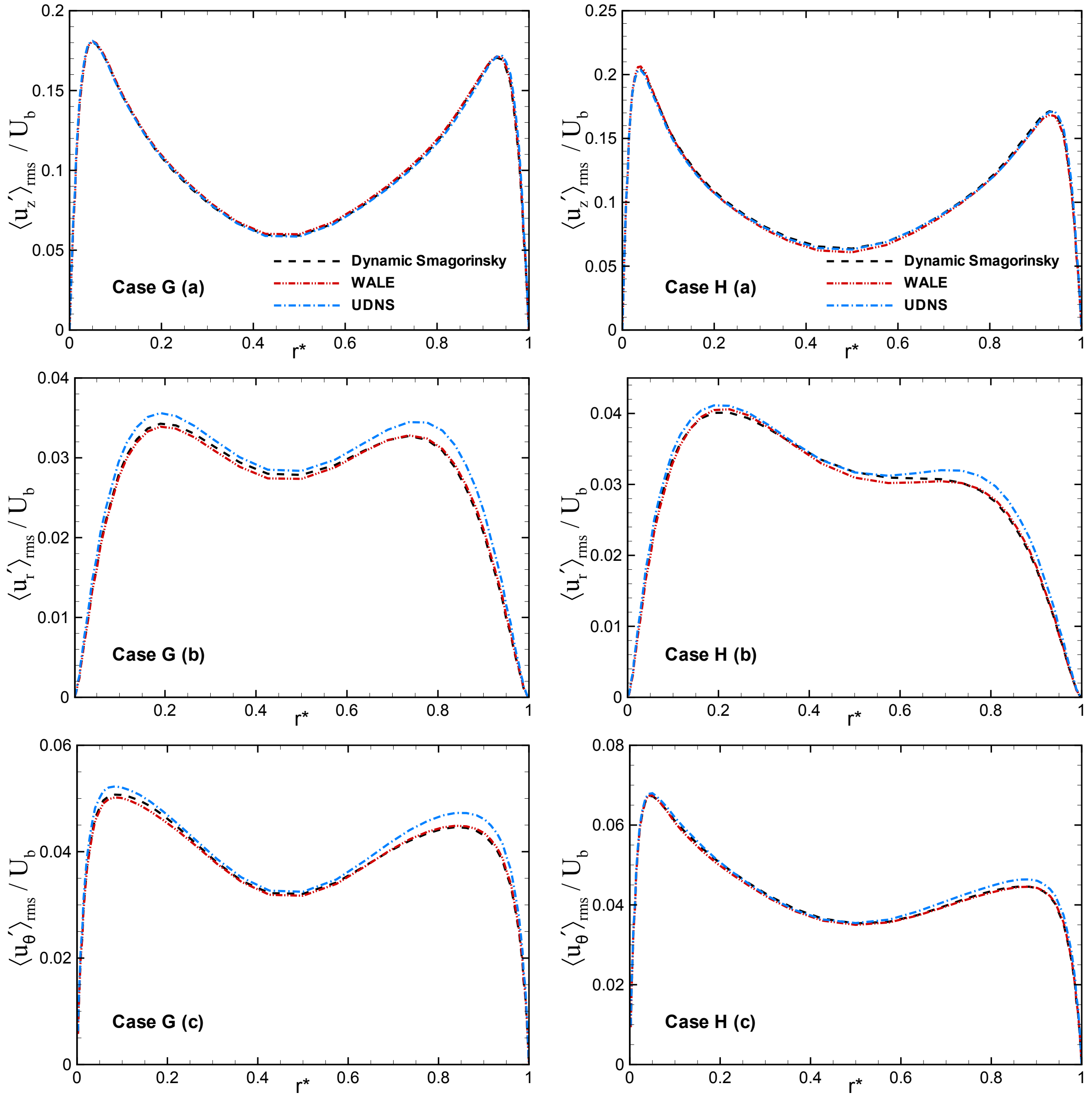

Source: Own elaboration.

Figure 5.44 – Profiles of Reynolds shear stress normalized by U_b^2 (a) Reynolds rz stress component and (b) Reynolds $r\theta$ stress component. Left: case G ($N = 0.15$, $B_n = 0.25$ and $n = 0.70$); Right: case H ($N = 0.30$, $B_n = 0.40$ and $n = 0.65$).

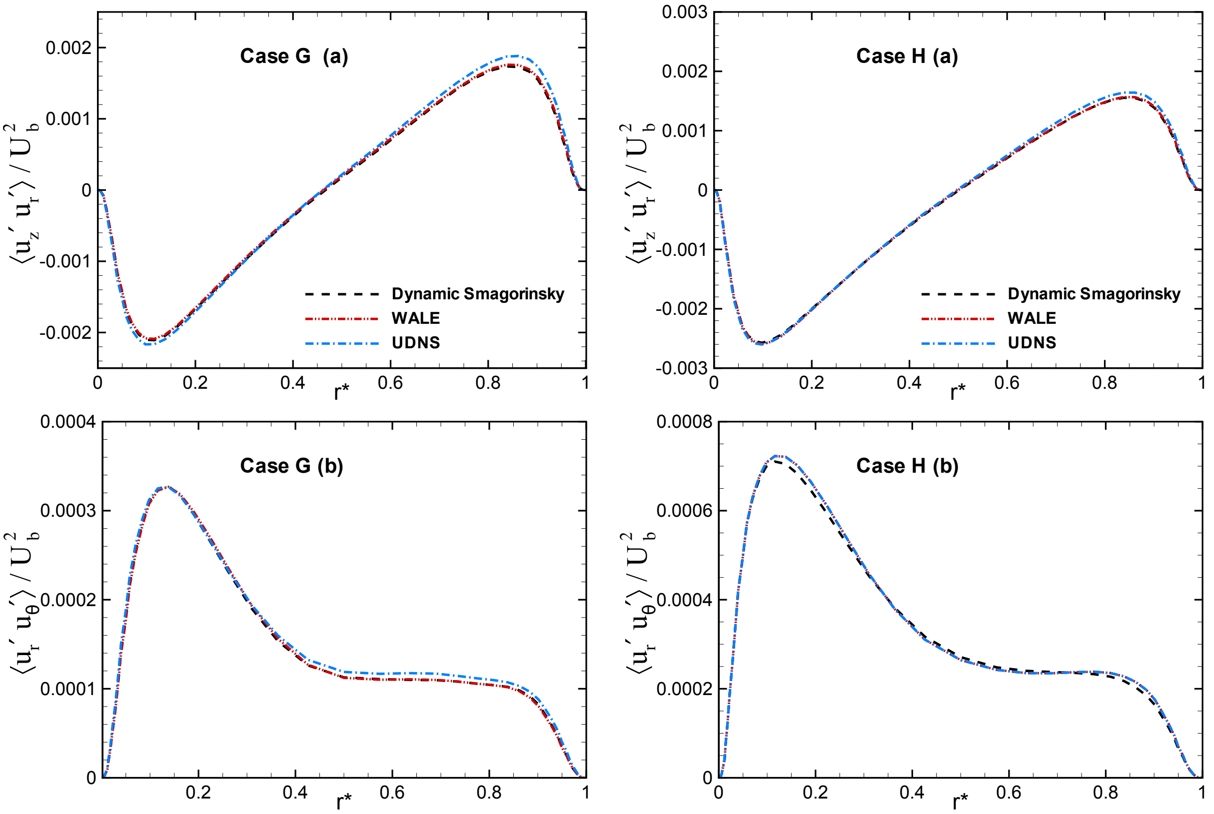

Source: Own elaboration.

Table 5.16 – Skin friction coefficients estimated for different SGS models and the UDNS. Top: case G ($N = 0.15$, $B_n = 0.25$ and $n = 0.70$); Bottom: case H ($N = 0.30$, $B_n = 0.40$ and $n = 0.65$).

Case G	$f_{inner\ wall}$ x10^{-3}	$f_{outer\ wall}$ x10^{-3}
Dynamic Smagorinsky	7.83	6.07
WALE	7.83	6.07
UDNS	7.93	6.48
Case H	$f_{inner\ wall}$ x10^{-3}	$f_{outer\ wall}$ x10^{-3}
Dynamic Smagorinsky	8.72	6.12
WALE	8.73	6.21
UDNS	8.76	6.25

Source: Own elaboration.

Chapter Summary

In this chapter, large-eddy simulations of Herschel-Bulkley fluids in a concentric annular section with rotation of the inner cylinder were performed at $Re_G \approx 9,000$. The effects of the flow behavior index ($n = 0.75$,0.70 and 0.65), Bingham number ($B_n = 0.10$,0.25 and 0.40), and the influence of Rotation number ($N = 0.15$ and 0.30) on the flow quantities were investigated. The performance of two SGS models, Dynamic Smagorinsky and WALE models, and the UDNS (no-model LES) was also discussed.

The effect of increasing the shear-thinning property (reducing the n value) of the fluids and the Bingham number have similar behaviors on the flow quantities. In the instantaneous flow features, the low-speed streaks of the axial velocity elongate in the streamwise direction; there is a greater amplitude of viscosity fluctuations compared to wall viscosity, and decreasing in the number of vortical structures. These characteristics suggest weaker turbulent structures.

Concerning the mean quantities, the RMS velocity fluctuations enhance in the axial direction; however, they decrease in the radial and the azimuthal directions, and the Reynolds shear stress components. Profiles of mean turbulent kinetic energy do not change significantly but decrease in value at the peak regions with increasing shear-thinning properties and Bingham number; the pressure gradient and the skin friction coefficients present the same tendency.

The mean viscosity profiles are constant near the walls and the effect of both parameters, flow behavior index and the Bingham number, become apparent after $y^+ > 10$. The mean viscosity increases towards the center of the annular section. Moreover, the ratio between the maximum value (at the center of the annular section) and the minimum value (near the wall) of the normalized mean viscosity grows for fluids with higher shear thinning behavior and Bingham number.

Regarding the influence of the Rotation number, the mean axial velocity profiles become flatter and the second-order turbulent statistics augment in magnitude as rotation number N enhances. In addition, asymmetries in the profiles of the RMS velocity fluctuations become apparent with increasing N. The alteration of the turbulent structures is attributed to the centrifugal force arising from the rotation of the inner wall.

The influence of the Rotation number does not produce huge discrepancies in the viscosity profiles, as seen for the effects of flow behavior index n and Bingham number. The ratio between the maximum value (in the center of the annular region) and the minimum value (near the walls) of the mean viscosity distribution is similar for both rotations, although the profiles for $N = 0.30$ present a more parabolic behavior than $N = 0.15$.

Finally, it is interesting that results obtained with the SGS models and the UDNS do not show significant differences, suggesting that the numerical dissipation is dominant over the SGS dissipation rate. These results agree with the profiles presented in Chapter 4, and they are in line with the works developed by (CASTIGLIONI; DOMARADZKI, 2015) and (KOMEN et al., 2017) using low-order schemes.

6 CONCLUSIONS

The research presented in this thesis aimed to investigate the applicability of the LES method in the turbulent flow of Herschel-Bulkley fluids. Although many industrial processes involve turbulent flows of non-Newtonian fluids, there are few studies regarding the LES of GNF.

In the early part of this thesis, simulations were performed to assess the capacity and limitations of the present numerical method. The OpenFOAM package, an implicit finite volume solver with second-order accuracy in space and time was employed for the computations. The OpenFOAM is an open-source CFD code and is commonly used to simulate industrial flows. Turbulent pipe flow with Newtonian and Herschel-Bulkley fluids and the turbulent flow of Newtonian fluid in a concentric annular section with inner wall rotation were considered. The LES approach has been applied with two different SGS models, Dynamic Smagorinsky and WALE models, and the UDNS (no-model LES).

As a first highlight, using a denser grid, the present methodology reproduced the features of the non-Newtonian fluid flows, and it presented consistent results compared to DNS data obtained by the second-order finite volume method. However, the results are reasonable for the second-order statistics when the current predictions are compared with data from a high-accuracy spectral DNS code.

In addition, it was observed that results predicted with the SGS models and the UDNS did not yield significant differences. Some authors argue that the contribution of the SGS models is small if the numerical dissipation in low-order schemes is dominant over the SGS dissipation rate (KRAVCHENKO; MOIN, 1997; CASTIGLIONI; DOMARADZKI, 2015)

With a huge amount of spatial and temporal scales existing in the turbulent flow field, the LES can be helpful to computing the evolution of instantaneous or mean quantities associated with turbulent flows where engineering precision is the desired outcome for industrial problems. The LES method can produce qualitatively consistent results at a reduced computational cost than a DNS solution.

Subsequently, the current methodology was applied to explore the turbulent flow of Herschel-Bulkley fluids in a concentric annular section with inner wall rotation. This type of flow usually occurs in the oil well drilling process, where drilling fluid is pumped into the drill string and returns to the surface carrying the cuttings through the annular region formed between the hole walls and drill string. The effects of the flow behavior index ($n = 0.75, 0.70$ and 0.65), Bingham number ($B_n = 0.10, 0.25$, and 0.40), and the influence of Rotation number ($N = 0.15$ and 0.30) on the flow quantities were investigated.

As a second highlight, the effect of increasing the shear-thinning property (reducing the *n* value) of the fluids and the Bingham number have similar behaviors on the flow quantities. As both parameters enhance, weaker turbulent structures are generated in the flow field. In the instantaneous flow features, the low-speed streaks elongate in the streamwise direction; there is a greater amplitude of viscosity fluctuations compared to wall viscosity and decreasing in the number of vortical structures. These characteristics suggest weaker turbulent structures.

Concerning the mean quantities, the RMS velocity fluctuations enhance in the axial direction but decrease in the radial and the azimuthal directions due to the turbulence anisotropy enhancement. The

Reynolds shear stress also decreases with augmenting the shear-thinning property and the Bingham number. Profiles of mean turbulent kinetic energy do not change significantly but decrease in value at the peak regions with increasing shear-thinning properties and Bingham number; the pressure gradient and the skin friction coefficients present the same tendency.

The mean viscosity profiles are constant near the walls, and the effect of both parameters, the flow behavior index and the Bingham number, become apparent after $y^+ > 10$. The mean viscosity increases towards the center of the annular section. Moreover, the ratio between the maximum value (at the center of the annular section) and the minimum value (near the wall) of the normalized mean viscosity grows for fluids with higher shear thinning behavior and Bingham number.

Regarding the influence of the Rotation number, the mean axial velocity profiles become flattered and the second-order turbulent statistics augment in magnitude as rotation number N enhances. In addition, asymmetries in the profiles of the RMS velocity fluctuations become apparent with increasing N. The modification of the turbulent structures is attributed to the centrifugal force arising from the rotation of the inner wall.

The influence of the rotation number does not produce huge discrepancies in the viscosity profiles, as seen for the effects of flow behavior index n and Bingham number. The ratio between the maximum value (in the center of the annular region) and the minimum value (near the walls) of the mean viscosity distribution is similar for both rotation numbers, although the profiles for $N = 0.30$ present a more parabolic behavior than $N = 0.15$.

6.1 Recommendations and Suggestions for future research

Some issues that could be considered for future works are suggested below.

- The study presented in Chapter 5 could be extended to investigate the eccentricity effect of the annular region on the flow quantities, as well as increase the range of parameters n, B_n, Re_G, and N evaluated.
- In order to improve the quality of the results of Chapter 5 and introduce an analysis of the TKE budgets, the simulations could be performed with a higher-order scheme.
- Once the numerical dissipation can mask the predictive capability of the SGS models, whenever it is of the same order of magnitude or greater than the SGS dissipation rate, it would be interesting to extend the work and quantify numerical dissipation and SGS dissipation rate.
- Finally, develop a closure model for the non-Newtonian SGS stress tensor to reduce the computational cost and produce satisfactory results even with coarse grids.

BIBLIOGRAPHY

ADEDOYIN, A. A.; WALTERS, D. K.; BHUSHAN, S. Investigation of turbulence model and numerical scheme combinations for practical finite-volume large eddy simulations. *Engineering Applications of Computational Fluid Mechanics*, v. 9, n. 1, p. 324–342, 2015.

ALEXANDROU, A. N.; MENN, P. L.; GEORGIOU, G.; ENTOV, V. Flow instabilities of Herschel–Bulkley fluids. *Journal of Non-Newtonian Fluid Mechanics*, v. 116, n. 1, p. 19–32, 2003.

AMANI, E.; AHMADPOUR, g. A.; AGHAJARI, M. J. Dynamic subgrid-scale LES model for turbulent non-Newtonian flows: A priori and a posteriori analyses of Burgers turbulence. *Journal of Non-Newtonian Fluid Mechanics*, v. 295, 2021.

ANBARLOOEI, H. R.; CRUZ, D. O. A.; SILVA FREIRE, A. P. Fully turbulent mean velocity profile for purely viscous non-Newtonian fluids. *Proceedings of the 15th European Turbulence Conference, Delft, The Netherlands*, p. 25–28, 2015.

AROSEMENA, A. A.; ANDERSSON, H. I.; SOLSVIK, J. Turbulent channel flow of generalized Newtonian fluids at a low Reynolds number. *Journal of Fluid Mechanics*, v. 908, p. A43:1–41, 2021.

ASTARITA, G.; MARRUCCI, G. *Principles of non-Newtonian Fluid Mechanics*. [S.l.]: McGraw-Hill Inc, 1974.

BAGUERI, E.; WANG, B. C.; YANG, Z. Influence of domain size on direct numerical simulation of turbulent flow in a moderately curved concentric annular pipe. *Physics of Fluids*, v. 32, 2020.

BAHRANI, A.; NOUAR, C. Intermittency in the transition to turbulence for a shear-thinning fluid in Hagen-Poiseuille flow. *Journal of Applied Fluid Mechanics*, v. 7, p. 1–6, 2014.

BALMFORTH, N. J.; FRIGAARD, I. A.; OVARLEZ, G. Yielding to Sress: Recent Developments in Viscoplastic Fluid Mechanics. *Ann Rev Fluid Mech*, v. 46, p. 121–146, 2014.

BAYLY, B. J.; ORSZAG, S. A.; HERBERT, T. Instability mechanisms in shear-flow transition. *Anne. Rev. Fluid Mechanics*, v. 20, p. 487–526, 1988.

BEN-NARS, O.; HADJADJ, A.; CHAUDHURI, A. Assessment of subgrid-scale modeling for large-eddy simulation of a spatially-evolving compressible turbulent boundary layer. *Computers & Fluids*, v. 151, p. 144–158, 2017.

BENZI, M. Preconditioning Techniques for Large linear systems: A survey. *Journal of Computational Physics*, v. 182, p. 418–477, 2002.

BIRD, R. B.; ARMSTRONG, R. C.; HASSAGER, O. *Dynamics of polymeric liquids. Vol. 1: Fluid mechanics*. [S.l.]: John Wiley and Sons Inc., New York, NY, 1987.

CADIEUX, F.; SUN, G.; DOMARADZKI, J. A. Effects of numerical dissipation on the interpretation of simulation results in computational fluid dynamics. *Computers & Fluids*, v. 154, p. 256–272, 2017.

CAENN, R.; CHILLINGAR, G. V. Drilling fluids: State of the art. *Journal of Petroleum Science and Engineering*, Elsevier, v. 14, n. 3-4, p. 221–230, 1996.

CAENN, R.; DARLEY, H.; GRAY, G. *Composition and Properties of Drilling and Completion Fluids*. [S.l.]: Elsevier Science, 2017.

CASSINELLI, A.; GIOVANETTI, M. D.; HWANG, Y. Streak instability in near-wall turbulence revisited. *Journal of Turbulence*, v. 18, n. 5, p. 443–464, 2017.

CASTIGLIONI, G.; DOMARADZKI, J. A numerical dissipation rate and viscosity in flow simulations with realistic geometry using low-order compressible Navier–Stokes solvers. *Computers & Fluids*, v. 119, p. 37–46, 2015.

CELIK, I. B.; CEHRELI, Z. N.; YAVUZ, I. Index of Resolution Quality for Large Eddy Simulations. *Journal of Fluids Engineering*, v. 127, p. 949–958, 2005.

CHHABRA, R. P.; RICHARDSON, J. F. *Non-Newtonian flow and applied rheology: engineering applications*. [S.l.]: Butterworth-Heinemann, 2008.

CHUNG, S. Y.; RHEE, G. H.; SUNG, H. J. Direct numerical simulation of turbulent concentric annular pipe flow: Part 1: Flow field. *International Journal of Heat and Fluid Flow*, Elsevier, v. 23, n. 4, p. 426–440, 2002.

CHUNG, S. Y.; SUNG, H. J. Large-eddy simulation of turbulent flow in a concentric annulus with rotation of an inner cylinder. *International Journal of Heat and Fluid Flow*, v. 26, p. 191–203, 2005.

DAMIÁN, S. An Extended Mixture Model for the Simultaneous Treatment of Short and Long Scale Interfaces (Ph.D. thesis). *UNIVERSIDAD NACIONAL DEL LITORAL, Instituto de Desarrollo Tecnologico para la Industria Quimica*, 2013.

DAVIDSON, L. Large Eddy Simulations: How to evaluate resolution. *Journal of Heat and Fluid Flow*, v. 30, p. 1016–1025, 2009.

DAVIDSON, L. How to estimate the resolution of an LES of recirculating flow Turbulence. *Quality and Reliability of Large-Eddy Simulations II*, v. 16, p. 269–286, 2011.

DAVIDSON, P. A. *Turbulence: An Introduction for Scientists and Engineers*. [S.l.]: OUP Oxford, 2004.

DE VILLIERS, E. The potential of large eddy simulation for the modeling of wall bounded flows (Ph.D. thesis). *Imperial College of Science, Technology and Medicine*, 2006.

Den Toonder, J. M. J.; NIEWSTADT, F. T. M. Reynolds number effects in a turbulent pipe flow for low to moderate Re. *Physics of Fluids*, v. 9, p. 3398–3409, 1997.

DESHPANDE, A.; KRISHNAN, J. M.; KUMAR, P. *Rheology of Complex Fluids*. [S.l.]: Springer, 2010.

DODGE, D. W.; METZNER, A. B. Turbulent flow of non-newtonian systems. *A. I. Ch. E. Journal*, v. 5, n. 2, p. 189–204, 1959.

DURBIN, P. A.; PETTERSSON-REIF, B. A. *Statistical Theory and Modeling for Turbulent Flows*. [S.l.]: Wiley, 2015.

EPELLE, E. I.; GEROGIORGIS, D. I. Transient and steady state analysis of drill cuttings transport phenomena under turbulent conditions. *Chemical Engineering Research and Design*, v. 131, p. 520–544, 2018.

ERGE, O.; OZBAYOGLU, E. M.; MISKA, S. Z.; YU, M.; TAKACH, N.; SAASEN, A.; MAY, R. The effects of drillstrings -eccentricity, -rotaion, and -buckling configurations on annular frictional pressure losses while circulating yield-power-law fluids. *SPE Drilling & Completion*, 2015a.

ERGE, O.; OZBAYOGLU, E. M.; MISKA, S. Z.; YU, M.; TAKACH, N.; SAASEN, A.; MAY, R. Laminar to turbulent transition of yield power-law fluids in annuli. *Journal of Petroleum Science and Engineering*, v. 128, p. 128–139, 2015b.

ESCUDIER, M. P.; GOULDSON, I. W.; JONES, D. M. Flow of shear-thinning fluids in a concentric annulus. *Experiments in Fluids*, v. 18, p. 225–238, 1995.

ESCUDIER, M. P.; POOLE, R. J.; PRESTI, F.; DALES, C.; NOUAR, C.; DESAUBRY, C.; GRAHAM, L.; PULLUM, L. Observations of asymmetrical flow behaviour in transitional pipe flow of yield-stress and other shear-thinning liquids. *Journal of Non-Newtonian Fluid Mechanics*, v. 127, p. 143–155, 2005.

ESCUDIER, M. P.; PRESTI, F. Pipe flow of a thixotropic liquid. *Journal of Non-Newtonian Fluid Mechanics*, v. 62, p. 291–306, 1996.

ESMAEL, E.; NOUAR, C. Transitional flow of a yield-stress fluid in a pipe: Evidence of a robust coherent structure. *Physical Review*, v. 77, 2008.

FERZIGER, J. H.; PERIC, M. *Computational Methods for Fluid Dynamics*. [S.l.]: Springer, 2002.

GAVRILOV, A. A.; RUDYAK, V. Y. Direct numerical simulation of the turbulent flows of power-law fluids in a circular pipe. *Thermophysics and Aeromechanics*, v. 23, p. 473–486, 2016.

GAVRILOV, A. A.; RUDYAK, V. Y. Direct numerical simulation of the turbulent energy balance and the shear stresses in Power-law fluid flow in pipes. *Fluid Dynamics*, v. 52, n. 3, p. 363–374, 2017.

GERMANO, M.; PIOMELLI, U.; MOIN, P.; CABOT, W. H. A dynamic subgrid-scale eddy viscosity model. *Physics of Fluids A: Fluid Dynamics*, v. 3, n. 7, p. 1760–1765, 1991.

GNAMBODE, P. S.; ORLANDI, P.; OULD-ROUISS, M.; NICOLAS, X. Large-Eddy simulation of turbulent pipe flow of power-law fluids. *International Journal of Heat and Fluid Flow*, v. 54, p. 196–210, 2015.

GRINSTEIN, F. F.; MARGOLIN, L. G.; RIDER, W. J. *Implicit Large Eddy Simulation. Computing Turbulent Fluid Dynamics.* [S.l.]: Cambridge University Press, 2007.

GUZEL, B.; BURGHELEA, T.; FRIGAARD, I. A.; MARTINEZ, D. M. Observation of laminar–turbulent transition of a yield stress fluid in Hagen–Poiseuille flow. *Journal of Fluid Mechanics*, v. 627, p. 97–128, 2009.

HANKS, R. W. Low Reynolds number turbulent pipeline flow of pseudohomogeneous slurries. *In: Fifth International Conference on the Hydraulic Transport of Solids in Pipes (Hydrotransport 5)*, v. 13, p. 23–34, 1978.

HIRSC, C. *Numerical Computations of internal and external flows: The Fundamental of computational fluid dynamics*. [S.l.]: Elsevier, 2007.

HOSSAIN, M. E.; AL-MAJED, A. A. *Fundamentals of Sustainable Drilling Engineering*. [S.l.]: Wiley-Scrivener, 2015.

INAGAKI, M. Large eddy simulation of non-Newtonian viscous fluids with low grid dependency using an anisotropy-resolving subgrid-scale model. *Journal of Non-Newtonian Fluid Mechanics*, v. 295, 2021.

ISSA, R. I. Solution of the implicitly discretized fluid flow equations by operator splitting. *Journal of Computational Physics*, v. 62, p. 40–65, 1986.

JAPPER-JAAFAR, A.; ESCUDIER, M. P.; POOLE, R. J. Laminar, transitional and turbulent annular flow of drag-reducing polymer solutions. *Journal of Non-Newtonian Fluid Mechanics*, v. 165, p. 1357–1372, 2010.

JASAK, H. Error analysis and estimation for the finite volume method with applications to fluid flows (Ph.D. thesis). *Imperial College of Science, Technology and Medicine*, 1996.

JEONG, J.; HUSSAIN, F. On the identification of a vortex. *Journal of Fluid Mechanics*, v. 285, p. 69–94, 1995.

JIANG, X.; LAI, C. H. *Numerical techniques for direct and large-eddy simulations*. [S.l.]: CRC Press, 2009.

KELIN, W.; TIE, Y.; XIAOFENG, S.; SHUAI, S.; SHIZHU, L. Review and analysis of cuttings transport in complex structural wells. *The Open Fuels Energy Science Journal*, v. 26, p. 9–17, 2013.

KELLY, N. S.; GILL, H. S.; COOKSON, A. N.; FRASER, K. H. Influence of shear-thinning blood rheology on the laminar-turbulent transition over a backward facing step. *Fluids*, v. 5, n. 2, 2020.

KHAN, M.; VALAN-SENDSTADL, K.; STEINMAN, D. A. Direct numerical simulation of laminar-turbulent transition in a non-axisymmetric stenosis model for Newtonian vs. shear-thinning non-Newtonian rheologies. *Flow Turbulence Combust*, 2018.

KIM, J.; MOIN, P.; MOSER, R. Turbulence statistics in fully developed channel flow at low Reynolds number. *Journal of Fluid Mechanics*, v. 177, p. 133–166, 1987.

KOMEN, E.; SHAMS, A.; CAMILO, L.; KOREN, B. Quasi-DNS capabilities of OpenFOAM for different mesh types. *Computers & Fluids*, v. 96, p. 87–104, 2014.

KOMEN, E. M. J.; CAMILO, L. H.; SHAMS, A.; GEURTS, B. J.; KOREN, B. A quantification method for numerical dissipation in quasi-DNS and under-resolved DNS, and effects of numerical dissipation in quasi-DNS and under-resolved DNS of turbulent channel flows. *Journal of Computational Physics*, v. 345, p. 565–595, 2017.

KRAVCHENKO, A. G.; MOIN, P. On the effect of numerical errors in large eddy simulations of turbulent flows. *Journal of Computational Physics*, v. 154, p. 310–322, 1997.

LAMPITELLA, P. Large eddy simulation for complex industrial flows (Ph.D. thesis). *Politecnico di Milano, Doctoral Programme in Energy and Nuclear Science and Technlogy*, 2014.

LAVAL, J. P. Lecture notes on DNS and LES. *International Masters Program in Turbulence, Centrale Lille*, 2020.

LESIEUR, M.; MÉTAIS, O.; COMTE, P. *Large-eddy simulations of turbulence*. [S.l.]: Cambridge University Press, 2005.

LILLY, D. K. A proposed modification of the Germano subgrid-scale closure method. *Physics of Fluids A: Fluid Dynamics*, v. 4, n. 3, p. 633–635, 1992.

LIU, N. S.; LU, X. Y. Large eddy simulation of turbulent flows in a rotating concentric annular channel. *International Journal of Heat and Fluid Flow*, v. 26, p. 378–392, 2005.

LUGARINI DE SOUZA, A. Lattice Boltzmann Method for Direct Numerical Simulation of Viscoplastic Turbulent flow. (Ph.D. thesis). *Postgraduate Programme in Mechanical and Materials Engineering, Federal University of Technology – Paraná, Curitiba, Brazil*, 2020.

MACOSKO, W. *Rheology principles, measurements, and applications*. [S.l.]: Wiley – VHC, 1994.

MALIN, M. Turbulent pipe flow of Herschel-Bulkley fluids. *International communications in heat and mass transfer*, v. 25, n. 3, p. 321–330, 1998.

MENTER, F. R. Best Practice: Scale-resolving Simulations in ANSYS CFD. *ANSYS Inc*, 2012.

METZNER, A. B.; REED, J. C. Flow of non-Newtonian fluids – correlations for laminar, transition and turbulent flow regimes. *A. I. Ch. E. Journal*, v. 1, n. 4, p. 434–444, 1955.

MEYERS, J.; GEURTS, B.; BEALMANS, M. Database analysis of errors in large-eddy simulation. *Physics of Fluids*, v. 15, n. 9, p. 2740–2755, 2003.

MITCHELL, R.; MISKA, S. *Fundamentals of drilling engineering*. [S.l.]: Richardson, USA: Society of Petroleum Engineers, 2011.

MOLLA, M. M.; PAUL, M. C. LES of non-Newtonian physiological blood flow in a model of arterial stenosis. *Medical Engineering & Physics*, v. 34, p. 1079–1087, 2012.

MONTREUIL, E. Simulation numérique pour l'aérothermique avec des modéles sous-maille (Ph.D. thesis). *Mécanique Université Pierre et Marie Curie - Paris VI*, 2000.

MOUKALLED, F.; MANGANI, L.; DARWISH, M. *The Finite Volume Method in Computational Fluid Dynamics: An Advanced Introduction with OpenFOAM and Matlab*. [S.l.]: Springer International Publishing, Switzerland, 2016.

NASEEM, A.; HAMILTON, N.; CALAF, M.; CAL, R. B. Turbulence kinetic energy budget and conditional sampling of momentum, scalar, and intermittency fluxes in thermally stratified wind farms. *Journal of Turbulence*, v. 20, p. 32–63, 2019.

NICOUD, F.; DUCROS, F. Subgrid-scale stress modelling based on the square of the velocity gradient tensor. *Flow, turbulence and Combustion*, v. 62, n. 3, p. 183–200, 1999.

NOURI, J. M.; UMUR, H.; WHITELAW, J. H. Flow of Newtonian and non-Newtonian fluids in concentric and eccentric annuli. *Journal of Fluid Mechanics*, v. 253, p. 617–641, 1993.

NOURI, J. M.; WHITELAW, J. H. Flow of Newtonian and non-Newtonian fluids in a concentric annulus with rotation of the inner cylinder. *Journal of Fluids Engineering*, v. 116, p. 821–827, 1994.

NOURI, J. M.; WHITELAW, J. H. Flow of Newtonian and non-Newtonian fluids in an eccentric annulus with rotation of the inner cylinder. *International Journal of Heat and Fluid Flow*, v. 18, p. 236–246, 1997.

OHTA, T.; MIYASHITA, M. DNS and LES with an extended smagorinsky model for wall turbulence in non-Newtonian viscous fluids. *Journal of Non-Newtonian Fluid Mechanics*, v. 206, p. 29–39, 2014.

OKAMOTO, M.; SHIMA, N. Direct numerical simulation of rotating turbulent flows through concentric annuli. *Engineering Turbulence Modelling and Experiments*, v. 6, p. 217–226, 2005.

OSSWALD, T.; RUDOLPH, N. *Polymer Rheology: Fundamentals and Applications*. [S.l.]: Hanser Publications, 2015.

PARK, J. T.; MANNHEIMER, R. J.; GRIMLEY, T. A.; MORROW, T. B. Pipe flow measurements of a transparent non-Newtonian slurry. *Journal of Fluids Engineering*, v. 111, 1989.

PEIXINHO, J.; NOUAR, C.; DESAUBRY, C.; THÉRON, B. Laminar transitional and turbulent flow of yield stress fluid in a pipe. *Journal of Non-Newtonian Fluid Mechanics*, v. 128, p. 172–184, 2005.

PEREIRA, A. S.; PINHO, F. T. Turbulent pipe flow characteristics of low molecular weight polymer solutions. *Journal of Non-Newtonian Fluid Mechanics*, v. 55, p. 321–344, 1994.

PINHO, F. T.; WHITELAW, J. H. Flow of non-Newtonian fluids in a pipe. *Journal of Non-Newtonian Fluid Mechanics*, v. 34, p. 129–144, 1990.

PIOMELLI, U. Large-eddy simulation: achievements and challenges. *Progress in Aerospace Sciences*, Elsevier, v. 35, p. 335–362, 1999.

PONCET, S.; VIAZZO, S.; OGUIC, R. Large eddy simulations of Taylor-Couette-Poiseuille flows in a narrow-gap system. *Physics of Fluids*, v. 26, n. 10, p. 105108, 2014.

POPE, S. B. *Turbulent flows*. [S.l.]: Cambridge University Press, 2000.

REYNOLDS, O. On the dynamical theory of incompressible viscous fluids and the determination of the criterion. *Philosophical Transactions of the Royal Society of London, Series A*, v. 186, 1896.

RICHARDSON, L. F. *Weather prediction by numerical process*. [S.l.]: Cambridge University Press, 1922.

RODI, W.; CONSTANTINESCU, G.; STOESSER, T. *Large-Eddy Simulation in Hydraulics*. [S.l.]: Cambridge University Press, 2013.

RUDMAN, M.; BLACKBURN, H. M. Direct numerical simulation of turbulent non-Newtonian flow using a spectral element method. *Applied Mathematical Modelling*, v. 30, p. 1229–1248, 2006.

RUDMAN, M.; BLACKBURN, H. M.; GRAHAM, L. J. W.; PULLUM, L. Turbulent pipe flow of shear-thinning fluids. *Journal of Non-Newtonian Fluid Mechanics*, v. 118, p. 33–48, 2004.

SAGAUT, P. *Large eddy simulation for incompressible flows: an introduction*. [S.l.]: Springer Science & Business Media, 2006.

SAGAUT, P.; DECK, S.; TERRACOL, M. *Multiscale and Multiresolution Approaches in Turbulence*. [S.l.]: Imperial College Press, 2006.

SCHILICHTING, H. *Boundary Layer Theory*. [S.l.]: McGraw-Hill, New York, 1979.

SCHNEIDER, M.; YOUNIS, B. A.; WEIGAND, B. Large eddy simulations of flow and heat transfer in heated concentric annulus with inner cylinder rotation. *International Journal of Heat and Mass Transfer*, v. 32, p. 1248–1262, 2017.

SINGH, J.; RUDMAN, M.; BLACKBURN, H. M. The influence of shear-dependent rheology on turbulent pipe flow. *Journal of Fluid Mechanics*, v. 822, p. 848–879, 2017a.

SINGH, J.; RUDMAN, M.; BLACKBURN, H. M. The effect of yield stress on pipe flow turbulence for generalised Newtonian fluids. *Journal of Non-Newtonian Fluid Mechanics*, v. 249, p. 53–62, 2017b.

SINGH, J.; RUDMAN, M.; BLACKBURN, H. M. Reynolds number effects in pipe flow turbulence of generalized Newtonian fluids. *Physical Review Fluids*, v. 3, 2018.

SINGH, J.; RUDMAN, M.; BLACKBURN, H. M.; CHRYSS, A.; PULLUM, L. The importance of rheology characterization in predicting turbulent pipe flow of generalized newtonian fluids. *Journal of Non-Newtonian Fluid Mechanics*, v. 232, p. 11–21, 2016.

SLATTER, P. T. Transitional and turbulent flow of non-Newtonian slurries in pipes (Ph.D. thesis). *Department of Civil Engineering, University of Cape Town, Cape Town*, 1995.

SMAGORINSKY, J. General circulation experiments with the primitive equations: I. The basic experiment. *Monthly Weather Review*, v. 91, p. 99–164, 1963.

TENNEKES, H.; LUMLEY, J. L. *A first course in turbulence*. [S.l.]: The MIT Press, 1978.

TORRANCE, B. M. Friction factors for turbulent non-Newtonian fluid flow in circular pipes. *South African Mechanical Engineering*, v. 13, p. 89–91, 1963.

VERSTEEG, H. K.; MALALASEKERA, W. *An Introduction to Computational Dynamics: The Finite Volume Method*. [S.l.]: Prentice Hill, 2007.

WILCOX, D. C. *Turbulence Modeling for CFD*. [S.l.]: La Canada CA, 1993.

WILSON, K. C.; THOMAS, A. D. A new analysis of the turbulent flow of non-Newtonian fluids. *The Canadian Journal of Chemical Engineering*, v. 63, n. 4, p. 539–546, 1985.

XU, H. A.; YANG, X. I. A. Treatment of unphysical numerical oscillations via local grid refinement. *Physics of Fluids*, v. 33, p. 077104, 2021.

ZAMAN, A.; ALI, N.; SADIJ, M. Effects of unsteadiness and non-Newtonian rheology on blood flow through a tapered time-variant stenotic artery. *Aip Advances 5*, 2015.

ZANG, T. A. Numerical simulation of the dynamics of turbulent boundary layers: perspectives of a transition simulator. *Philosophical Transactions of the Royal Society A*, v. 72, p. 50–67, 1991.

ZHENG, E. Z.; RUDMAN, M.; SINGH, J.; KUANG, S. B. Direct numerical simulation of turbulent non-newtonian flow using openFOAM. *Applied Mathematical Modelling*, v. 72, p. 50–67, 2019.

APPENDIX A – BALANCE EQUATIONS IN CYLINDRICAL COORDINATES

A.1 Conservation equaions

The equations of motion are presented in cylindrical coordinates for an incompressible fluid in terms of viscous stress tensor $\boldsymbol{\sigma}$ (BIRD et al., 1987). The gravity is neglected.

Continuity:

$$\frac{1}{r}\frac{\partial}{\partial r}\left(r u_r\right)+\frac{1}{r}\frac{\partial}{\partial \theta}\left(u_\theta\right)+\frac{\partial}{\partial z}\left(u_z\right)=0 \tag{A.1}$$

r-component:

$$\begin{gathered}\rho\left(\frac{\partial u_r}{\partial t}+u_r\frac{\partial u_r}{\partial r}+\frac{u_\theta}{r}\frac{\partial u_r}{\partial \theta}+u_z\frac{\partial u_r}{\partial z}-\frac{u_\theta^2}{r}\right)= \\ -\frac{\partial p}{\partial r}-\left\{\frac{1}{r}\frac{\partial}{\partial r}\left(r\sigma_{rr}\right)+\frac{1}{r}\frac{\partial}{\partial \theta}\sigma_{\theta r}+\frac{\partial}{\partial z}\sigma_{zr}-\frac{\sigma_{\theta\theta}}{r}\right\}\end{gathered} \tag{A.2}$$

θ-component:

$$\begin{gathered}\rho\left(\frac{\partial u_\theta}{\partial t}+u_r\frac{\partial u_\theta}{\partial r}+\frac{u_\theta}{r}\frac{\partial u_\theta}{\partial \theta}+u_z\frac{\partial u_\theta}{\partial z}+\frac{u_r u_\theta}{r}\right)= \\ -\frac{1}{r}\frac{\partial p}{\partial \theta}-\left\{\frac{1}{r^2}\frac{\partial}{\partial r}\left(r^2\sigma_{r\theta}\right)+\frac{1}{r}\frac{\partial}{\partial \theta}\sigma_{\theta\theta}+\frac{\partial}{\partial z}\sigma_{z\theta}+\frac{\sigma_{\theta r}-\sigma_{r\theta}}{r}\right\}\end{gathered} \tag{A.3}$$

z-component:

$$\begin{gathered}\rho\left(\frac{\partial u_z}{\partial t}+u_r\frac{\partial u_z}{\partial r}+\frac{v_\theta}{r}\frac{\partial u_z}{\partial \theta}+u_z\frac{\partial u_z}{\partial z}\right)= \\ -\frac{\partial p}{\partial z}-\left\{\frac{1}{r}\frac{\partial}{\partial r}\left(r\sigma_{rz}\right)+\frac{1}{r}\frac{\partial}{\partial \theta}\sigma_{\theta z}+\frac{\partial}{\partial z}\sigma_{zz}\right\}\end{gathered} \tag{A.4}$$

APPENDIX B – TURBULENT PIPE FLOW OF THE HERSCHEL-BULKLEY FLUID AT $Re_G = 10,600$ ($Re_\tau = 633$)

The set of numerical simulations presented in Section 4.1.5 for turbulent pipe flow of Herschel-Bulkley fluids is extended in this section. An additional simulation is presented here. The DNS results of Singh et al. (2016) are compared with the current LES and UDNS approaches.

B.1 Computational Methodology

The pipe length in the axial direction is defined as $L_z = 4\pi D$ with $D = 0.0445$ [m]. The bulk velocity and the pressure gradient used by Singh et al. (2016) were estimated experimentally, and the values of these quantities are 2.90 [$\mathrm{m\ s^{-1}}$]. and 2.72 [$\mathrm{kPa\ m^{-1}}$], respectively. The model parameters of the Herschel-Bulkley fluid are given in Table B.1. According to the author, the model parameters were determined experimentally via rheology measurements.

The computational grid employed in the current simulations is the same mesh used in the simulations for $Re_G = 7,500$ of Section 4.1.5 (mesh VIII from Table 4.2). The number of cells in the axial, radial, and azimuthal directions are $N_z = 162$,$N_r = 36$, and $N_\theta = 122$, totaling approximately 1.1 M elements. The mesh resolution in wall units is $\Delta z^+ \approx 50$, $R\Delta\theta^+ \approx 14$, and $\Delta r^+_{wall} \approx 0.50$.

Table B.1 – Model parameters of a Herschel-Bulkley fluid for the turbulent pipe flow simulations at $Re_G = 10,600$.

τ_y (Pa)	K (Pa s^n)	ρ (kg m^{-3})	n
0.72	0.129	1,000	0.69

Singh et al. (2016).

B.2 Results and Discussion

The mean axial velocity profiles are illustrated in Figure B.1. The results obtained with SGS models and the UDNS agree with the DNS data until $y^+ < 10$; however, the solutions overpredict the DNS velocity profile in the logarithm region. The difference between current simulations and DNS prediction is about 3.9% after $y^+ < 30$.

The second-order statistics of the velocity field are reported in Figure B.2. Following the data trend presented in Section 4.1.5, the OpenFOAM computes the radial and azimuthal turbulence intensities and Reynolds shear stress in lower magnitudes. On the other hand, the axial turbulence intensity overpredicts the DNS data. The relative differences in axial, radial, and azimuthal turbulence intensities at the peak are 9%, 8%, and 12%, respectively.

Figure B.1 – Mean axial velocity profiles of the Herschel-Bulkley fluid plotted in wall units at $Re_G = 10,600$.

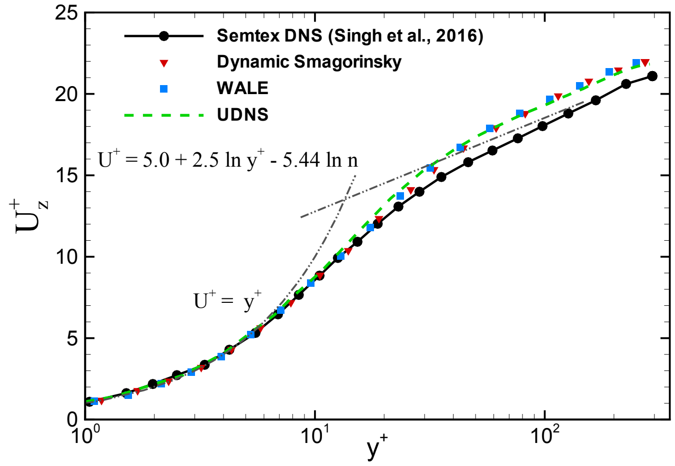

Source: Own elaboration.

Figure B.2 – Profiles of RMS velocity fluctuations in (a) axial, (b) radial, (c) azimuthal directions, and (d) Reynolds shear stress of the Herschel-Bulkley fluid plotted in wall units at $Re_G = 10,600$.

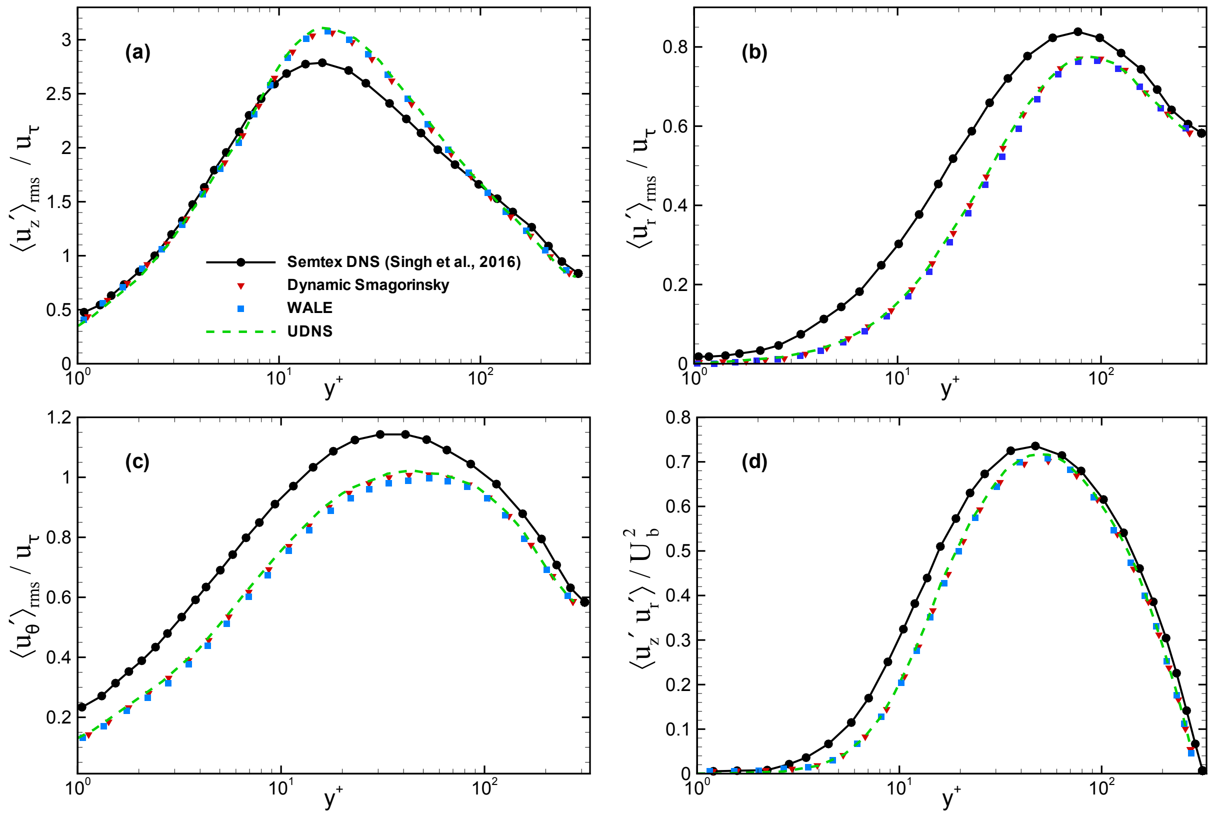

Source: Own elaboration.

The radial distributions of the mean viscosity normalized by the wall viscosity are shown in Figure B.3. The present profiles of both SGS models and the UDNS align with the DNS results of Singh et al. (2016). The maximum deviation (≈5%) between current simulations and the reference data occurs in the core region at $y^+ = 300$.

Figure B.3 – Mean viscosity profiles of the Herschel-Bulkley fluid plotted in wall units at $Re_G = 10,600$.

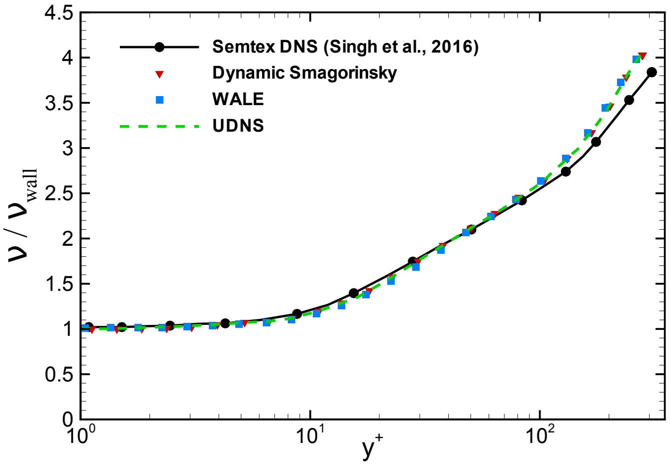

Source: Own elaboration.

The flow quantities, including mean wall shear stress, mean pressure gradient, mean wall viscosity, and the Reynolds number based on the friction velocity are presented in Table A.2. The mean wall shear stress and the mean pressure gradient estimated by Singh et al. and the present work show differences of approximately 13%. The maximum deviations for the mean wall viscosity and Reynolds number are 3.5% and 8.5%, respectively.

Table B.2 – Comparison between the present work and the reference DNS data of Singh et al. (2016) for mean wall shear stress, mean pressure gradient, mean wall viscosity, and Reynolds number based on the friction velocity.

	τ_w $[Pa]$	dp/dz $[Pa\ m^{-1}]$	ν_{wall} $[m^2\ s^{-1}]$	Re_τ
Semtex DNS (SINGH et al., 2016)	30.25	2,720	1.217e-05	633
Dynamic Smagorinsky	27.02	2,429	1.24e-05	587
WALE	26.80	2,408	1.251e-05	583
UDNS	27.28	2,453	1.24e-5	593

Source: Own elaboration.